

THE COOPER UNION FOR THE ADVANCEMENT OF SCIENCE AND ART  
ALBERT NERKEN SCHOOL OF ENGINEERING

# The Development of an Open Source Physics Simulation for Flapping Wing Micro Air Vehicles

By  
Netanel Fiorino

A thesis submitted in partial fulfillment of the requirements for the degree of Master of  
Engineering

Advisors

Dr. Dirk M. Luchtenburg and Dr. Michelle Rosen

THE COOPER UNION FOR THE ADVANCEMENT OF SCIENCE AND ART  
ALBERT NERKEN SCHOOL OF ENGINEERING

This thesis was prepared under the direction of the Candidate's Thesis Advisors and has received approval. It was submitted to the Dean of the School of Engineering and the full Faculty, and was approved as partial fulfillment of the requirements for the degree of Master of Engineering.

---

Barry L. Shoop, Ph.D., P.E. - May 10th, 2024

Dean, Albert Nerken School of Engineering

---

Prof. Dirk M. Luchtenburg - May 10th, 2024  
Candidate's Thesis Advisor

---

Prof. Michelle Rosen - May 10th, 2024  
Candidate's Thesis Advisor

# Acknowledgment

I would like to thank my professors, family, and friends who have believed in me and pushed me to succeed over the past five years of school. I would like to give a special thank you to my advisors and professors, Dr. Martin Luchtenburg and Dr. Michelle Rosen for supporting me and guiding me through this exciting and developing field of flapping wing micro air vehicles. Your support and encouragement to push myself and challenge myself have allowed me to deliver a thesis that I am proud of and that truly represents a culmination of my undergraduate and graduate education. I am extremely thankful to my family, and specifically my parents who have enabled and supported me throughout my undergraduate and graduate endeavors. Without your support, none of this would be possible. To my roommates, Gavri and Ayden, thank you for always being a source of inspiration and for always being there for me when things got tough. Seeing the effort and time that you spent on your respective thesis', kept me motivated and encouraged. Many others played a role in this thesis and I thank every one of you for your help.

# Abstract

In recent years, robotics has advanced, yielding aerial vehicles mimicking the flight of insects and birds. This thesis presents an open-source simulation for the Cooper Union Bio-Inspired Robotics Design (CUBIRD) Flapping Wing Micro Air Vehicle (FWMAV) project, aiming to create a lightweight, accessible FWMAV. Despite abundant resources for rotary or fixed-wing drones, FWMAV development lacks accessible tools due to complex design requirements and the need for more advanced controllers. This simulation bridges this gap, enabling users to test the effects of various changes in their design choices. The adaptable simulation accommodates various FWMAV sizes and configurations, allowing adjustments to critical dimensions like wing shapes and the center of mass position. A modified quasi-steady aerodynamic model, based on blade element theory, accurately computes forces and moments during flapping motion, considering factors like unsteady leading edge vortex effects, rotational effects, and added mass effects. The simulation was verified by comparing a purchased FWMAV's movement to a simulated counterpart under identical conditions. The simulation displayed similar flight patterns with small oscillations appearing and possessed similar trends in the overall trajectory and rotation of the FWMAV. Minor discrepancies suggest room for improvement in the body and tail aerodynamic models and the necessity

of more precise wing shape equations. Nevertheless, the simulation serves as a valuable design tool, allowing users to explore the impact of different designs on FWMAV performance. In summary, this thesis contributes an accessible and versatile simulation platform, fostering future innovations in FWMAV research and development.

# Contents

<b>Abstract</b>	<b>iii</b>
<b>List of Figures</b>	<b>xviii</b>
<b>Table of Nomenclature</b>	<b>xix</b>
<b>Introduction</b>	<b>1</b>
1.1 Motivation . . . . .	1
1.2 Intermittent Flight . . . . .	4
1.3 FWMAV Dynamical Model . . . . .	6
1.3.1 Aerodynamics . . . . .	8
1.3.2 Simulation Organization . . . . .	10
1.4 Active Control . . . . .	12
1.5 Outline . . . . .	13
<b>Physics Model Development</b>	<b>16</b>
2.1 Introduction . . . . .	16
2.2 Equations of Motion . . . . .	18
2.2.1 Reference Frames . . . . .	21
2.2.2 Rigid Body Dynamics Equations . . . . .	24

2.2.3	Aerodynamic Gliding Forces . . . . .	26
2.2.4	Aerodynamic Flapping Forces . . . . .	29
2.2.5	Numerical Solver . . . . .	42
2.3	Simulation Setup . . . . .	44
2.3.1	Derivative Function for the Solver . . . . .	44
<b>Simulation Results</b>		<b>48</b>
3.1	Wing Parameter Study . . . . .	48
3.1.1	Effects of Wing Shape . . . . .	52
3.1.2	Effects of Wing Kinematics . . . . .	55
3.1.3	Effects of Flapping Frequency . . . . .	59
3.2	Effects of Tail Location . . . . .	63
3.3	Extended Flight and Comparison to Gliding . . . . .	66
<b>Model Verification</b>		<b>73</b>
4.1	Introduction . . . . .	73
4.1.1	Comparison with the Purchased Flyer . . . . .	74
4.1.2	Comparison with the Purchases Flyer Modified with Rigid Wings . . . . .	81
4.2	Limitations . . . . .	93
<b>Future Work and Conclusion</b>		<b>96</b>
5.1	Future Work . . . . .	96
5.2	Conclusion . . . . .	99

<b>Appendices</b>	<b>102</b>
<b>A Additional Figures for Simulation Results</b>	<b>102</b>
A.1 Parameter Study . . . . .	102
A.1.1 Forces from Different Wing Shapes . . . . .	102
A.1.2 Forces from Different Stroke Amplitudes . . . . .	103
A.1.3 Forces from Different Rotation Amplitudes . . . . .	104
A.1.4 Forces from Different Flapping Frequencies . . . . .	105
A.2 Extended Flight and Comparison to Gliding . . . . .	106
A.2.1 Figures from Flapping Simulation . . . . .	106
A.2.2 Figures from Gliding Simulation . . . . .	109
<b>Bibliography</b>	<b>111</b>

# List of Figures

2.1	Flow diagram for the simulation. . . . .	17
2.2	Wing kinematics and reference angles for a flapping wing. [23]. . . . .	20
2.3	2D global frame, body frame, tail frame, and tail stability frame. . . . .	22
2.4	2D global frame and forces shown in global frame. . . . .	25
2.5	2D global frame and forces shown in their calculated frames, the tail force is in the tail frame, and the wing force is in the body frame. . . . .	27
2.6	Coordinate system and dimensions for a generic wing used in blade element theory calculations. The black lines show the coordinate system used for the wing shape equations, and the red represents the coordinate system used in the blade element theory. . . . .	31
2.7	Stroke angle of rectangular wings of size 0.1m x 0.033m, flap- ping at 10 Hz, in a free stream velocity of 0 m/s. . . . .	39
2.8	Flapping force generated by rectangular wings of size 0.1m x 0.033m, flapping at 10 Hz, in a free stream velocity of 0 m/s. .	40

2.9 Comparison of wing profile angles of the Hawkmoth with the simplified equations. Figure 2.9a shows the stroke and deviation angles. The Hawkmoth's average stroke angle was $21.5^\circ$ , minimum stroke angle was $-30.4^\circ$ , stroke amplitude was $103.9^\circ$ , and the deviation angle was $-13.7^\circ$ Figure 2.9b shows the pitch angle where the average pitch angle was $90^\circ$ , minimum rotation angle was $60^\circ$ , and rotation amplitude was $60^\circ$ [28]. . . . .	42
2.10 2D Global and body frames. . . . .	45
2.11 Simulation data showing the comparison of the flight path, pitch, and angle of attack of an FWMAV with the inclusion of the moment caused by the tail force in the $x$ direction vs an FWMAV without the moment. Figure 2.11a shows the flight path of the FWMAV with the addition of the moment caused by the tail's $x$ force. Figure 2.11b shows the pitch and angles of attack of the FWMAV with the addition of the moment caused by the tail's $x$ force. Figure 2.11c shows the flight path of the FWMAV without the addition of the moment caused by the tail's $x$ force. Figure 2.11d shows the pitch and angles of attack of the FWMAV without the addition of the moment caused by the tail's $x$ force. . . . .	47
3.1 Rectangular wing used in the initial flight simulations. . . . .	49

3.2	Baseline wing kinematics for 1 period used to explore the effects of variations in the stroke angle amplitude and rotation angle amplitude. The stroke angle oscillates around $0^\circ$ , with a magnitude of $90^\circ$ and the rotation angle oscillates around $-5^\circ$ with an amplitude of $30^\circ$ . . . . .	50
3.3	Baseline simulation data, with conventions from Figure 2.4, used to compare with the adjusted kinematics and adjusted wing shapes. Figure 3.3a shows the FWMAV's position in the global frame vs time. Figure 3.3b shows the FWMAV's flapping forces in the body frame vs time. Figure 3.3c shows the FWMAV's velocity in the global frame vs time. Figure 3.3d shows the FWMAV's pitch angle and the tail's angle of attack vs time. . . . .	51
3.4	The different wing shapes used overlaid onto each other. Each wing has the same area, aspect ratio, and length. . . . .	52



3.6 Simulation data when the wing stroke amplitude was  $60^\circ$  (lower) and  $120^\circ$  (higher) instead of the baseline  $90^\circ$  and all other parameters were held constant. Figure 3.6a shows the FWMAV's position in the global frame vs time. Figure 3.6b shows the FWMAV's flapping forces in the body frame vs time, with an expanded view shown in Figure A.2. Figure 3.6c shows the FWMAV's velocity in the global frame vs time. Figure 3.6d shows the FWMAV's pitch angle and the tail's angle of attack vs time. Here, the FWMAV with the larger stroke amplitude experienced higher initial forces, but this caused the FWMAV to pitch downwards, ultimately leading to the majority of the movement happening along the  $y$  axis. When the stroke angle is smaller, there are smaller forces and moments generated from flapping, leading to less pitch deviation and a trajectory that appears similar to gliding.

3.7 Simulation data when the wing rotation amplitude was 40° (higher) and 20° (lower) instead of the baseline 30° and all other parameters were held constant. Figure 3.7a shows the FWMAV’s position in the global frame vs time. Figure 3.7b shows the FWMAV’s flapping forces in the body frame vs time, with an expanded view shown in Figure A.3. Figure 3.7c shows the FWMAV’s velocity in the global frame vs time. Figure 3.7d shows the FWMAV’s pitch angle and the tail’s angle of attack vs time. The effects from the changes in the rotation angle were less impactful than changes in the stroke angle seen in Figure 3.6. The velocities, positions, rotations, and rotation rates all followed similar trends and were close to each other throughout the simulation. . . . .	58
3.8 Forces and moments from a 0.152 meter long rectangular wing in a wind speed of 2 m/s flapping at different frequencies for 1 period. Figure 3.8a shows the wing flapping at 5 Hz, Figure 3.8b shows the wing flapping at 10 Hz, and Figure 3.8c shows the wing flapping at 20 Hz. . . . .	60





3.12 Flight data from a 6-second simulation when the FWMAV is gliding. Figure 3.12a shows the flight path of the FWMAV, with an expanded view in Figure A.7a. Figure 3.12b shows the flapping forces in the body frame vs time with an expanded view in Figure A.7b. Figure 3.12c shows the velocity in the global frame vs time with an expanded view in Figure A.8a. Figure 3.12d shows the pitch angle and the tail's angle of attack vs time with an expanded view in Figure A.8b. Compared to the flapping simulation in Figure 3.11, there are no high-frequency oscillations because there is no flapping motion. Without flapping, the tail quickly stabilizes the FWMAV and reaches an angle of attack of $0^\circ$ .	71
4.1 Image of the Zing Avatar Banshee.	75
4.2 Film stills of slow-motion video capturing the flapping motion of the Zing Avatar Banshee. The first image shows the beginning of the downstroke, with the time underneath, and the last image shows the end of the upstroke.	75
4.3 The trapezoidal wing approximation used in the model verification overlaid onto the wing of the Zing Avatar Banshee. . .	76

4.4 Initial flight test comparison of the purchased FWMAV to the simulation. Figure 4.4a shows the flight path. Figure 4.4b shows the $x$ velocity in the global frame vs time. Figure 4.4c shows the $z$ velocity in the global frame vs time, where the $z$ axis used to record the flight data corresponds to the $y$ axis in Figure 2.3. Figure 4.4d shows the pitch vs time. Figure 4.4e shows the pitch rate vs time. In this flight, the FWMAV was equipped solely with tracking markers and had flexible and compliant wings. . . . .	79
4.5 Zing Avatar Banshee equipped with carbon fiber chords. The carbon fiber chords increased the rigidity of the wing without adding significant weight. . . . .	83
4.6 Initial comparison between the simulation and the recorded data with the Zing Avatar Banshee with carbon fiber chords along the wing. Figure 4.6a shows the flight path, Figure 4.6b shows the $x$ velocity in the global frame vs time, Figure 4.6c shows the $z$ velocity in the global frame vs time, Figure 4.6d shows the pitch and body's angle of attack vs time, and Figure 4.6e shows the pitch rate vs time. In this simulation, the wing kinematics started with an immediate upstroke and did not model the flight of the Zing Avatar Banshee correctly. . . . .	86

4.7 The average trial and comparison between simulation data and flight data. Figure 4.7a shows the flight path, Figure 4.7b shows the $x$ velocity in the global frame vs time, Figure 4.7c shows the $z$ velocity in the global frame vs time, Figure 4.7d shows the pitch and body's angle of attack vs time, and Figure 4.7e shows the pitch rate vs time. This simulation roughly emulates the motion of the FWMAV. . . . .	88
4.8 The best comparison between simulation data and flight data. Figure 4.8a shows the flight path, Figure 4.8b shows the $x$ velocity in the global frame vs time, Figure 4.8c shows the $z$ velocity in the global frame vs time, Figure 4.8d shows the pitch and body's angle of attack vs time, and Figure 4.8e shows the pitch rate vs time. Here, the simulation predicted the motion and orientation of the FWMAV most accurately. . . .	90

## 4.9 The worst comparison between simulation data and flight data.

Figure 4.9a shows the flight path, Figure 4.9b shows the  $x$  velocity in the global frame vs time, Figure 4.9c shows the  $z$  velocity in the global frame vs time, Figure 4.9d shows the pitch and body's angle of attack vs time, and Figure 4.9e shows the pitch rate vs time. In this simulation, the model performed significantly worse than the projectile motion simulation in predicting the trajectory of the FWMAV. The simulation also did not capture the pitch pattern of the flight data, having a significant decrease before pitching upwards. . . . . . . . . . . . 92

A.1	Expanded image of the flapping forces seen in Figure 3.5b. . .	103
A.2	Expanded image of the flapping forces seen in Figure 3.6b. . .	104
A.3	Expanded image of the flapping forces seen in Figure 3.7b. . .	105
A.4	Expanded image of the flapping forces seen in Figure 3.9b. . .	106

# Nomenclature

$\alpha$  Angle of Attack

$\beta_{wing}$  Stroke Plane Angle of the Wing

$\phi_0$  Average Rotation/Pitch Angle of the Wing

$\phi_{amp}$  Amplitude of Rotation/Pitch Angle of the Wing

$\phi_{wing}$  Stroke Angle of the Wing

$\psi_0$  Average Rotation/Pitch Angle of the Wing

$\psi_{amp}$  Amplitude of Rotation/Pitch Angle of the Wing

$\psi_{wing}$  Deviation Angle of the Wing

$\rho$  Density of Air

$\theta_0$  Average Rotation/Pitch Angle of the Wing

$\theta_{amp}$  Amplitude of Rotation/Pitch Angle of the Wing

$\theta_{tail}$  Tail Angle

$\theta_{wing}$  Rotation/Pitch Angle of the Wing

$AR$  Aspect Ratio of the Wing/Tail

$C_A$  Added Mass Coefficient

$C_D$  Drag Coefficient

$C_L$  Lift Coefficient

$C_M$  Moment Coefficient

$C_R$  Rotation Coefficient

$f$  Flapping Frequency

$g$  Gravitational Constant

$J$  Advance Ratio

$J_{body}$  Moment of Inertia of the Body

$L_{body}$  Length of the Body

$m_{body}$  Mass of the FWMAV

$q_d$  Dynamic Pressure

$R, L_{wing}$  Length of the Wing

$r_{tail}$  Distance from Center of Mass to Tail Center of Pressure

$r_{wing}$  Distance from Center of Mass to Wing Shoulder

# Introduction

## 1.1 Motivation

In recent years, the field of robotics has seen remarkable advancements, leading to the development of sophisticated aerial vehicles capable of mimicking the highly efficient and maneuverable flight patterns of various insects and birds. The pursuit of efficient and versatile flight has led researchers to explore novel approaches in aerial vehicle design, such as ornithopters, VTOL (vertical takeoff and landing) drones, and UAVs (unmanned aerial vehicles). Due to their lightweight nature and modulation of their wing kinematics, many insects and small birds exhibit high lift-to-power ratios, enhanced agility, and increased flight efficiency [1]. By looking at these biological systems, flapping winged robots have emerged as a promising avenue for achieving enhanced performances in flight, endurance, and maneuverability [2] [3]. Many birds and large insects exhibit intermittent active (i.e. flapping) and passive (i.e. gliding, bounding, or soaring) flight, which has been found to lead to significant energy savings when compared to continuous flapping flight methods at most speeds [2]. Compared with continuous flapping, flap-gliding is considerably more energy-efficient during slow flight, and flap-bounding is more energy-efficient during fast flight. A flapping-wing micro-air vehicle (FW-

MAV) capable of both active (flapping) and passive (gliding) flight that can seamlessly transition between the two at appropriate times would greatly increase the energy efficiency of the FWMAV.

This thesis addresses the development of an open-source simulation environment for the Cooper Union Bio-Inspired Robotics Design (CUBIRD) FWMAV being currently developed. The overall goal of the CUBIRD FWMAV project is to develop a roughly 30-gram, low-cost, and easily accessible FWMAV. There are two ideologies behind this, to research energy conservation methods in flyers, particularly flap and glide, and allow FWMAVs to become more accessible to hobbyists. There is a lack of open-source resources that can be used by a regular person who wants to develop their own FWMAV from scratch, compared to rotary drones or fixed-wing drones. A simple Google search for DIY drones will give hundreds of tutorials for developing fixed-wing<sup>1</sup> or rotary drones<sup>2</sup>, but there are no DIY FWMAV tutorials. This might be due to the lower interest in FWMAV's but is certainly due to the impact that the design of an FWMAV has on a controller that is implemented. The physics simulation being developed is the first step of the process to allow the average person to design, test, and control their own FWMAV with relative ease.

One major difficulty in the development of FWMAVs is the lack of open-source software to develop physics simulations and control methods. Each

---

<sup>1</sup><https://www.instructables.com/Pi-Zero-Plane-a-150-Smart-Fixed-Wing-Drone-With-th/>

<sup>2</sup><https://www.instructables.com/The-Ultimate-Guide-to-Building-a-Quadcopter-From-S/>

of the FWMAVs mentioned before developed their simulation environments independently of each other and had to tailor their models to their unique robot. This may involve using the results from wind tunnel testing to model the behavior or the use of machine learning that takes in test flight data to generate the governing dynamics equations [4]. In addition, most conference papers focus on one of two major components, the physical design of the FWMAV, or control methods, often glancing over the development of their simulation environment [5] [6] [7] [8]. While many authors include the relevant dynamics equations in their papers, they often lack any figures or results that would allow an outsider to follow their process and reproduce their results. An additional challenge is that many papers related to flapping wing aerodynamics focus on the act of hovering rather than forward flight. Although forward flight and hovering are both caused by the flapping of wings, the aerodynamics change significantly once the body starts to move. Hovering tends to rely on the vortices generated through the rotation of the wing. On the other hand, forward flight relies on the quasi-steady assumption that the instantaneous aerodynamic forces on the flapping wing are assumed to be those which the wing would experience in steady motion at the same instantaneous speed and angle of attack [9]. Therefore the typical models used to simulate hovering motion may not be suitable for forward flight. This thesis plans to address the two areas that are often overlooked, the top-down implementation of a flapping wing aerodynamic model that can be

adjustable to various-sized FWMAVs, and the lack of open-source simulation environments in the FWMAV field.

## 1.2 Intermittent Flight

While flapping flight offers improved maneuverability and agility compared to fixed-wing flight [10], fixed-wing flight outperforms flapping-wing flight for steady, level flight. This has led to increased interest and research in intermittent flight, which combines the advantages of flapping flight and fixed-wing flight. Intermittent flight in birds has been widely studied for several decades and has been shown to increase energy efficiency [11] [12]. There is a strong correlation between the size of the flyer and the use of intermittent flight [13]. Small birds, categorized as less than 30g with low aspect ratios, use flap-bounding methods exclusively. Medium-sized birds, those with body mass less than 300g or that have pointed wings with high aspect ratios, use both flap-gliding and flap-bounding flight. Lastly, large birds, those weighing more than 300g, use flap-gliding exclusively. There are a variety of birds that use intermittent glides at slow speeds and switch to intermittent bounding at high speeds. Irrespective of the scale of the aerial vehicle, a consistent phenomenon prevails: flapping motion is commonly complemented with another form of movement. While flapping allows for enhanced maneuverability, each flap results in energy loss due to the elastic deformation in the wing during the upstroke and downstroke, with studies showing that the wing might re-

cover only 80% of the bending energy during the flapping motion [13]. It is therefore of interest to reduce the number of flaps that an FWMAV performs over a flight through the use of intermittent flapping, which will ultimately conserve energy. While fixed-wing flyers will also experience elastic deformation in the wings, it is to a significantly lesser degree than flapping-wing flyers. There is an opportunity to conserve some of that lost energy caused by flapping through the use of intermittent flapping. Flapping less often will lead to less energy being lost due to elastic deformation.

Intermittent flight allows for an FWMAV to take advantage of fixed-wing and flapping-wing air vehicles, conserving energy during a gliding phase, and having enhanced maneuverability during the flapping phase. Modern airplanes are particularly effective for steady, level flight, with propellers or jet engines producing the necessary thrust, and various control surfaces such as ailerons, rudders, and elevators allowing for slight changes in altitude or attitude. An FWMAV does not necessarily have the same control surfaces as a fixed-wing aircraft, so to achieve control over pitch, yaw, and roll, it must be able to flap its wings at different frequencies, which control the movement and rotation of the FWMAV. The gliding aerodynamic theory of a fixed-wing aircraft can be applied to the gliding stage of an FWMAV, but different aerodynamic methods must be applied during the flapping stage to accurately simulate and control flapping flight.

### 1.3 FWMAV Dynamical Model

While there are robust dynamic simulations and models for fixed-wing aircrafts, modeling the dynamics of the FWMAV is not quite as simple due to the increased complexity of flapping. Common fixed-wing MAVs and rotary MAVs (helicopters) have had their aerodynamics well studied and have existed in a commercial setting for far longer than FWMAVs. In order to accurately simulate an FWMAV, mathematical models have to be created for multiple systems that all must interact with each other: wing aerodynamics, body dynamics, actuator dynamics, sensors, external environment, and flight control algorithms [14]. The body dynamics model is usually the same in most models, implementing Newton's second law and Euler's laws of motion for rigid bodies, while the other subsystems typically vary from model to model and depend on the physical design of the FWMAV being analyzed [15]. Different FWMAVs will have different transmission systems, different wing shapes, and different sensors on board that will all require their unique models to correctly simulate the behavior. These systems must all work together, passing information between each other to create the simulation. Because of this, each system must be modeled with the necessary accuracy, to capture the true behavior of the FWMAV, otherwise, the simulation will produce undesirable results, leading to incorrect controller implementation.

Creating an FWMAV is a lengthy process that consists of designing the

physical robot, developing a simulation environment, and developing control methods to allow the FWMAV to fly. There are many FWMAVs in existence today various masses, wing spans, and flapping frequencies that use different techniques to fly. The Harvard RoboBee is a small-scale FWMAV weighing less than one-tenth of a gram that uses a passive wing hinge to adjust the angle of attack during the stroke [2]. The Harvard RoboBee hovers and moves forward by adjusting its pitch, similar to a quadcopter. The TU Delft DelFly has three models, the DelFly Micro weighing 3 grams, the DelFly Explorer weighing 20 grams, and the DelFly Nimble weighing 30 grams, which all use clap-and-fling effects using a pair of wings on either side of the body <sup>3</sup> [16] [4]. The Dove, being developed by Northwestern Polytechnic Institute, is a 220-gram robot that uses the typical 2 wings seen on birds to fly [17]. Each robot's simulation environment had to be uniquely designed due to the different sizes of the mass and wingspan of flyers as well as the different flying mechanisms each of these robots exhibit. These are only some of the many examples of FWMAVs currently being developed, but highlight the disparity in sizes and flapping mechanisms. While researchers have gone into detail explaining the aerodynamic models used in simulation, many rely on empirically fit data rather than an all-encompassing model [4]. The difference in the sizes of these robots and uniquely tailored physics models demonstrates the need for an all-encompassing design tool that can effectively model various sized and

---

<sup>3</sup><https://www.delfly.nl/home/>

shaped FWMAVs.

### 1.3.1 Aerodynamics

Modeling the aerodynamics of an FWMAV is a complex task due to the changing aerodynamic properties of gliding and flapping due to elastic deformation in the wings and leading-edge vortices [11] [13]. The elastic deformation in the wings and the leading-edge vortices produced and their respective effects on thrust and drag forces are particularly difficult to model and vary significantly depending on the size and shape of the wing, specifically with changes in the location of the pitching axis, aspect ratio, and leading-edge profile [18]. There are two main types of aerodynamic models, quasi-steady and unsteady. Quasi-steady models assume that the aerodynamic forces and moments acting on an object remain constant over small time intervals. It simplifies the analysis by treating the aerodynamic forces as though they are steady, even though the actual flow around the object may be changing over time. Unsteady models, on the other hand, explicitly account for the time-varying nature of aerodynamic forces and moments. Unsteady aerodynamic models incorporate the complex interactions between the object and the surrounding airflow as they evolve over time, providing a more accurate representation of aerodynamic behavior at the cost of higher computational costs, therefore not being suitable for dynamic and control purposes [19]. The quasi-steady models and unsteady models are often not in agreement with

each other, producing different forces and moments, with unsteady models producing higher accuracy by including effects from the rotation of the wing, wake capture, and added-mass effects. Models that combine the accuracy of unsteady models and the lower computational speeds of quasi-steady models still require a higher computational cost than traditional quasi-steady models but have the potential to be utilized for controller design due to their increased accuracy[19].

Due to the complex aerodynamic force calculations, there are a variety of methods used to approximate the thrust and drag forces such as CFD simulations [18], using testbench data [4], using averaged dynamics over the duration of one flap, as well as quasi-steady and unsteady models mentioned previously. CFD simulations offer high accuracy and allow for calculations to be done without building a physical prototype, but it is often highly computationally demanding. CFD relies on dividing the wing into small pieces and calculating the aerodynamics of each segment. Many aerodynamic mathematical models can be applied, taking into account complex aerodynamic properties such as leading-edge vortexes, different flow regimes, and wake capture, as well as changes in the shape of the wing due to elastic deformation, but doing so would be computationally heavy, and would not be suitable for use with controller design. Using testbench data is the most accurate way of understanding and recording behavior, but this is often in a controlled environment and small adjustments to the physical design of the FWMAV can

alter recorded results. Using the averaged dynamics over time is the most simple method, where a simple mathematical function is used to model the thrust and drag forces where the average force produced during one flapping cycle is equivalent to the average force during one cycle recorded from test bench data. Averaged dynamic forces result in a less accurate model, but is computationally lighter and can be suitable if high levels of precision are not necessary. The goal of creating the physics simulation detailed in this thesis is to allow for the testing of various FWMAV designs without needing to physically build a robot, so using test bench data or averaged dynamics is illogical. For the simulation being developed a model that combines the quasi-steady and unsteady models is being used because it will have reduced computational time, accurate aerodynamic models, and possesses the ability to be adjusted to different FWMAVs without the need to collect testbench data.

### 1.3.2 Simulation Organization

The structure of the code developed for the physics simulation of flapping wing robots is designed with usability and adaptability in mind, ensuring that future students and researchers can easily integrate it into the CUBIRD FW-MAV project or their own hobbyist projects. The code architecture revolves around modularity, with multiple files interconnecting to facilitate efficient adjustments and enhancements.

At its core, a primary file houses all essential parameters pertinent to both the FWMAV and the simulation itself, providing a centralized repository for easy reference and modification. Another crucial component is the Wing-Shape class, residing within its dedicated file, which encapsulates functions responsible for defining the wing's shape. Specifically, two pivotal functions, concerning the leading edge and chord length, can be readily altered to accommodate variations in wing configurations, thereby allowing users to tailor the simulation to their specific needs.

Further augmenting the code's flexibility are specialized files dedicated to crucial aspects such as wing dynamics, tail forces, and body forces. These files encapsulate functions responsible for calculating forces, kinematics, and aerodynamic properties, offering users the flexibility to update them with relevant equations and parameters as necessary. Additionally, a file detailing the derivatives of the system's state, derived from fundamental equations of motion, ensures accurate representation and simulation fidelity.

The numerical solver, contained within its designated file, provides the computational backbone for simulating the system dynamics, while a separate simulation function orchestrates the integration of initial conditions and the numerical solver, returning arrays of system states, forces, and angles of attack. Finally, a dedicated file for data visualization and graphing enables users to interpret and analyze simulation results effectively.

Overall, this structured approach not only facilitates the development and

refinement of the simulation but also ensures accessibility and ease of use for future researchers and developers within the FWMAV project and beyond.

## 1.4 Active Control

Intermittent flight in birds has been shown to result in increased flight range, endurance, and energy conservation, but this flight mode poses difficulties in control system design, specifically in the control of transitions between gliding and flapping. The dynamics of the system vary significantly between the two modes. While flapping, the aerodynamic forces and moments vary periodically and change nonlinearly with changes in flight speed and the angle of attack. While gliding, the forces and torque vary linearly with small changes in speed or angle of attack and will therefore have different equations and models than flapping. Additionally, FWMAVs are affected by external disturbances, such as wind, further complicating controller design. Typical fixed-wing aircrafts travel at speeds significantly greater than the wind speed and are passively stable, so small wind gusts are not as drastic on the aircraft. With smaller-scale aircraft, such as FWMAVs traveling at low speeds, those same wind gusts will cause a larger disturbance in the trajectory and orientation of the vehicle, requiring more advanced control methods to compensate. An additional complexity for FWMAV's is that they are passively unstable, leading to larger effects from disturbances, and necessitating the need for a robust controller. Traditional PID control is not well-suited as

an optimal control method [20] because of the inability of a PID controller to retune its parameters if there are disturbances, but recent developments in the field have led to the emergence of more viable control methods such as Active Disturbance Rejection Control (ADRC), sliding mode control, and more recently, neural network control [21]. The idea behind ADRC is to actively eliminate disturbances that affect the behavior of the system by using real-time measurements to estimate disturbances instead of relying solely on system-based modeling and compensation techniques such as PID control [20]. Sliding mode control relies on two modes, sliding mode and switching mode. Sliding mode drives the system toward a desired range, the sliding surface, where the system's behavior is constrained, and the switching mode adjusts different control actions to maintain the system on the sliding surface. Neural network control uses artificial neural networks (ANNs) as part of control systems to regulate the behavior of the system. These networks learn to approximate the control law or system dynamics based on input-output data, enabling adaptive and often nonlinear control strategies.

## 1.5 Outline

The simulation being developed is adaptable to FWMAV of various sizes, having the ability to adjust the critical dimensions of the robot, as well as the shapes of the wings. This will allow for users to test adjustments for the center of mass, the wing shape, the tail position, and any other parameters without

having to build a new FWMAV each iteration. Developing an adaptable physics simulation that can accurately simulate different FWMAVs is the first step in the CUBIRD mission of providing easier access for individuals to create their own FWMAVs.

The subsequent chapters of this thesis will delve into the intricacies of the simulation framework and its applications:

- 1. Model Development:** This chapter will provide a comprehensive overview of the dynamic equations governing FWMAV flight and the aerodynamic models incorporated into the simulation.
- 2. Simulation Results:** Here, the effects of different key parameters of an FWMAV, such as the flapping frequency, wing shape, and wing kinematics, will be simulated and analyzed. Additionally, a simulation of a flapping FWMAV will be compared to the same FWMAV while gliding.
- 3. Model Verification:** Following the discussion of the physics behind the simulation, this chapter will focus on the validation process undertaken to ensure the accuracy and reliability of the developed physics model. Various methods used to validate the simulation against empirical data will be outlined and discussed. The limitations of the simulation framework will be meticulously examined, providing insights into its capabilities and areas for improvement.
- 4. Future Work and Conclusion:** The final chapter will outline the

envisioned future steps in the CUBIRD project, explaining potential areas for further research, development, and innovation. This section will offer a roadmap for advancing FWMAV technology and the simulation framework introduced in this thesis.

# Physics Model Development

## 2.1 Introduction

Before delving into the details of the physics simulation, it's crucial to understand the flow that drives its functionality. To model and predict the trajectory of any object, two conditions must be known, the instantaneous state of the object, and the forces and moments acting on the object. The state contains information that fully defines the instantaneous configuration and motion of the object for any given instant in time. The forces acting on the object can be utilized with Newton's second law to determine the rate of change of the state. In a two-dimensional rigid body simulation with three degrees of freedom, two translational and one rotational, there are six states: x position, y position, rotation angle, x velocity, y velocity, and angular velocity. In three dimensions, there are six degrees of freedom, three translation and three rotational, and 12 total states due to the added degrees of freedom. Updating these states over time relies on numerical integration, which requires knowledge of second derivatives of position and rotation derived from Newton's second law. The simulation's fidelity hinges on accurately representing the forces and moments that are used in Newton's second law, including gravitational effects, aerodynamic forces and moments from

flapping wings, and aerodynamic forces exerted by the tail.

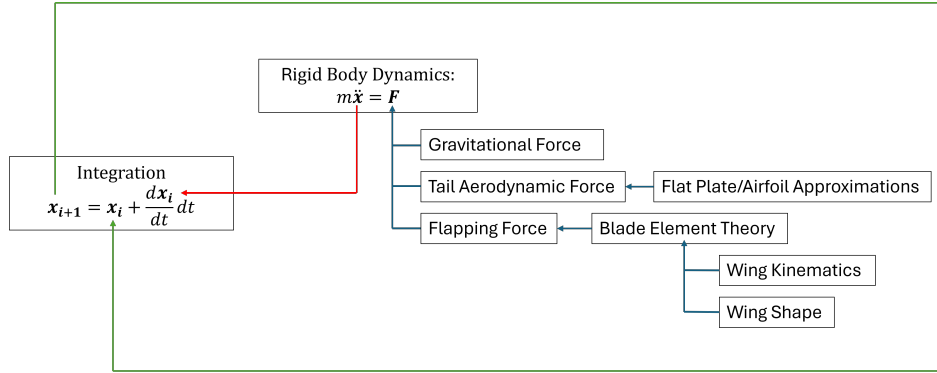


Figure 2.1: Flow diagram for the simulation.

Figure 2.1 shows a process flow of the simulation. The main objective of the simulation is to predict the state of the object at the subsequent time step through the process of numerical integration. This integration step is repeated over and over until the simulation concludes, ensuring high degrees of accuracy and the correct modeling of the unsteady aerodynamics.

To implement the numerical integration, the second derivatives of position and rotation are required and are derived from Newton's second law, depicted by the red arrow. However, to apply Newton's laws effectively, the forces and moments acting upon our object must be known. In this case, these forces originate from gravity, the flapping wings, and the tail. Calculating the flapping force involves employing blade element theory, a methodology used to break down the wing into chord-wise strips to better estimate the aerodynamic forces. Because the tail is not flapping, a different approach must be used to calculate the aerodynamic forces on the tail. The tail's model utilizes modified airfoil and flat plate aerodynamic calculations, that

allow for tails with different aspect ratios to be accounted for correctly.

In the simulation, there are three assumptions that are made to help simplify the physics. The first is that the motor will perfectly control the flapping kinematics of the wing. This entails that the motor will always be operating at 100% and there is no start-up time or changes in the flapping motion due to air resistance. A properly chosen motor should output enough torque to overcome any air resistance forces and maintain the same wing kinematic profile over the duration of the simulation. It is also assumed that the wing will be rigid and the rotation angle formula will take into account small flexes along the wing by incorporating them into its kinematic formulas, not requiring separate equations regarding the elasticity. Lastly, the wings are assumed to be massless, due to the wings making up a small percentage of the total weight of the robot, some as small as 0.1% [22], and will have no inertial effects on the movement of the FWMAV.

## 2.2 Equations of Motion

The FWMAV model can be broken down into three separate models that when combined, accurately simulate the trajectory of the FWMAV. These are the rigid body dynamics which describes the motion of the body using the forces acting upon it, the flapping aerodynamics which calculate the forces generated during flapping, and the gliding aerodynamics which are used to calculate the forces on the tail and on the wings during a gliding phase.

The rigid body dynamics govern the overall motion of the body and follow Newton’s second law, for translation and rotation. Although the FWMAV is not a true rigid body, deformations in the main body of the vehicle are negligible, and therefore, the rigid body assumption is valid. The parameters that can be adjusted here include the total mass and the location of the center of mass, the moment of inertia, the force inputs, the moment inputs, and the initial conditions.

The flapping aerodynamics uses blade-element theory to estimate the forces and moments produced during the flapping motion that can be used in rigid body dynamics to simulate the effects of flapping [23]. The blade element theory uses rigid body dynamics, modeling the wings as rigid plates, which is a major assumption for flapping wings since many flyers have wings that change morphology depending on the flight conditions. In nature, there is a large variety of the types of wings of flyers. Insects typically have rigid wings, while birds have flexible wings that change morphology during flight [[24]]. The wings being developed for the CUBIRD will be inspired by insects and will be relatively rigid, therefore the rigid wing assumption used for the blade element theory is satisfactory. The main physical parameters that are adjustable in this model are the wing kinematics, the wing shape, and the flapping frequency.

Biological flyers generate lift and control torques entirely through the manipulation of their wings, creating flapping motion with multiple degrees of

freedom. The principal rotations that generate the flapping motion are the stroke-plane angle, the wing flapping stroke, the wing rotation (pitch), and the wing deviation, as seen in Figure 2.2. The stroke plane ( $\beta$ ) is the plane upon which the flapping motion takes place. The flapping stroke angle ( $\phi$ ) is the main back-and-forth rotation along the stroke plane. The pitch ( $\theta$ ) is the angle at which the wing is rotated relative to the stroke plane, which causes increases or decreases in the angle of attack during the flapping process. The deviation angle ( $\psi$ ) is the angle at which the rotational axis is offset from the stroke plane. These four angles and their respective functions define the wing kinematics of an FWMAV.

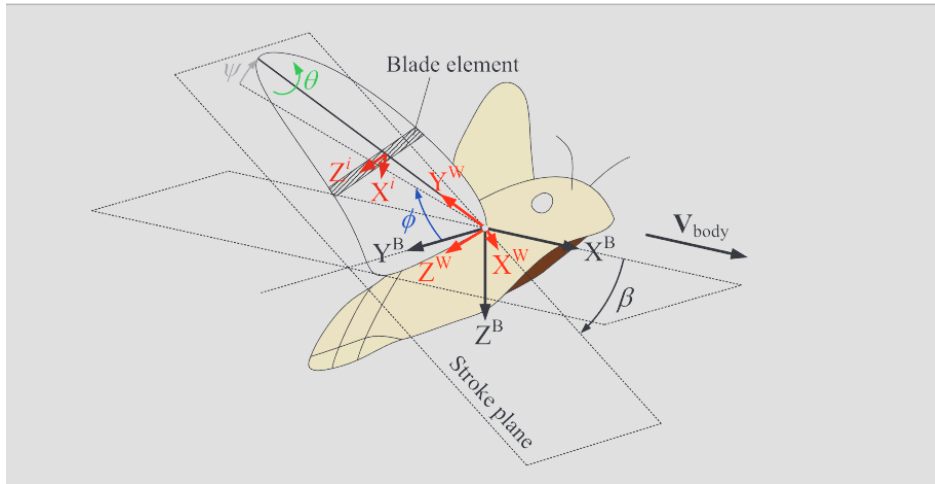


Figure 2.2: Wing kinematics and reference angles for a flapping wing. [23].

On the other hand, the gliding aerodynamics uses nonlinear equations to calculate the aerodynamic forces that occur in the tail and in the wings when the FWMAV is gliding. The gliding aerodynamics utilize airfoil approximations for small angles of attack, and flat plate approximations as the angle of

attack grows, capturing stall effects. The physical parameters that affect the aerodynamic force are the aspect ratio of the surface, the surface area, and drag and lift forces for an angle of attack of  $0^\circ$ .

### 2.2.1 Reference Frames

In the simulation of FWMAVs, various reference frames are employed to accurately model the dynamics of flight. These frames serve as coordinate systems relative to which forces and motions are defined and transformed. Understanding these frames is essential for comprehending the simulation's mathematical formulation and its connection to real-world dynamics. Figure 2.3 shows some of the reference frames used in the simulation. The black axes, denoted by  $x_{global}$  and  $y_{global}$  represent the global frame. The red axes, denoted by  $x_{body}$  and  $y_{body}$  show the body frame. The green axes, denoted by  $x_{tail}$  and  $y_{tail}$  represent the tail frame. Finally, the blue axes, denoted by  $x_{stability}$  and  $y_{stability}$  represent the tail's stability frame.

#### Global Frame

The global frame provides a reference relative to the external environment and serves as the frame used in the rigid body dynamics. The global frame is a static frame in which the FWMAV moves. The position and pitch of the FWMAV are calculated in this frame, which can be seen in Figure 2.3, where  $X$  and  $Y$  are the horizontal and vertical distances, and  $\theta$  is the pitch angle with respect to the  $x$ -axis.

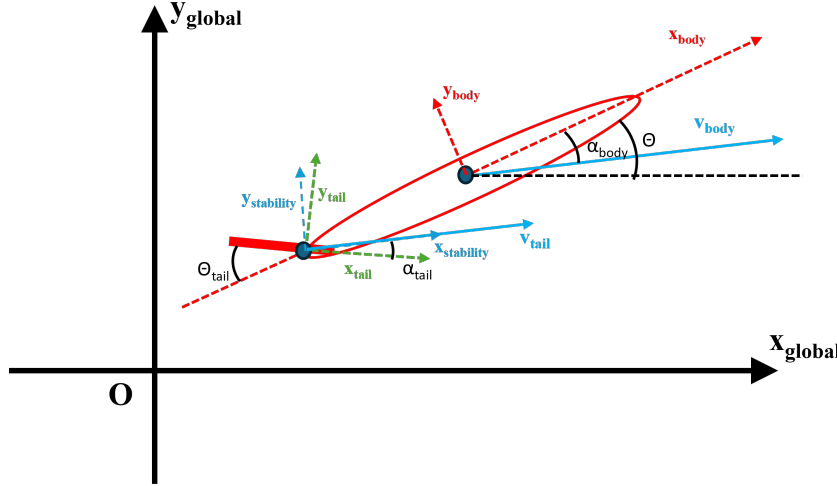


Figure 2.3: 2D global frame, body frame, tail frame, and tail stability frame.

### Body Frame

The body frame is a local frame fixed relative to the FWMAV's body, shown in Figure 2.3. Expressing the forces in the body frame is beneficial as it allows for the moments caused by offset forces to be calculated with ease. Since the rigid body dynamics are applied in the global frame, the forces need to be transformed through a rotation matrix, rotating by the pitch angle  $\theta$ , to represent the body forces in the global frame. The conversion of the forces in the body frame to the global frame is

$$\begin{bmatrix} F_x^{Global} \\ F_y^{Global} \end{bmatrix} = \begin{bmatrix} \cos \theta & -\sin \theta \\ \sin \theta & \cos \theta \end{bmatrix} \begin{bmatrix} F_x^{body} \\ F_y^{body} \end{bmatrix} \quad (2.1)$$

## Tail Frame

The tail frame, shown in Figure 2.3 is a local frame fixed relative to the vehicle's tail, which is the frame in which the tail's aerodynamic forces are expressed. The tail's aerodynamic forces are converted to the body frame by rotating by the tail angle,  $\theta_{tail}$ . The conversion of the forces in the tail frame to the body frame is given as

$$\begin{bmatrix} F_x^{body} \\ F_y^{body} \end{bmatrix} = \begin{bmatrix} \cos \theta_{tail} & \sin \theta_{tail} \\ -\sin \theta_{tail} & \cos \theta_{tail} \end{bmatrix} \begin{bmatrix} F_x^{tail} \\ F_y^{tail} \end{bmatrix} \quad (2.2)$$

## Stability Frame

The stability frame is a local frame centered at the aerodynamic surface's center of pressure pointing in the direction of the velocity of the FWMAV, shown in Figure 2.3. In this frame, the lift and drag forces are initially expressed, with the drag force always being in the opposite direction of the velocity, before being rotated to the aerodynamic surface's frame by a rotation about the angle of attack,  $\alpha$ . These forces are directly related to the FWMAV's velocity and orientation relative to its surroundings. The conversion of the lift and drag forces in the stability frame to the aerodynamic surface's frame is given by

$$\begin{bmatrix} F_x^{surface} \\ F_y^{surface} \end{bmatrix} = \begin{bmatrix} \cos \alpha & \sin \alpha \\ -\sin \alpha & \cos \alpha \end{bmatrix} \begin{bmatrix} -F_{drag} \\ F_{lift} \end{bmatrix} \quad (2.3)$$

## Wing Frame

The wing frame, shown in Figure 2.2 and Figure 2.6, is a local frame fixed relative to the vehicle's wing structure. The wing flapping force is initially calculated in this frame, considering aerodynamic principles and wing kinematics, before being transformed into the body frame. The details of these rotations will be discussed in the Aerodynamic Flapping Forces section.

### 2.2.2 Rigid Body Dynamics Equations

The dynamics of the system are governed by the equations of motion that are found using Newton's second law  $ma = \sum F$  and  $I\alpha = \sum M$  by applying it to each degree of freedom,  $x$ ,  $y$ , and  $\theta$ , in the ground-fixed frame as seen in Figure 2.4. In this figure, the forces from the wing and tail, calculated to be in the body and tail frame respectively, are shown in their final form used for Newton's second law, the global frame. In the previous equations,  $m$  is the mass of the body,  $a$  is the acceleration of the body,  $F$  is the force vectors acting on the body,  $I$  is the moment of inertia,  $\alpha$  is the angular acceleration, and  $M$  is the moments acting on the body. Three forces act on the FWMAV that cause motion: the gravitational force, the flapping wing force, and the aerodynamic tail force. The moments caused by these forces can be given as

$r \times F$  where  $r$  is the distance from the center of mass to the location of the force. The equations for the second derivatives of  $x$ ,  $y$ , and  $\theta$ , with forces expressed in the global frame, are

$$\ddot{x} = \frac{F_{wing-x} + F_{tail-x}}{m_{body}} \quad (2.4)$$

$$\ddot{y} = \frac{-m_{body}g + F_{wing-y} + F_{tail-y}}{m_{body}} \quad (2.5)$$

$$\ddot{\theta} = \frac{r_{wing} \times F_{wing} + r_{tail} \times F_{tail} + M_{wing-z}}{J_{body}} \quad (2.6)$$

where the forces and moments are expressed in the global frame and  $mg$  represents the force from gravity.

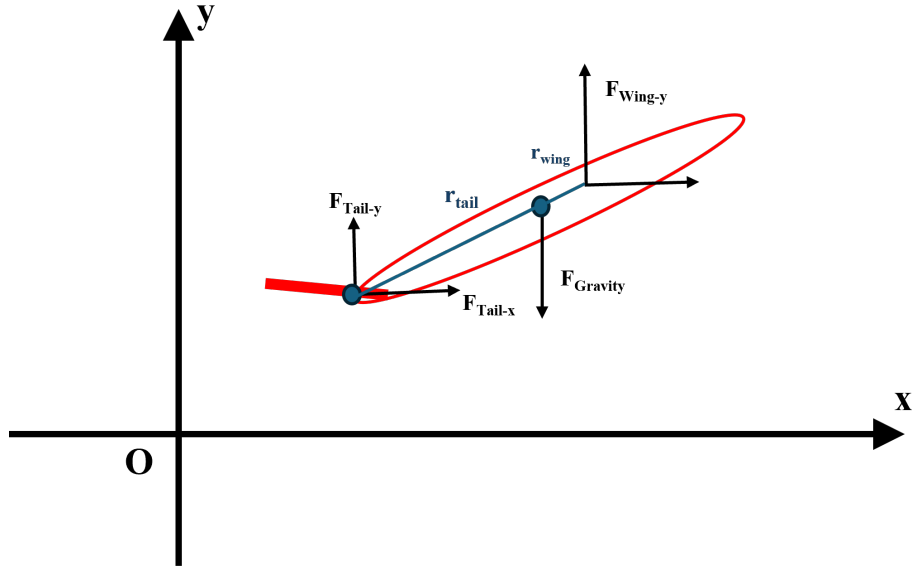


Figure 2.4: 2D global frame and forces shown in global frame.

### 2.2.3 Aerodynamic Gliding Forces

Modeling the aerodynamic forces generated while gliding is necessary to calculate the force contribution from the tail as well as modeling the FWMAV during a gliding phase. Lift and drag forces are typically expressed in the stability frame, the frame expressing the movement of the FWMAV in the  $x$ -axis exclusively, and are converted to the frame of the aerodynamic surface by a rotation around the angle of attack  $\alpha$ , where a separate  $\alpha$  exists for each surface. Figure 2.5 shows the tail and wing forces expressed in the tail frame and body frame respectively and the angle of attack of the overall FWMAV. The equations for the lift and drag forces expressed in the aerodynamic surface's frame are the same as equation 2.3 and are given as

$$F_x = -F_{drag} \cos(\alpha) + F_{lift} \sin(\alpha) \quad (2.7)$$

$$F_y = F_{drag} \sin(\alpha) + F_{lift} \cos(\alpha) \quad (2.8)$$

where

$$F_{lift} = C_L q_d \quad (2.9)$$

$$F_{drag} = C_D q_d \quad (2.10)$$

and

$$q_d = 0.5 \rho S v^2 \quad (2.11)$$

where  $q_d$  is the dynamic pressure,  $v$  is the magnitude of the velocity,  $S$  is

the surface area of the aerodynamic surface, and  $C_L$  and  $C_D$  are nonlinear functions for the lift and drag coefficients that are a function of  $\alpha$ .

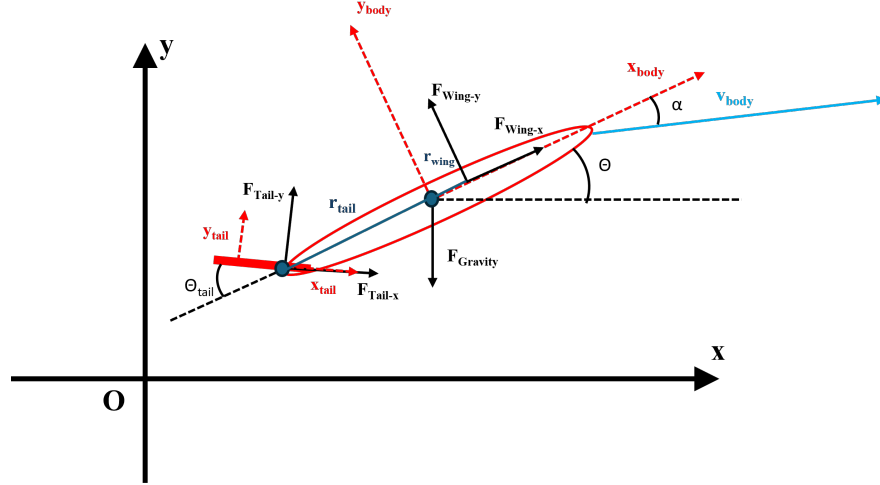


Figure 2.5: 2D global frame and forces shown in their calculated frames, the tail force is in the tail frame, and the wing force is in the body frame.

The angle of attack,  $\alpha$  is calculated in two different ways, depending on whether the tail or wing in gliding mode is being calculated. For the wing gliding, the equation in 2.30 is used, with the adjustment of having only one blade element. That formula takes into account the wing kinematics in the calculation of  $\alpha$  which is important because the wings might not be in a neutral position during gliding. For the tail's angle of attack, the inertial frame can be used and is shown in the following equation

$$\alpha = \theta - \tan^{-1}\left(\frac{\dot{y}_{tail}}{\dot{x}_{tail}}\right) - \theta_{tail} \quad (2.12)$$

where,

$$\dot{y}_{tail} = \dot{y} + \dot{\theta}r_{tail} \cos(\theta) \quad (2.13)$$

$$\dot{x}_{tail} = \dot{x} + \dot{\theta}r_{tail}(-\sin(\theta)) \quad (2.14)$$

and  $\dot{x}$ ,  $\dot{y}$ , and  $\theta$  are expressed in the global frame.

To convert the tail frame to the body frame, to be in line with the wing forces shown in Figure 2.5, a rotation must be done by the tail angle,  $\theta_{tail}$ . The equations for the tail's aerodynamic forces in the body frame are taken from equation 2.2 and are given as

$$F_x^B = F_x^T \cos(\theta_{tail}) + F_y^T \sin(\theta_{tail}) \quad (2.15)$$

$$F_y^B = -F_x^T \sin(\theta_{tail}) + F_y^T \cos(\theta_{tail}) \quad (2.16)$$

where the letters B and T represent the force, calculated by Equations 2.7 and 2.8, expressed in the body and tail frame.

The lift and drag models, used to calculate  $C_L$  and  $C_D$ , taken from literature [25], incorporate the effects of stall using a flat plate approximation, as well as parasitic and induced drag and initial lift coefficients at  $0^\circ$  angle of attacks. The lift coefficient equation is

$$C_L(\alpha) = (1 - \sigma(\alpha))[C_{L_0} + C_{L_\alpha}\alpha] + \sigma(\alpha)[2 \operatorname{sign}(\alpha) \sin^2(\alpha) \cos(\alpha)] \quad (2.17)$$

where  $\sigma(\alpha)$  is a blending function that will allow for the combination of airfoil approximations for low angles of attack and flat plate stall approximations

for large angles of attack and is given as

$$\sigma(\alpha) = \frac{1 + e^{-M(\alpha - \alpha_0)} + e^{M(\alpha + \alpha_0)}}{(1 + e^{-M(\alpha - \alpha_0)})(1 + e^{M(\alpha + \alpha_0)})} \quad (2.18)$$

where  $M$  and  $\alpha_0$  are positive constants representing the transition rate and the cutoff respectively. The linear lift coefficient  $C_{L_\alpha}$  is approximated as

$$C_{L_\alpha} = \frac{\pi AR}{1 + \sqrt{1 + \frac{AR^2}{2}}} \quad (2.19)$$

where  $AR = b^2/S$  is the wing aspect ratio,  $b$  is the wingspan, and  $S$  is the wing surface area [26]. The drag coefficient is

$$C_D(\alpha) = C_{D_p} + \frac{(C_{L_0} + C_{L_\alpha}\alpha)^2}{\pi e AR} \quad (2.20)$$

where  $e$  is the Oswald efficiency factor, a parameter used to account for induced drag generated as a result of lift, from [27].

#### 2.2.4 Aerodynamic Flapping Forces

The aerodynamics for flapping are significantly more complex than for gliding and require a different set of equations. A quasi-steady aerodynamic model was developed and validated by Han [23] and is used in the simulation. This model was chosen because the aerodynamic forces and moments are functions of the wing shape and flight speed of the FWMAV which allow the aerodynamics to be adjustable for any FWMAV. Han also verified his models

by comparing the forces generated in simulation to those found in literature with high degrees of accuracy, presenting a compelling case for the validity of his model [23] [28]. The model breaks the wing down into a specified number of elements,  $N$ , and the aerodynamic forces and moments are computed for each blade element, this is what is known as blade element theory (BET). This ensures high accuracy, as the shape of the wing and the different centers of pressure are accurately accounted for.

The total forces and moments are comprised of the translational component, the rotational component, and the added-mass component. The translational component is due to the FWMAV moving through the air. The rotational component is due to the rotational motion of the wing around its pitching axis during flapping which affects the airflow patterns and aerodynamic forces acting on the wing. The added mass component is from the acceleration of the air which caused a redistribution of mass on the wing, affecting the forces generated from flapping. The total forces and moments are taken from literature [23] and are expressed as

$$F^W = F_{trans}^W + F_{rot}^W + F_{added}^W \quad (2.21)$$

$$M^W = M_{trans}^W + M_{rot}^W + M_{added}^W \quad (2.22)$$

To allow for the simulation to be compatible with any given wing, generalized equations for wing shapes were used [29]. Figure 2.6 illustrates a generic

wing as well as the wing parameter definitions and the blade element theory coordinate system used for the calculations. The  $x$ -axis is aligned with the wing's axis or rotation, where  $r$  is the radial distance along it. The intersection of the  $x$ -axis and  $y$ -axis ( $O'$ ) is the shoulder. The wing root, which is the proximal point on the leading edge, can be offset from the shoulder by distances  $x_r$  and  $y_r$ , where both distances are typically set to 0, and any offsets can be implemented in the equations for the chord length and leading edge. The radial distance from the wing root, along the  $r'$ -axis, is  $r'$ . The wing length  $R$  is the distance from the wing root to the most distal point on the wing projected along the  $r'$ -axis.  $c$  is the cord profile, and  $y_{LE}$  is the distance from the  $r'$ -axis to the leading edge as a function of  $r'$ .

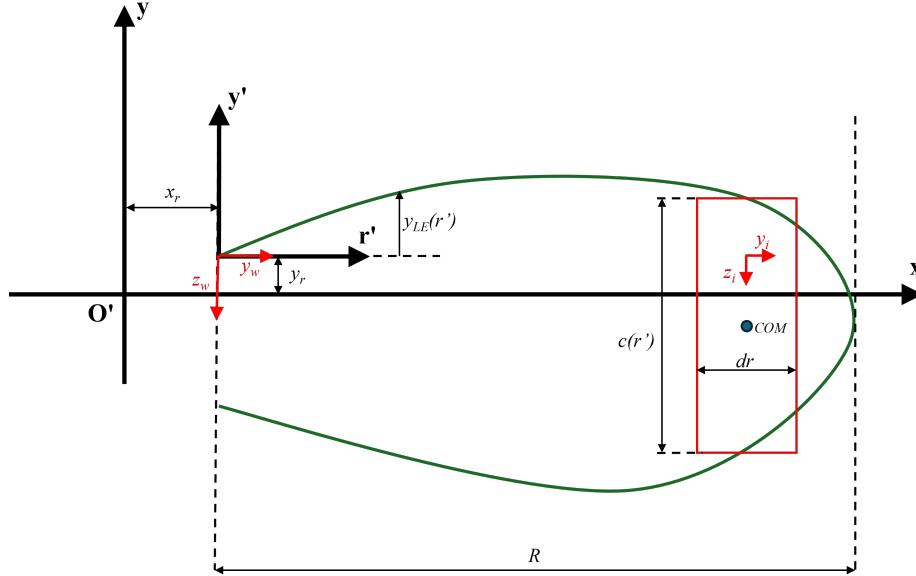


Figure 2.6: Coordinate system and dimensions for a generic wing used in blade element theory calculations. The black lines show the coordinate system used for the wing shape equations, and the red represents the coordinate system used in the blade element theory.

The radial and chordwise coordinates are made non-dimensional by divid-

ing by  $R$  and  $\bar{c}$  respectively, where  $\bar{c}$  is the mean chord length calculated as the area of the wing divided by the wing length,  $\frac{A_W}{R}$ . The non-dimensional parameters are radial distance:  $\hat{r} = \frac{r'}{R}$ , chord profile:  $\hat{c} = \frac{c}{\bar{c}}$ , leading edge profile:  $\hat{y}_{LE} = \frac{y_{LE}}{\bar{c}}$ , x-root offset:  $\hat{x}_r = \frac{x_r}{R}$ , and y-root offset:  $\hat{y}_r = \frac{y_r}{\bar{c}}$ . A wing's shape can be fully defined by  $R$ ,  $AR$ ,  $\hat{c}(\hat{r})$ , and  $\hat{y}_{LE}(\hat{r})$ , where  $AR$  is the aspect ratio defined as  $AR = \frac{R}{\bar{c}}$ , in addition to the wing root offsets  $\hat{x}_r$  and  $\hat{y}_r$ .

The calculations used in the blade element theory calculations require the additional geometrical parameters  $\hat{r}_2$ ,  $\hat{r}_M$ , and  $\hat{x}_0$ .  $\hat{r}_2$  and  $\hat{r}_M$  are calculated in equations 2.23 and 2.24 respectively [23].  $\hat{x}_0$  is the non-dimensional distance from the pitching axis to the leading edge, calculated in eq. 2.25.

$$\hat{r}_2 = \sqrt{\int_0^1 \hat{r}^2 \hat{c} \cdot d\hat{r}} \quad (2.23)$$

$$\hat{r}_M = \sqrt{\int_0^1 \hat{r}^2 \hat{c}^2 \cdot d\hat{r}} \quad (2.24)$$

$$\hat{x}_0 = \hat{y}_{LE} + \hat{y}_r \quad (2.25)$$

Knowing the wing shape and coordinate system definitions, the aerodynamic blade element theory model can be derived. To begin, the body frame coordinate system is transformed to the wing frame through a series of rotation matrices for the wing's rotation angles: the stroke plane angle,  $\beta$ , the stroke angle,  $\phi$ , the rotation angle,  $\theta$ , and the deviation angle,  $\psi$  seen in Fig-

ure 2.2. The rotation matrix used to transform the body frame to the wing frame is

$$R^{B \rightarrow W} = R_{\theta_w} R_{\psi_w} R_{\phi_w} R_{\beta} \quad (2.26)$$

$$\text{where } R_{\theta_w} = \begin{bmatrix} \cos \theta_w & 0 & -\sin \theta_w \\ 0 & 1 & 0 \\ \sin \theta_w & 0 & \cos \theta_w \end{bmatrix}, R_{\psi_w} = \begin{bmatrix} 1 & 0 & 1 \\ 0 & \cos \psi_w & -\sin \psi_w \\ 0 & \sin \psi_w & \cos \psi_w \end{bmatrix},$$

$$R_{\phi_w} = \begin{bmatrix} \cos \phi_w & \sin \phi_w & 0 \\ -\sin \phi_w & \cos \phi_w & 0 \\ 0 & 0 & 1 \end{bmatrix}, \text{ and } R_{\beta_w} = \begin{bmatrix} \cos \beta_w & 0 & \sin \beta_w \\ 0 & 1 & 0 \\ -\sin \beta_w & 0 & \cos \beta_w \end{bmatrix}.$$

The velocity of the body in the body frame is converted to the wing frame by multiplying by the rotation matrix

$$V_{body}^W = R^{B \rightarrow W} V_{body}^B \quad (2.27)$$

The angular velocity of the wing in the wing-frame is

$$\omega_{wing}^W = \begin{bmatrix} 0 \\ \dot{\theta} \\ 0 \end{bmatrix} + R_{\theta} \begin{bmatrix} \dot{\psi} \\ 0 \\ 0 \end{bmatrix} + R_{\theta} R_{\psi} \begin{bmatrix} 0 \\ 0 \\ \dot{\psi} \end{bmatrix} \quad (2.28)$$

The inflow velocity vector on the  $i$ th blade element  $V_i^W$  contains only an  $x$  and  $z$  component, representing the flow perpendicular to the wing surface and chordwise flow as seen in Figure 2.6. The inflow velocity vector is given

as

$$V_i^W = \begin{bmatrix} 1 & 0 & 0 \\ 0 & 0 & 0 \\ 0 & 0 & 1 \end{bmatrix} (V_{body}^W + \omega_{wing}^W \times r_i^W) \quad (2.29)$$

where  $r_i^W$  is the distance from the wing root to the  $i$ th blade element and consists only of a  $y$  component.

The angle of attack of the  $i$ th blade element,  $\alpha_i$  is defined as

$$\alpha_i = \tan^{-1} \frac{\sqrt{[V_i^W \times \hat{c}_i^W]^T [V_i^W \times \hat{c}_i^W]}}{V_i^W \cdot \hat{c}_i^W} \quad (2.30)$$

where  $\hat{c}_i^W$  is a unit vector pointing towards the leading edge and is equal to  $\begin{bmatrix} 0 & 0 & -1 \end{bmatrix}^T$ .

The lift and drag unit vectors,  $\hat{l}_i^W$  and  $\hat{d}_i^W$ , which dictate the direction of the aerodynamic forces are derived by Han [23] and are given as

$$\hat{l}_i^W = \frac{V_i^W \cdot i_i^W}{\sqrt{(V_i^W \cdot i_i^W)(V_i^W \cdot i_i^W)}} \begin{bmatrix} 0 & 0 & 1 \\ 0 & -1 & 0 \\ -1 & 0 & 0 \end{bmatrix} \frac{V_i^W}{\sqrt{[V_i^W]^T V_i^W}} \quad (2.31)$$

$$\hat{d}_i^W = \begin{bmatrix} -1 & 0 & 0 \\ 0 & 0 & 0 \\ 0 & 0 & -1 \end{bmatrix} \frac{V_i^W}{\sqrt{[V_i^W]^T V_i^W}} \quad (2.32)$$

where  $i_i^W$  is a unit vector in the  $x$  direction on the wing [23]. The acceleration

of the blade elements  $a_i^W$  is used for estimating the added-mass contribution at the center of each element,  $s_i^W$ . The added mass force is the inertial force experienced by an FWMAV due to the acceleration of the air particles around it during flapping motion, causing a redistribution of mass, and creating an additional inertial force acting on the wing. The acceleration of the center of the blade element is

$$a_i^W = \frac{d}{dt} V_{i@c_i^*}^W \quad (2.33)$$

$$s_i^W = \begin{bmatrix} 0 & r_i^w \cdot \hat{j}^W & c_i^* \end{bmatrix}^T \quad (2.34)$$

In the equation above,  $c_i^*$  is the distance along the  $z$ -axis from the wing root axis to the center of mass of the blade element. The velocity  $V_{i@c_i^*}^W$  follows a similar form to equation 2.29 and is

$$V_{i@c_i^*}^W = V_{body}^W + \omega_{wing}^W \times s_i^W \quad (2.35)$$

With the frames and velocities calculated, the forces and moments in Equations 2.21 and 2.22 can be calculated where

$$F_{trans}^W = \sum_{i=1}^N \{C_L \frac{1}{2} \rho [V_i^W]^T V_i^W c_i \Delta r\} \hat{l}_i^W + \sum_{i=1}^N \{C_D \frac{1}{2} \rho [V_i^W]^T V_i^W c_i \Delta r\} \hat{d}_i^W \quad (2.36)$$

$$F_{rot}^W = \sum_{i=1}^N \{C_R \rho (\omega_{wing}^W \cdot \hat{j}^W) \sqrt{[V_i^W]^T V_i^W} c_i^2 \Delta r\} \hat{i}^W \quad (2.37)$$

$$F_{added}^W = \sum_{i=1}^N \{C_A \rho (a_i^W \cdot \hat{i}^W) c_i^2 \Delta r\} \hat{i}^W \quad (2.38)$$

$$M_{trans}^W = \sum_{i=1}^N \{C_M \frac{1}{2} \rho [V_i^W]^T V_i^W c_i^2 \Delta r\} \hat{j}^W + \sum_{i=1}^N \{r_i^W \times F_{i,trans}^W\} \quad (2.39)$$

$$M_{rot}^W = \sum_{i=1}^N \{s_i^W \times F_{i,rot}^W\} \quad (2.40)$$

$$M_{added}^W = \sum_{i=1}^N \{s_i^W \times F_{i,added}^W\} \quad (2.41)$$

The forces and moments are calculated in the wing frame and must be converted to the body frame. The forces and moments are multiplied by the transpose of the rotation matrix from equation 2.26 to express the forces and moments in the body frame.

$$F^B = [R^{B \rightarrow W}]^T F^W \quad (2.42)$$

$$M^B = [R^{B \rightarrow W}]^T M^W \quad (2.43)$$

The aerodynamic coefficients for lift ( $C_L$ ), drag ( $C_D$ ), and moment ( $C_M$ ) used in equations 2.36 and 2.39 were derived and verified by Han [23] and are shown in Equation 2.45, 2.46, and 2.47. He used regression curves on collected data to generate curve-fit models. This model takes into account the leading edge vortices and the vortex potential generated during flapping and is a function of the advance ratio ( $J$ ), the angle of attack ( $\alpha$ ), the non-dimensional second moment of the wing area ( $\hat{r}_2$ ), and  $\hat{r}_M$ .  $J$ , the advance ratio, is defined as the forward flight speed,  $U_{inf}$ , divided by the mean wingtip speed which is a function of the flapping frequency  $f$  in Hz, the stroke amplitude  $\phi_{amp}$ , and

the wing length  $R$ .

$$J = \frac{U_{\text{inf}}}{2\phi_{amp}fR} \quad (2.44)$$

The coefficient for the rotational force ( $C_R$ ) shown in Equation 2.48, and used in Equation 2.37 is identical to that found in literature [30]. The added mass coefficient ( $C_A$ ) shown in Equation 2.49, and used in Equation 2.38, is a modified result from DeLaurier [23]. Han discovered that the traditional contribution of the added mass on a flapping wing is only true when the flow is fully attached to the wing, and since large advance ratios lead to more irregularly shaped wake structures leading to separated flow, the conventional aerodynamic models for added-mass effects cannot be used [31] [32]. DeLaurier overcomes this issue by adding an added mass coefficient for a flapping wing in the post-stall region [33] where one side of the wing has attached flow, and the second side has separated flow, which Han modified. The aerodynamic coefficients are given as

$$C_L(\alpha, J) = K_{P,L}(J) \sin(\alpha) \cos^2(\alpha) + K_{V,L}(J) \sin^2(\alpha) \cos(\alpha) \quad (2.45)$$

$$C_D(\alpha, J) = K_{P,D}(J) \sin^2(\alpha) \cos(\alpha) + K_{V,D}(J) \sin^3(\alpha) \quad (2.46)$$

$$C_M(\alpha, J) = K_{P,M}(J) \sin^2(\alpha) \cos(\alpha) + K_{V,M}(J) \sin^2(\alpha) \cos(\alpha) \quad (2.47)$$

$$C_R = \pi(0.75 - \hat{x}_0) \quad (2.48)$$

Table 2.1: Coefficients of the correction factors  $K_P$  and  $K_V$ 

		a	b	d
Lift	$K_{P,L}$	-2.109	-0.606	4.136
	$K_{V,L}$	2.659	-0.666	-0.344
Drag	$K_{P,D}$	-0.182	-2.414	1.370
	$K_{V,D}$	0.765	-1.497	2.078
Pitching moment	$K_{P,M}$	0.803	-0.972	-0.363
	$K_{V,M}$	-0.242	-1.354	-0.554

$$C_A = \frac{\pi}{8} \quad (2.49)$$

where  $\hat{x}_0$  is the non-dimensional distance from the pitching axis to the leading edge. The correction factors  $K_{P,L}$ ,  $K_{V,L}$ ,  $K_{P,D}$ ,  $K_{V,D}$ ,  $K_{P,M}$ , and  $K_{V,M}$  are calculated to be

$$K_{P,F \text{ or } V,F} = a(J + \hat{r}_2)^b + d \quad (2.50)$$

$$K_{P,M \text{ or } V,M} = a(J + \hat{r}_M)^b + d \quad (2.51)$$

where the subscripts  $F$  and  $M$  stand for force (lift and drag) and moment respectively. The coefficients for the correction factors  $K_{P,L}$ ,  $K_{V,L}$ ,  $K_{P,D}$ ,  $K_{V,D}$ ,  $K_{P,M}$ , and  $K_{V,M}$  are given in table 2.1. In the model, the values of  $K_V$ , the correction factor referring to the leading edge vortices, decrease as the forward flight speed increases. This demonstrates the degradation of the vorticity of the leading edge vortex and corresponding lift and drag forces during forward flight.

## Wing Kinematics

During the flapping process, the wing moves up and down and simultaneously rotates about the pitching axis of the wing, increasing and decreasing the angle of attack during the upstroke and downstroke of the wing. Simply flapping up and down without any rotation causes a periodic force profile where the average force exerted over a period is equal to zero. Figure 2.7 and Figure 2.8, show the stroke angle during one period and the forces and moments generated by the flapping motion. As seen in the figures, when there is no pitch angle during the duration of a singular flap, the net force over one period is equal to zero, as the forces produced during the symmetric upstroke and downstroke cancel each other out.

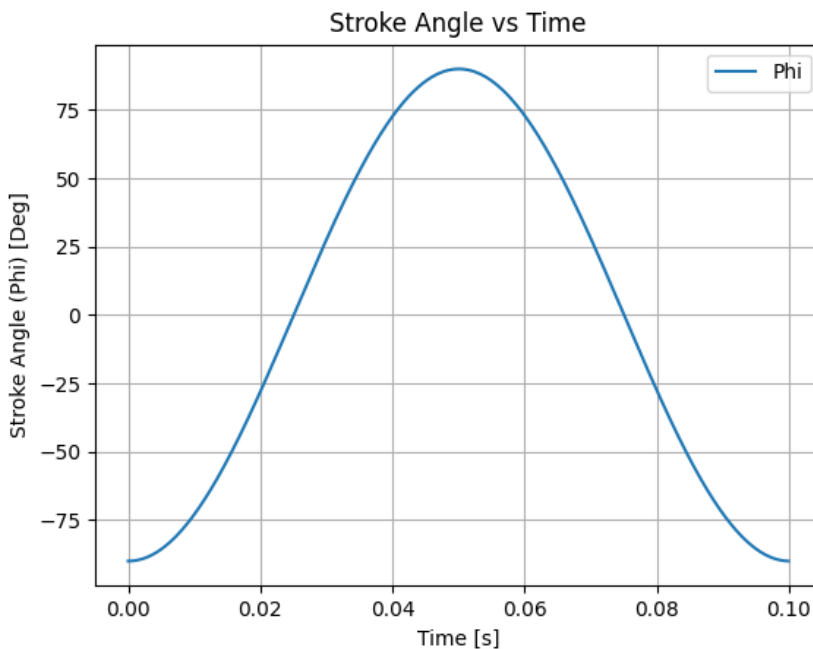


Figure 2.7: Stroke angle of rectangular wings of size 0.1m x 0.033m, flapping at 10 Hz, in a free stream velocity of 0 m/s.

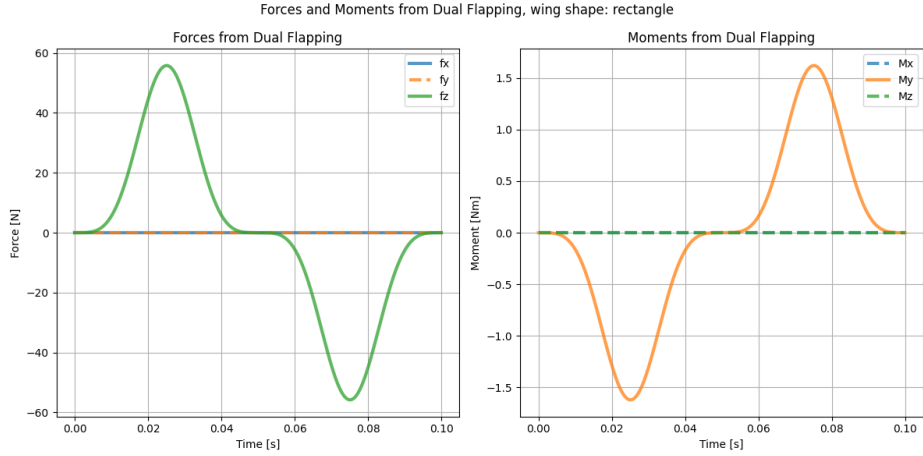


Figure 2.8: Flapping force generated by rectangular wings of size 0.1m x 0.033m, flapping at 10 Hz, in a free stream velocity of 0 m/s.

To accurately produce the thrust and lift forces that enable forward flight, an accurate wing rotational kinematics had to be devised that represents the motion of a biological flyer's wings in forward flight. Because CUBIRD is looking at biology for inspiration, the wing kinematics will likely follow similar patterns to those found in nature. In the future, the wing kinematics can be updated to reflect the true kinematics of the transmission design. For simplicity, the deviation angle is assumed to be a constant value, since the deviation angle in biological flyers typically has little variation [28]. A formulation for the stroke angle and rotation angle for the wing is written in equations 2.52 and 2.53, where  $\phi_0$  and  $\theta_0$  are the average stroke and rotation angle,  $\phi_{amp}$  and  $\theta_{amp}$  are the stroke and rotation angle amplitudes,  $C_\alpha$  is a constant that adjusts the speed at which the pitch changes and is set to 2.6 to best match the data from [28], and  $f$  is the flapping frequency in Hz [34].

$$\phi_{wing}(t) = \phi_0 - \phi_{amp} \sin(2\pi ft + \pi/2) \quad (2.52)$$

$$\theta_{wing}(t) = \theta_0 - \frac{\theta_{amp}}{\tanh(C_\alpha)} \tanh(C_\alpha \sin(2\pi ft + \pi)) \quad (2.53)$$

Figure 2.9 shows the stroke, rotation, and deviation angles generated by equations 2.52 and 2.53 compared to the wing angle profile of a biological flyer. The underlying graph is the flapping profile of a Hawkmoth flying at 5 m/s, taken from Willmott and Ellington [28]. In 2.9a The blue curve shows the approximation of the stroke angle over one period as calculated in equation 2.52 and the orange line shows the approximation for the deviation angle. In 2.9b the blue line shows an adjusted approximation for the rotation angle.

An interesting observation seen by Willmott and Ellington was that biological flyers change their stroke plane angle, maximum and minimum stroke angles, and maximum and minimum rotation angles depending on the speed at which they are flying [28]. While hovering, Willmott and Ellington observed stroke plane angles of 125° compared to 105 ° when flying at 5 m/s. They also noticed that at low flight speeds, the rotation angle along the  $r'$ -axis of the wing, would increase in magnitude as you progressed radially along the  $r'$ -axis of the wing, but at higher speeds, 5 m/s or above, there was a near-constant rotation angle through the entire wing. Representing these kinematic changes

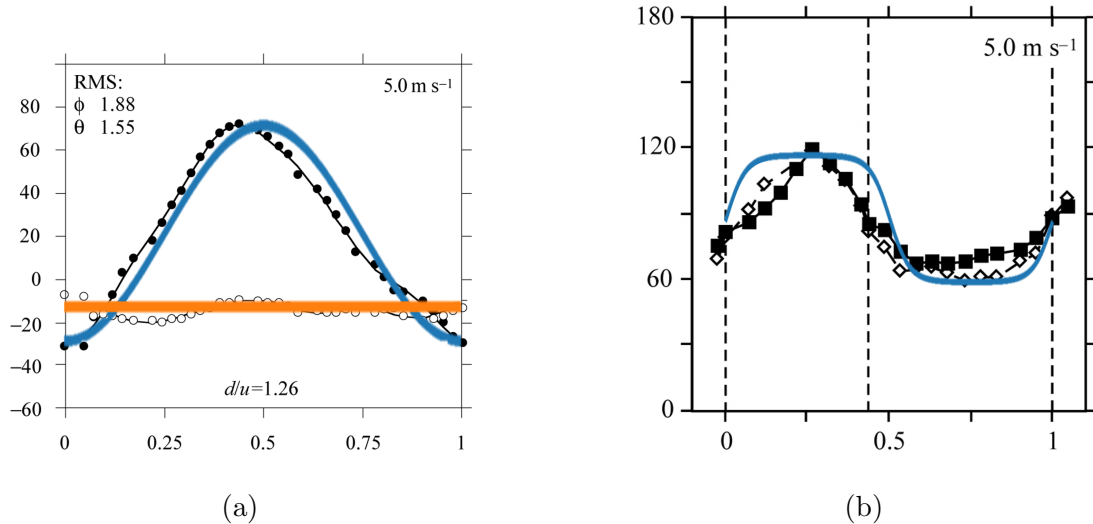


Figure 2.9: Comparison of wing profile angles of the Hawkmoth with the simplified equations. Figure 2.9a shows the stroke and deviation angles. The Hawkmoth's average stroke angle was  $21.5^\circ$ , minimum stroke angle was  $-30.4^\circ$ , stroke amplitude was  $103.9^\circ$ , and the deviation angle was  $-13.7^\circ$ . Figure 2.9b shows the pitch angle where the average pitch angle was  $90^\circ$ , minimum rotation angle was  $60^\circ$ , and rotation amplitude was  $60^\circ$  [28].

can make modeling a biological flyer more complex as equations would have to be derived correlating the flight speed and position along the wing with the stroke plane angle, stroke angle, and rotation angle. In the current simulation, the wing profile equations are assumed to be constant, both radially along the wing and for different flight speeds, but more complex equations that take into account the velocity and radial position  $r$  along the  $r'$  axis of the wing can be used at a later date.

### 2.2.5 Numerical Solver

Now that the equations of motion are known and the forces are fully defined, a numerical solver can be used to integrate every time step to determine the next state. A simple solver would follow the form  $\mathbf{x}_{i+1} = \mathbf{x}_i + d\mathbf{x}_i \cdot dt$ ,

where  $\mathbf{x}$  is the state and  $d\mathbf{x}$  is the derivative of the state. In 2d, the state is  $[x, y, \theta, \dot{x}, \dot{y}, \dot{\theta}]$ , and  $d\mathbf{x}$  is  $[\dot{x}, \dot{y}, \dot{\theta}, \ddot{x}, \ddot{y}, \ddot{\theta}]$  where  $\dot{x}, \dot{y}, \dot{\theta}$  are the same as the state's and  $\ddot{x}, \ddot{y}, \ddot{\theta}$  are taken from the equations of motion, in this case, taken from equations 2.59, 2.60, and 2.61. To increase the accuracy of the solver, a Runge-Kutta solver was implemented in the simulation. The Runge-Kutta solver uses a weighted average of the derivatives to provide a more accurate prediction of the next time step. The solver's inputs are the current state, the external forces (used to calculate the accelerations), and the time step. The equations below show how the solver works. In these equations, the function  $dxdt()$  is a function that takes in the current state and additional forces and calculates the derivative of the state.

$$K1 = \Delta t * dxdt(\text{state}, \text{Forces}) \quad (2.54)$$

$$K2 = \Delta t * dxdt(\text{state} + 1/2 * K1, \text{Forces}) \quad (2.55)$$

$$K3 = \Delta t * dxdt(\text{state} + 1/2 * K2, \text{Forces}) \quad (2.56)$$

$$K4 = \Delta t * dxdt(\text{state} + 1 * K3, \text{Forces}) \quad (2.57)$$

$$\text{state+} = (K1/6 + K2/3 + K3/3 + K4/6) \quad (2.58)$$

## 2.3 Simulation Setup

Before jumping into a three-dimensional simulation with six degrees of freedom, a two-dimensional simulation was developed. As mentioned earlier, in two dimensions, the FWMAV has three degrees of freedom: movement along the x-axis ( $x$ ), movement along the y-axis ( $y$ ), and rotation about the z-axis ( $\theta$ ) and will have gravity, the wing force, and the tail force acting upon it. Even though the FWMAV will be flying in three dimensions, a two-dimensional simulation can be used to verify the aerodynamic models and gain insights into the behavior of the FWMAV.

### 2.3.1 Derivative Function for the Solver

The FWMAV in the simulation has two symmetric wings and a tail that can be angled to a specified angle  $\theta_{tail}$ . The gravitational force is always acting in the global  $-y$  direction at the center of mass, and the tail and wing forces ( $F_{tail}$  and  $F_{wing}$ ) are calculated by their respective models in the body-frame, as mentioned in the previous section, at distances  $r_{tail}$  and  $r_{wing}$  from the center of mass. Newton's second law only holds true for non-moving frames, the tail and flapping forces that are calculated in the body frame respectively, must be converted to the global frame using equation 2.1. The global and body frames and the forces shown in the body frame can be seen in Figure 2.10. The complete set of equations used to calculate the

second derivatives used in the numerical solver, while satisfying Newton's second law, are

$$\ddot{x} = \frac{(F_{wing-y} + F_{tail-y})(-\sin(\theta)) + (F_{wing-x} + F_{tail-x})\cos(\theta)}{m_{body}} \quad (2.59)$$

$$\ddot{y} = \frac{-m_{body}g + (F_{wing-y} + F_{tail-y})\cos(\theta) + (F_{wing-x} + F_{tail-x})\sin(\theta)}{m_{body}} \quad (2.60)$$

$$\ddot{\theta} = \frac{r_{wing}F_{wing-y} + r_{tail}F_{tail-y} + M_{wing-z}}{J_{body}} \quad (2.61)$$

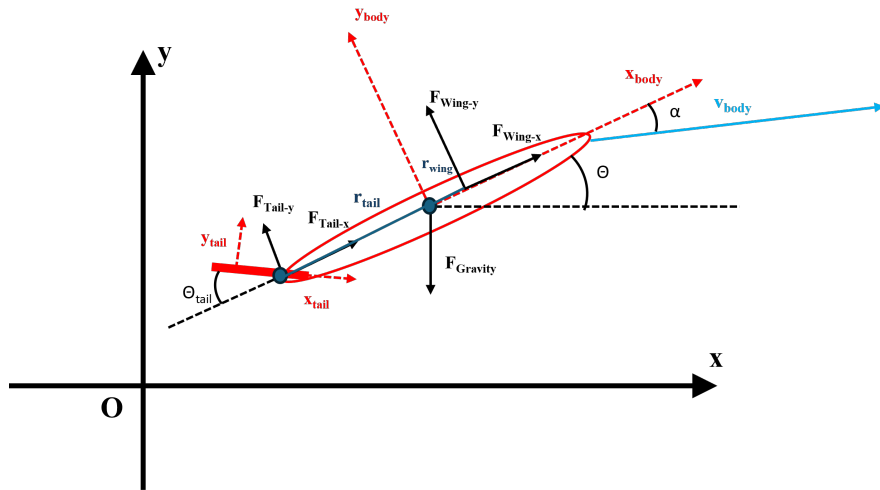


Figure 2.10: 2D Global and body frames.

## **Effects of the $x$ -Component of the Tail Force**

The moment calculation in equations of motion only accounts for the  $y$  component of the tail force, neglecting the contribution from the tail force in the  $x$  direction. Figure 2.11 shows the flight path, pitch, and angles of attack of an FWMAV with and without the tail's  $x$  force being incorporated into the moment calculation. In this example, the tail's center of pressure position was located 0.1 meters from the center of mass in the  $-x$  direction and 0.02 m in the  $y$  direction. As seen in the figures the effect of the  $x$  force is negligible, resulting in minuscule changes in both the trajectory and pitch. Because of this, in future simulations, only the  $y$  component of the tail force is used when calculating the moments. This allows for the tail's position to be measured in one direction, along the body's  $x$ -axis, making it easier for future users to input their robot parameters.

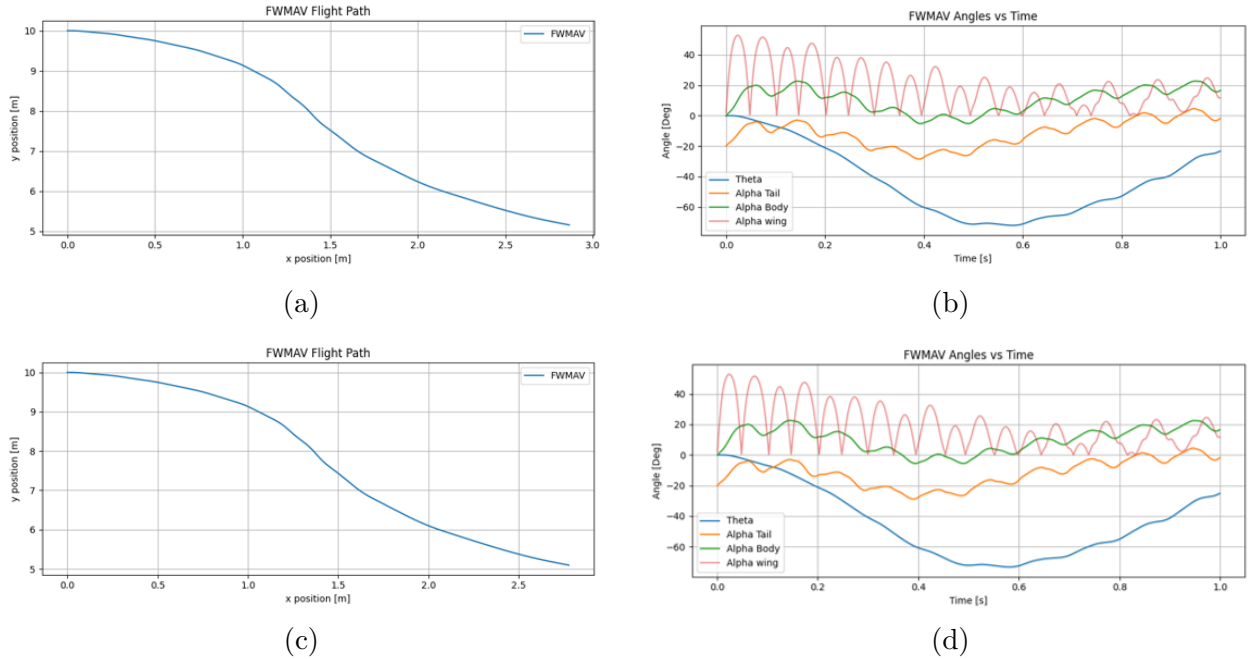


Figure 2.11: Simulation data showing the comparison of the flight path, pitch, and angle of attack of an FWMAV with the inclusion of the moment caused by the tail force in the  $x$  direction vs an FWMAV without the moment. Figure 2.11a shows the flight path of the FWMAV with the addition of the moment caused by the tail's  $x$  force. Figure 2.11b shows the pitch and angles of attack of the FWMAV with the addition of the moment caused by the tail's  $x$  force. Figure 2.11c shows the flight path of the FWMAV without the addition of the moment caused by the tail's  $x$  force. Figure 2.11d shows the pitch and angles of attack of the FWMAV without the addition of the moment caused by the tail's  $x$  force.

# Simulation Results

## 3.1 Wing Parameter Study

To gain a better understanding of the models in the simulation, various parameters, such as the wing shape, the wing kinematics, and the flapping frequency were adjusted and compared against a baseline test case. The reasoning behind this is to visualize the effects that each parameter has on the flight of the FWMAV and also to confirm that the simulation is adaptable to the various input parameters. The physical parameters of the FWMAV are found in Table 3.1. The parameters were chosen with the overall scale of the CUBIRD project in mind, with the mass being 30 grams, and the flapping frequency being 10 Hz. The additional parameters were chosen based on intuition and trial and error, where parameters were adjusted until the FWMAV behaved as expected. For instance, changes were made to the  $r_{wing}$  value because some values would lead to unstable pitch angles resulting in the FWMAV spinning continuously. The only initial condition of the FWMAV was the  $x$  velocity set to 2 m/s. The baseline wing kinematics are shown in Figure 3.2 and were selected because the kinematics can easily be altered with an increase or decrease in amplitude. Here the stroke angle ranges from -45° to 45° with an average stroke angle of 0°, and the rotation angle ranges

Table 3.1: Test Parameters

$m_{body}$	30.0 g
$L_{body}$	0.254 m
$r_{wing}$	0.0127 m
$r_{tail}$	-0.1 m
$\theta_{tail}$	20°
$S_{tail}$	0.01354 m <sup>2</sup>
$L_{tail}$	0.1778 m
$L_{wing}$	0.152 m
$AR_{wing}$	2.25
$f$	10 Hz
$\beta$	90°
$\phi_0$	0°
$\phi_{amp}$	45°
$\theta_0$	-5°
$\theta_{amp}$	15°
<i>Wing Shape</i>	Rectangle seen in Figure 3.1

from -20° to 10° with an average stroke angle of -5°. The simulation results from this test case can be seen in Figure 3.3.

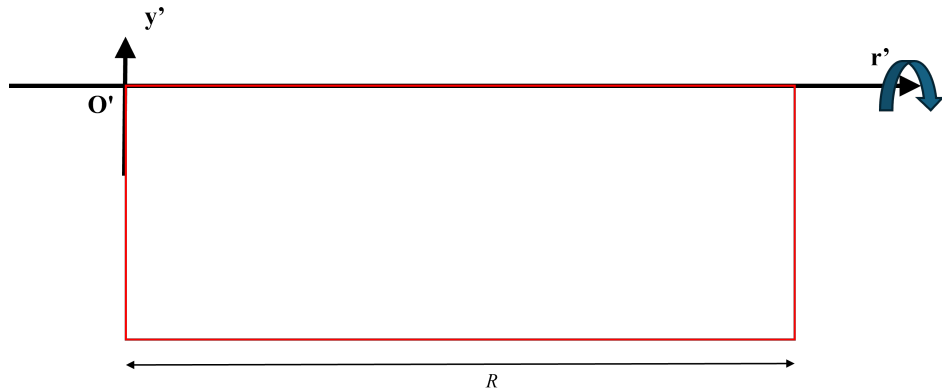


Figure 3.1: Rectangular wing used in the initial flight simulations.

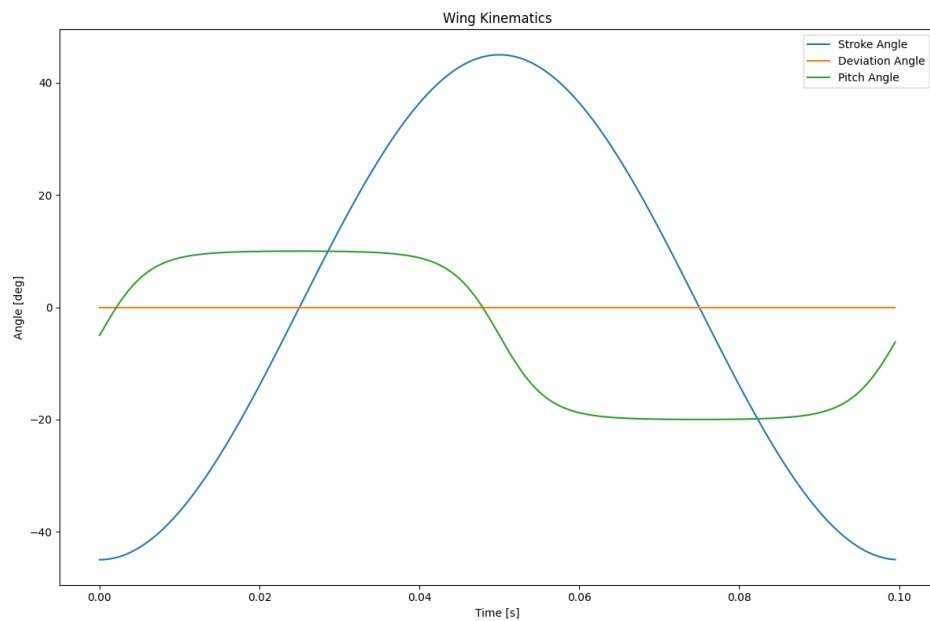


Figure 3.2: Baseline wing kinematics for 1 period used to explore the effects of variations in the stroke angle amplitude and rotation angle amplitude. The stroke angle oscillates around  $0^\circ$ , with a magnitude of  $90^\circ$  and the rotation angle oscillates around  $-5^\circ$  with an amplitude of  $30^\circ$ .

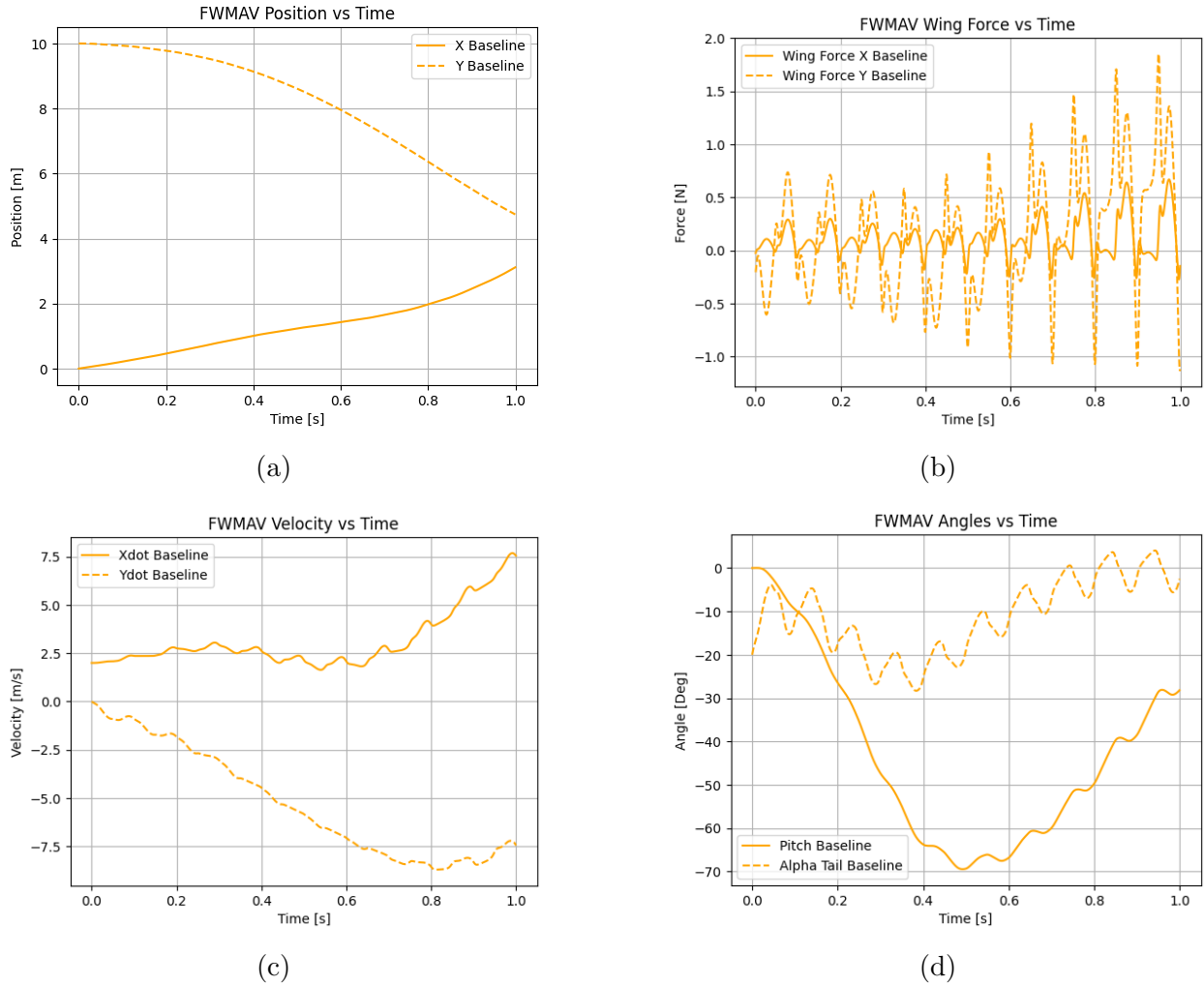


Figure 3.3: Baseline simulation data, with conventions from Figure 2.4, used to compare with the adjusted kinematics and adjusted wing shapes. Figure 3.3a shows the FWMAV's position in the global frame vs time. Figure 3.3b shows the FWMAV's flapping forces in the body frame vs time. Figure 3.3c shows the FWMAV's velocity in the global frame vs time. Figure 3.3d shows the FWMAV's pitch angle and the tail's angle of attack vs time.

### 3.1.1 Effects of Wing Shape

In this study, the effect of the wing shape was examined. Two additional wings were simulated, a triangle wing and a trapezoid wing both with the same area as the rectangular baseline. The wings overlaid onto each other can be seen in Figure 3.4.

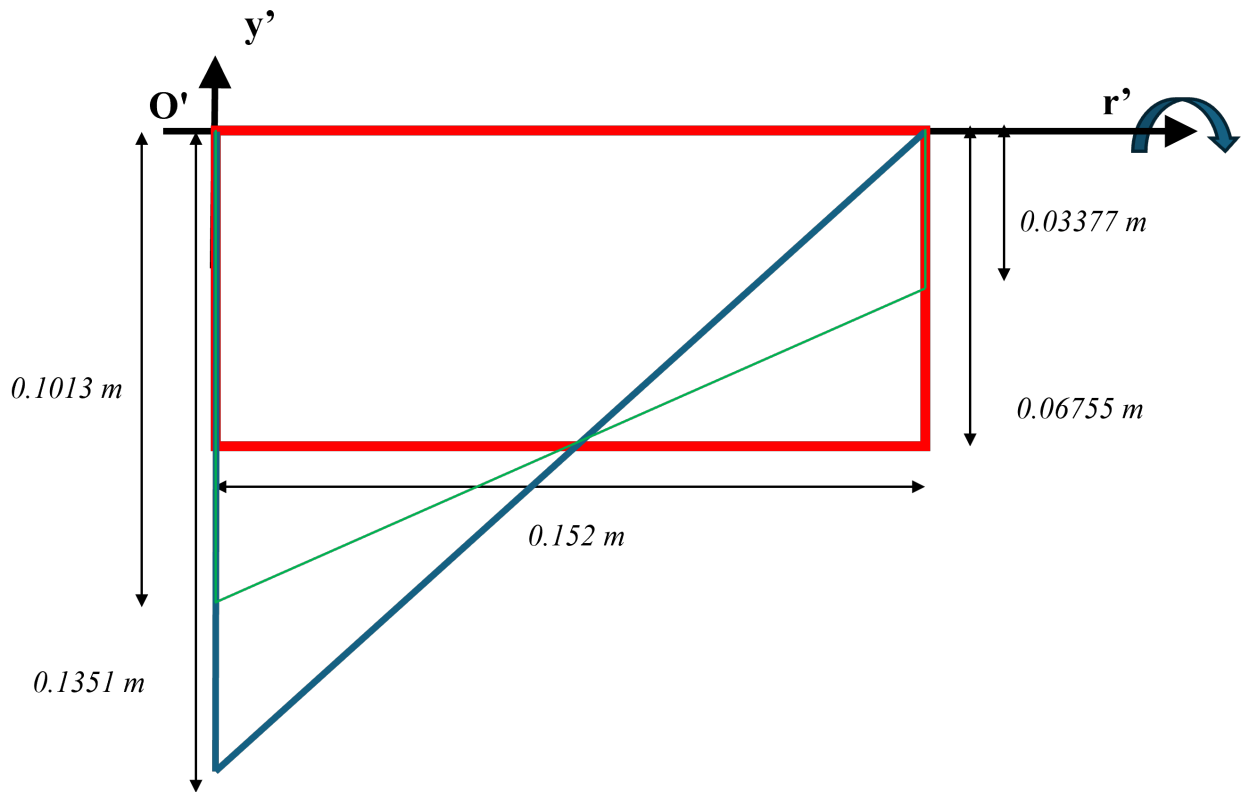


Figure 3.4: The different wing shapes used overlaid onto each other. Each wing has the same area, aspect ratio, and length.

Figure 3.5 shows the simulation data from the baseline FWMAV and the comparison to the same FWMAV but with triangular and trapezoidal wings. The initial forces, seen in Figure 3.5b, with an expanded view seen in Figure A.1, generated by the flapping triangular wings were lower than the baseline

case. The baseline rectangular wing has more surface area towards the outer edge of the wing, which has a larger contribution to the generated force because the velocity of the wing increases as the distance along the  $r'$ -axis increases. The initial forces generated by the flapping trapezoidal wings were lower than the baseline case but higher than the triangular wing. This is expected since the trapezoidal wing has more surface area at the end of the wing compared to the triangular wing, but less surface area compared to the rectangular wing.

While it is easy to see and explain the differences in the initial forces caused by the different wing shapes, as the FWMAV begins to move through the air and change its pitch and velocities, seen in Figures 3.5c and 3.5d, the long-term effects that the wing shape has on the FWMAV become harder to predict. Although the rectangular wing exhibited the highest forces, the FWMAV traveled the least distance along the  $x$ -axis and dropped the most in height, as seen in Figure 3.5a. The triangular wing generated the smallest initial forces but traveled along the  $x$ -axis further than the rectangular baseline and ended at a higher height. Following this trend, one would expect the trapezoidal wing to fall somewhere in between the rectangular wing and the triangular wing because its initial forces fell between them. However, the FWMAV with trapezoidal wings traveled the furthest along the  $x$ -axis and ended between the rectangular and triangular wing FWMAVs in height. These unexpected results highlight the sensitivity of an FWMAV to its var-

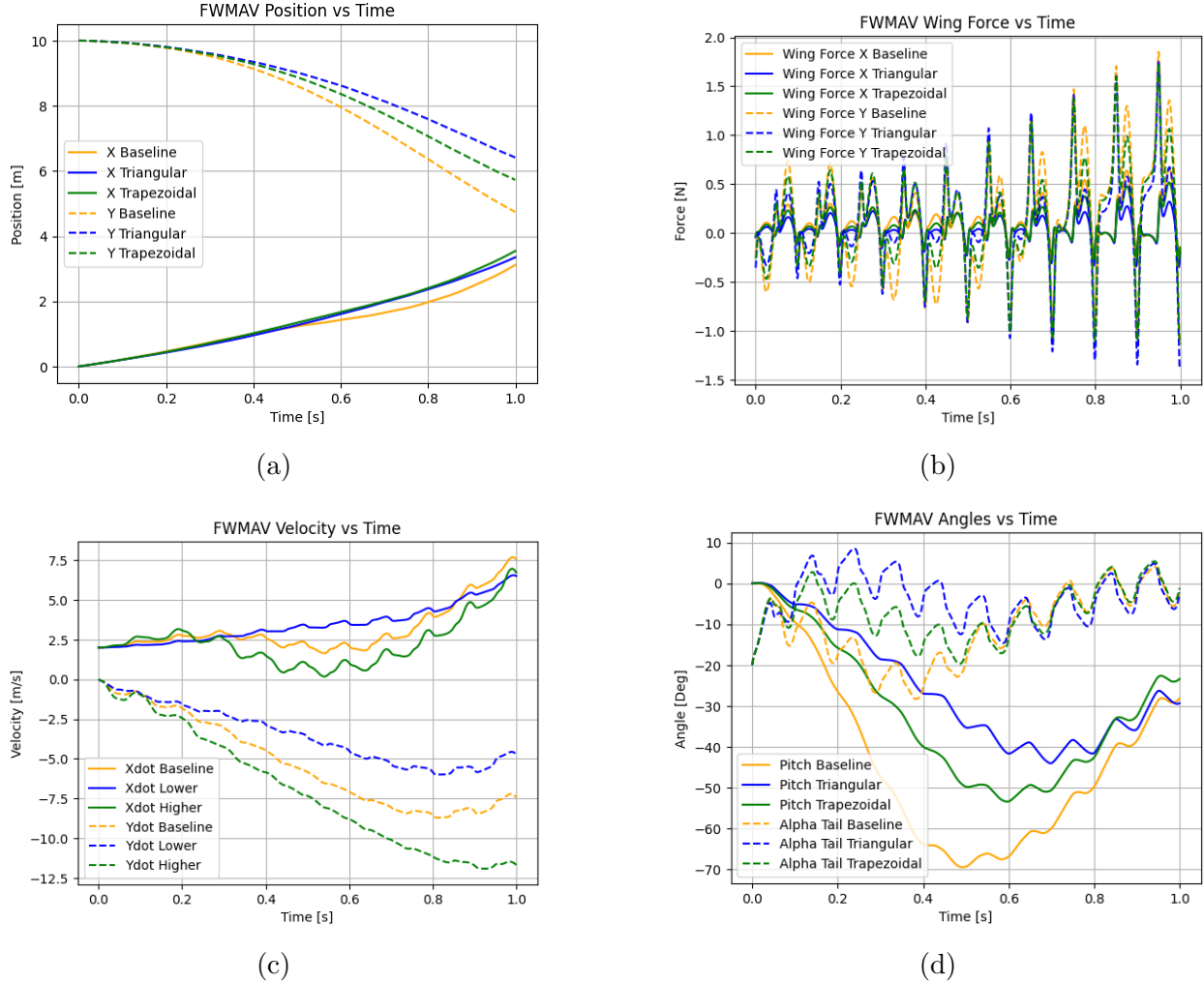


Figure 3.5: Simulation data, with conventions from Figure 2.10, from FWMAVs with rectangular (baseline), triangular, and trapezoidal wings seen in Figure 3.4. Figure 3.5a shows the FWMAV's position in the global frame vs time. Figure 3.5b shows the FWMAV's flapping forces in the body frame vs time, with an expanded view shown in Figure A.1. Figure 3.5c shows the FWMAV's velocity in the global frame vs time. Figure 3.5d shows the FWMAV's pitch angle and the tail's angle of attack vs time.

ious design components and its unpredictable behavior further necessitating an adaptable simulation environment that can be used as a design tool.

### 3.1.2 Effects of Wing Kinematics

In this study the kinematics of the wings were analyzed in two ways, changes to the stroke amplitude and changes to the rotation amplitude. Figure 3.6 shows the simulation data when the stroke angle ranges from  $-30^\circ$  to  $30^\circ$  a decrease in the amplitude of the baseline from  $90^\circ$  to  $60^\circ$  and a case where the stroke angle ranges from  $-60^\circ$  to  $60^\circ$  an increase in the amplitude to  $120^\circ$ . In this test, the FWMAV with the smaller stroke amplitude reaches a lower velocity than the baseline, shown in Figure 3.6c, because the wings are moving at a slower speed, covering a smaller distance in the same time frame as the baseline, thereby reducing the net forces exerted onto the FWMAV. The magnitude of the  $y$  velocity also is reduced due to the wings acting more like the wings of a glider because of its reduced stroke range. As the stroke amplitude gets closer to  $0^\circ$ , the wings behave more like aerodynamic surfaces such as airfoils and plates. At increased amplitudes, the flapping forces are increased because the wings are moving faster which can be seen in Figure 3.6b with an expanded view in Figure A.2. However, Figures 3.6a and 3.6d show that the increased forces lead to a larger pitch angle, causing the FWMAV to pitch downwards, increasing the distance it travels downwards but decreasing the distance it travels along the  $x$ -axis. It is noteworthy that

as the simulation continues, the  $x$  velocity of the FWMAV with the larger stroke amplitude increases at a higher rate than the FWMAV with a smaller stroke amplitude.

Figure 3.7 shows the simulation data when the rotation angle ranges from  $-25^\circ$  to  $15^\circ$  an increase in the amplitude of the baseline from  $15^\circ$  to  $20^\circ$  and a case where the rotation angle ranges from  $-15^\circ$  to  $5^\circ$  a decrease in the amplitude to  $20^\circ$ . Figure 3.7d shows that the larger amplitude in the rotation angle ultimately leads to a larger final downward pitch compared to the baseline level. In this case, the larger amplitudes in the rotation angle led to reduced angles of attack at the center of pressure of the wing. Interestingly, the FWMAV with the lowest rotation amplitude experienced the lowest minimum pitch angle but ended the simulation at the highest pitch angle. The opposite of this is seen with the FWMAV with the largest rotation amplitude, it has the highest minimum pitch but ends the simulation at the lowest pitch angle. The effects that the changes to the rotation angle amplitude have on the FWMAV are considerably less than that from the changes in stroke angle amplitude, shown by the close proximity of the different FWMAV's positional data to each other in Figure 3.7a. This is expected because the changes in amplitude for the rotation angle were less than the changes to the stroke angle and also because the majority of the flapping force is caused by the stroke motion of the wing.

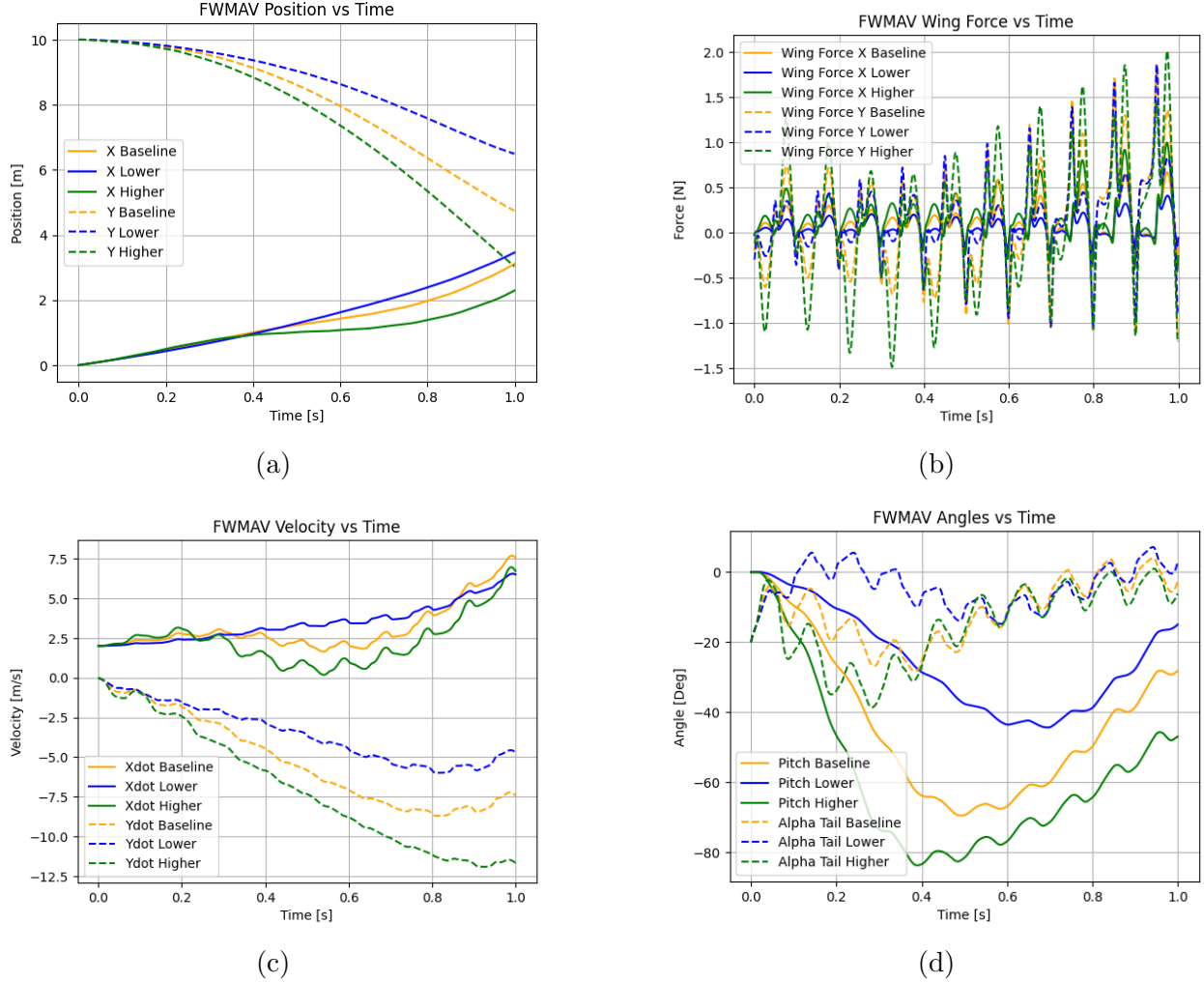


Figure 3.6: Simulation data when the wing stroke amplitude was  $60^\circ$  (lower) and  $120^\circ$  (higher) instead of the baseline  $90^\circ$  and all other parameters were held constant. Figure 3.6a shows the FWMAV's position in the global frame vs time. Figure 3.6b shows the FWMAV's flapping forces in the body frame vs time, with an expanded view shown in Figure A.2. Figure 3.6c shows the FWMAV's velocity in the global frame vs time. Figure 3.6d shows the FWMAV's pitch angle and the tail's angle of attack vs time. Here, the FWMAV with the larger stroke amplitude experienced higher initial forces, but this caused the FWMAV to pitch downwards, ultimately leading to the majority of the movement happening along the  $y$  axis. When the stroke angle is smaller, there are smaller forces and moments generated from flapping, leading to less pitch deviation and a trajectory that appears similar to gliding.

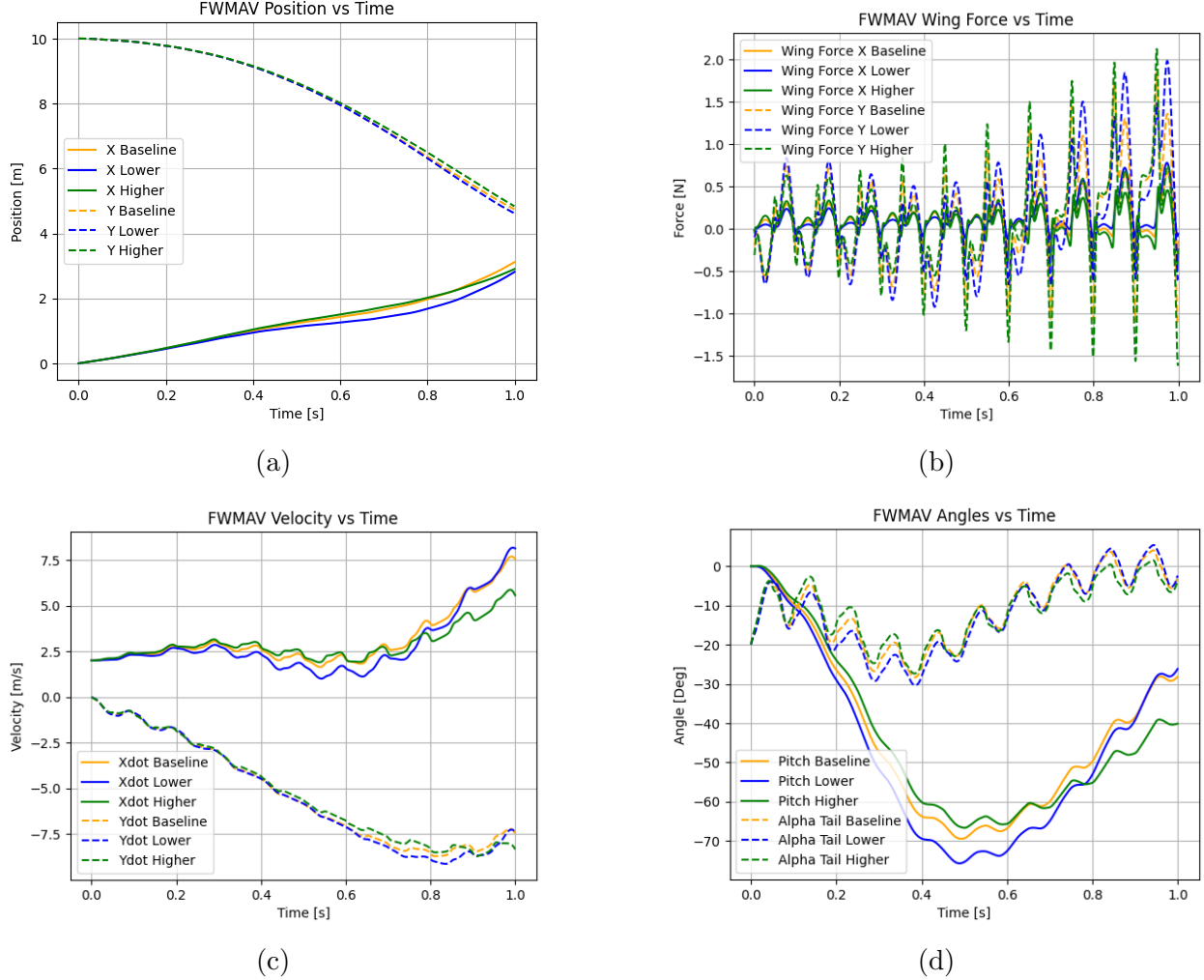
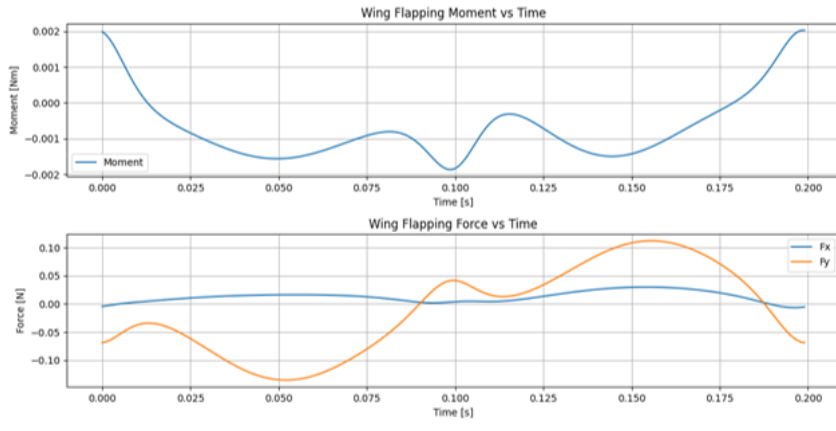


Figure 3.7: Simulation data when the wing rotation amplitude was  $40^\circ$  (higher) and  $20^\circ$  (lower) instead of the baseline  $30^\circ$  and all other parameters were held constant. Figure 3.7a shows the FWMAV's position in the global frame vs time. Figure 3.7b shows the FWMAV's flapping forces in the body frame vs time, with an expanded view shown in Figure A.3. Figure 3.7c shows the FWMAV's velocity in the global frame vs time. Figure 3.7d shows the FWMAV's pitch angle and the tail's angle of attack vs time. The effects from the changes in the rotation angle were less impactful than changes in the stroke angle seen in Figure 3.6. The velocities, positions, rotations, and rotation rates all followed similar trends and were close to each other throughout the simulation.

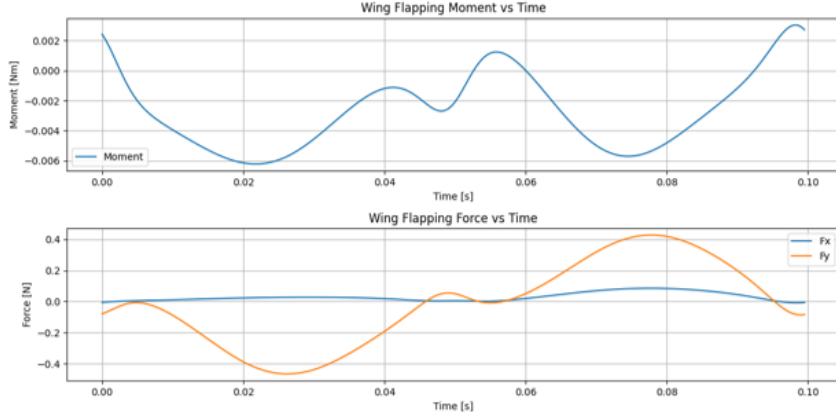
### 3.1.3 Effects of Flapping Frequency

By changing the flapping frequency the flapping wings generate different forces. The effects that different flapping frequencies have on the flapping force can be seen in Figures 3.8a, 3.8b, and 3.8c. These figures show the flapping force for one period and show that with the same wing shape and wing kinematics, flapping at higher frequencies leads to larger magnitude forces exerted by the wings, which ultimately leads to different behavior in the FWMAV. This behavior can be seen in Figure 3.9 which shows the flight data over a 1-second flight simulation. While the reduced flapping frequency follows a similar trend to the baseline, the FWMAV with increased flapping frequency behaves completely differently. The large forces generated lead to a large moment caused by the offset of the wing's shoulder from the center of mass, causing the FWMAV to rotate, performing a loop. The reduced frequency behaves similarly to the baseline, but towards the end of the simulation, Figure 3.9c shows that the baseline  $y$  velocity begins to climb, and will eventually become higher than the FWMAV with the reduced flapping frequency. Similar to the effects of the reduced stroke angle amplitude, the reduced flapping frequency causes the FWMAV to have a more stable velocity with smaller oscillations being seen due to the decreased flapping forces.

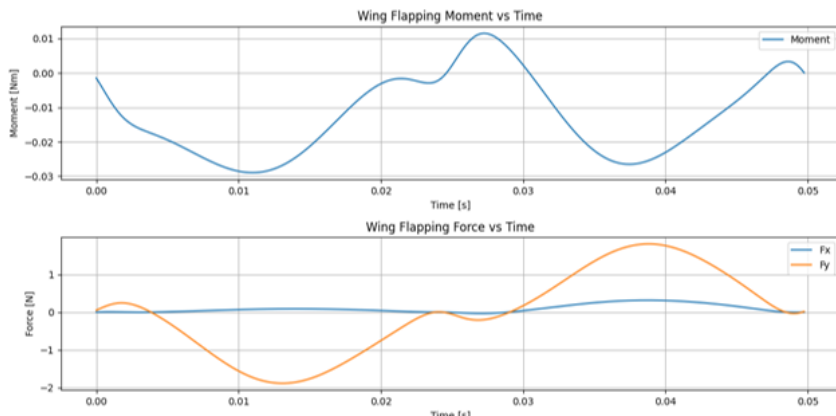
In all the test cases simulated, the magnitude of the vertical component of the flapping force was always larger than the magnitude of the horizon-



(a)



(b)



(c)

Figure 3.8: Forces and moments from a 0.152 meter long rectangular wing in a wind speed of 2 m/s flapping at different frequencies for 1 period. Figure 3.8a shows the wing flapping at 5 Hz, Figure 3.8b shows the wing flapping at 10 Hz, and Figure 3.8c shows the wing flapping at 20 Hz.

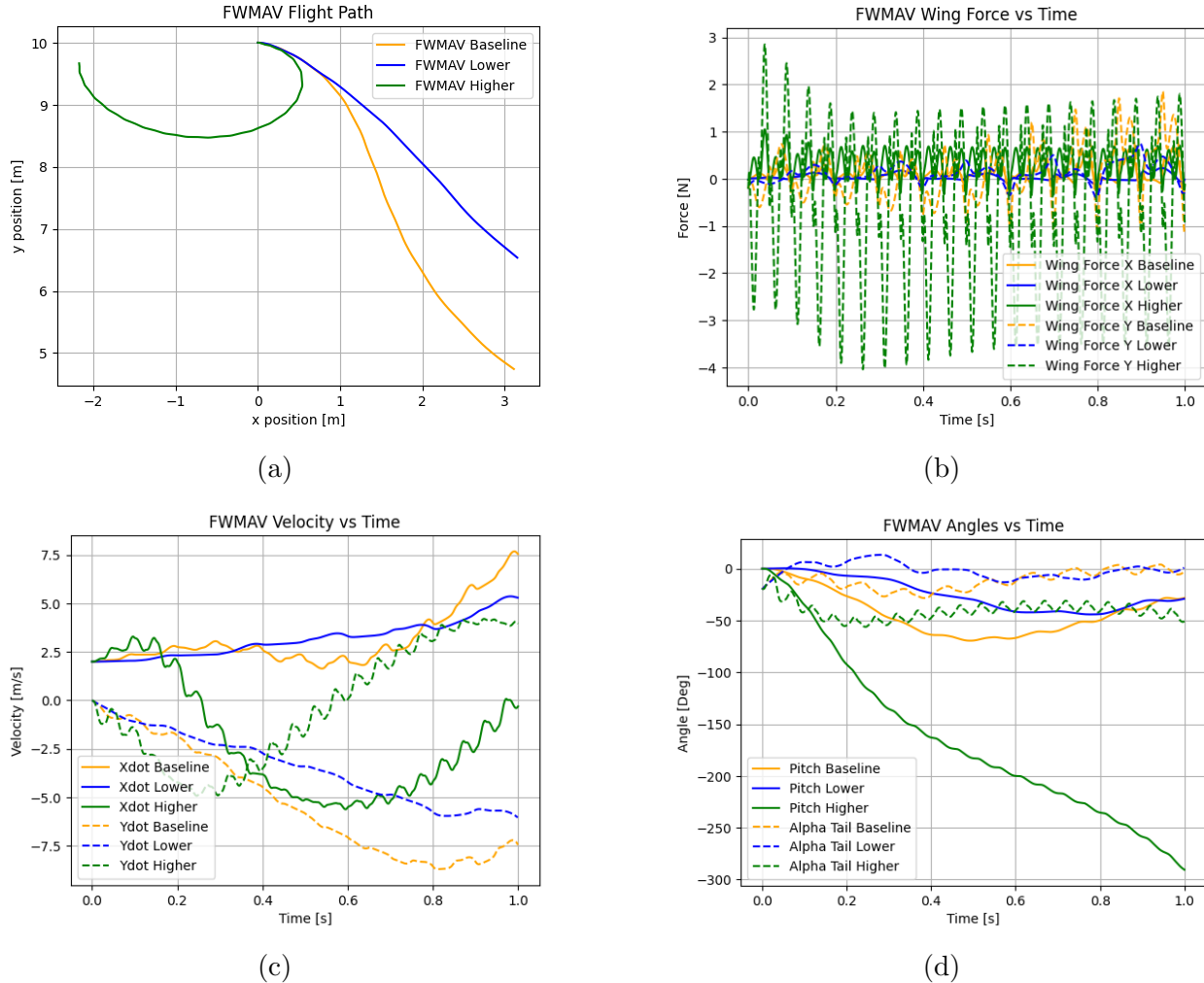


Figure 3.9: Simulation data when the flapping frequency was 20 Hz (higher) and 5 Hz (lower) instead of the baseline 10 Hz. Figure 3.9a shows the FWMAV's flight path. Figure 3.9b shows the FWMAV's flapping forces in the body frame vs time, with an expanded view shown in Figure A.4. Figure 3.9c shows the FWMAV's velocity in the global frame vs time. Figure 3.9d shows the FWMAV's pitch angle and the tail's angle of attack vs time. Flapping at too high of a frequency leads to unexpected behavior, with the FWMAV performing a loop. Flapping at a lower frequency leads to reduced forces and a reduced velocity.

tal flapping force, agreeing with the expectation that the majority of the forces generated would be in the direction of the stroke motion. Increasing the rotation angle's magnitude led to larger forces in the horizontal direction compared to the baseline, due to the changes in the angle of attack and additional rotation forces that occur, and decreases in the stroke angle's magnitude led to decreases in both the horizontal and vertical flapping forces due to the decreasing speed of the wing. Increasing the flapping frequency always led to higher flapping forces which is expected due to the faster movement of the wings, and affected these forces to a higher degree than adjustments to the stroke amplitude. The initial effects of the wing's shape follow the logic that wings with higher surface area concentrations near the wing tip will generate larger forces than those with higher surface areas near the wing root because of the increasing velocity along the radial axis of the wing. The long-term effects that the wing shapes had on the flight of the FWMAV in the simulation are more difficult to predict because of the cascading effect that the initial forces have. The initial forces affect the next state of the FWMAV, and that state will affect the subsequent forces, starting an unpredictable feedback loop. These parameter studies demonstrate not only the adaptability of the simulation to various wing kinematics and wing shapes but also show the impact that the design parameters have on the functionality and behavior of the FWMAV. The changes in the wing kinematics and wing shape and their respective effects on the flapping force agree with intuition,

with the stroke amplitude and the flapping frequency having the largest impact on the flight, providing an initial sense of validity to the core principles of the flapping model.

Understanding and visualizing the effects that the wing kinematics have on the forces and trajectory of the FWMAV is instrumental in the design process of an FWMAV. Seeing the effects of changes to various parameters of the wing kinematics and the robot's physical design without having to develop a physical FWMAV will speed up and simplify the design process. Understanding the effects that the wing kinematics have on the flight of the FWMAV can prove beneficial by being used as control inputs in the future when designing a controller for level flight.

## 3.2 Effects of Tail Location

In addition to examining the effects of changes to the wing parameters, the effect of the tail location was analyzed. Two cases were considered, one where the tail's center of pressure was moved further from the center of mass of the FWMAV and one where the tail's center of pressure was moved closer to the center of mass. When the tail is further from the center of mass, it is expected to stabilize the FWMAV with greater effect due to the increased moment arm and the increased forces from the increased angular velocity contribution, reducing the oscillations in the pitch of the FWMAV. The effects of increasing the tail distance can be seen in Figure 3.10. In comparison with

the baseline simulation, the distance from the center of mass to the tail's center of pressure,  $r_{tail}$ , was changed from -0.1 meters to -0.125 meters, an increase of 25%. This increase in distance led to the angle of attack of the tail returning to oscillate around 0° 13% faster, reduced the minimum pitch angle from approximately -70° to -60°, and reduced the angular velocity of the FWMAV as seen in Figure 3.10d.

Conversely, when  $r_{tail}$  was changed from -0.1 meters to -0.075 meters, a decrease of 25%, one would expect the stability of the FWMAV to decrease and to see larger oscillations in the pitch. The simulation data shown in Figure 3.10 supports this hypothesis. Here, the minimum pitch angle is approximately -85° compared to the -70° pitch angle in the baseline case, and the angle of attack of the tail first reaches 0° 13% slower than the baseline as seen in Figure 3.10d. In addition, the distance traveled by the FWMAV in the horizontal direction is considerably shorter than the baseline case, a reduction from 3.1 meters to 1.7 meters, shown in Figure 3.10b.

Overall the effects that the location of the tail has on the stability of the FWMAV in the simulation agree with intuition. Increasing the distance from the center of mass leads to increased stability by reducing the pitching motion, and decreasing the distance leads to increased pitch angles and longer settling times. The tail plays a pivotal role in passively stabilizing the FWMAV, so the location (and size) of the tail must be carefully considered in the design process.

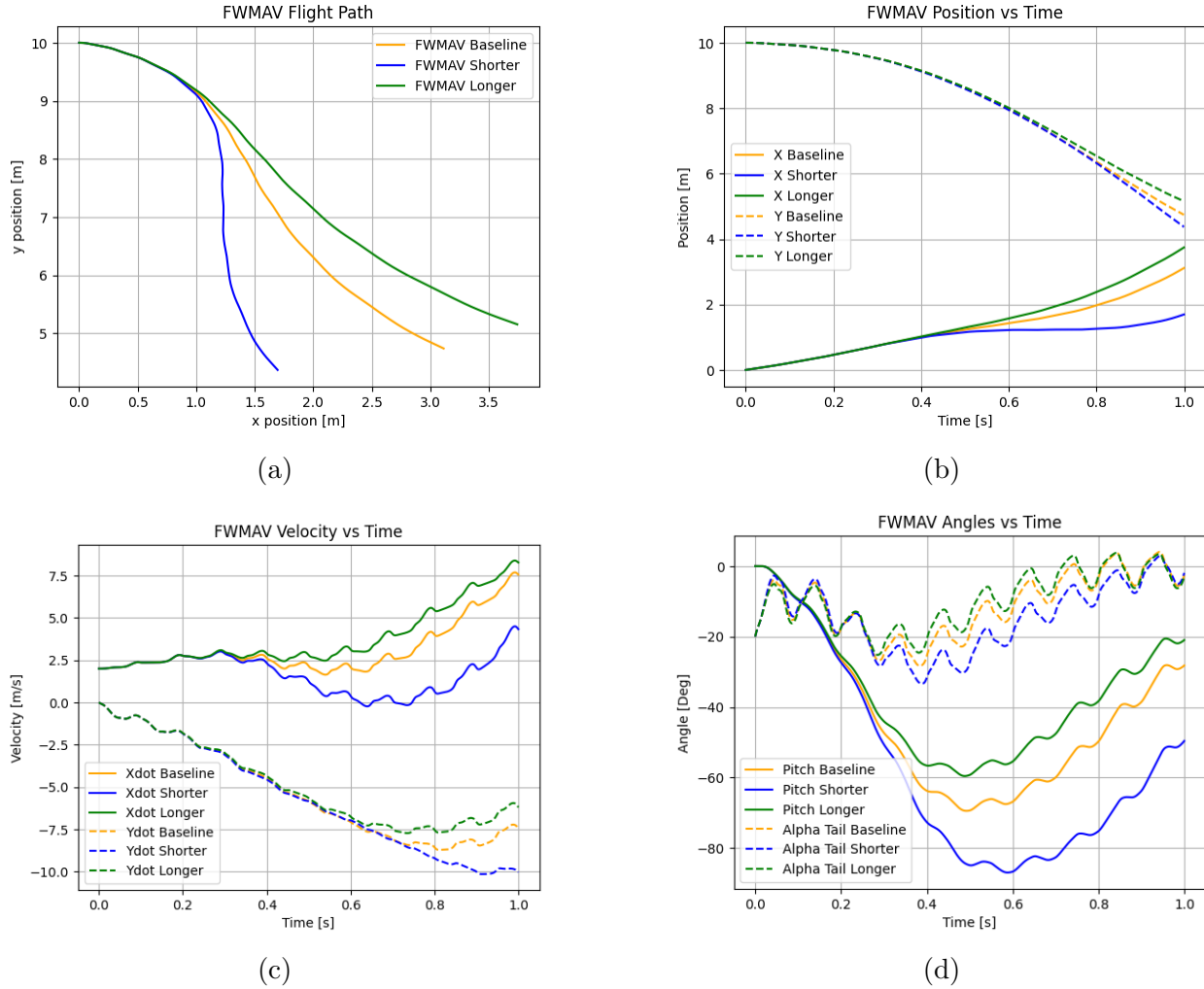


Figure 3.10: Simulation data when  $r_{tail}$  was -0.125 meters (longer) and -0.075 meters (shorter) instead of the baseline -0.1 meters. Figure 3.10a shows the flight path, Figure 3.10b shows the FWMAV's position in the global frame vs time, Figure 3.10c shows the velocity in the global frame vs time, and Figure 3.10d shows the pitch angle and the tail's angle of attack vs time. A longer tail led to a reduced minimum pitch of the FWMAV and a faster settling time, demonstrating improved stability and a shorter tail led to a greater minimum pitch and a slower settling time, demonstrating reduced stability.

### 3.3 Extended Flight and Comparison to Gliding

In addition to testing the effects of the adjustments in various wing parameters and the tail location, trials were conducted to visually inspect if the simulation worked as expected and to examine the effects of flapping vs gliding. Similar to before, the parameters were chosen with the overall scale of the CUBIRD project in mind, with the mass being 30 grams, and the flapping frequency being 9.8 Hz. The other parameters chosen were selected through trial and error and can be seen in table 3.2. In this trial, the moment of inertia,  $J_{body}$  was chosen to be  $0.9\frac{1}{12}m_{body}L_{body}^2$ , which assumes the mass distribution is smaller to that of a uniform rod, due to the fact that majority of an FWMAV's mass is located closer towards the center of mass. The initial  $x$  velocity in the simulation was  $3 \text{ m/s}$ , the initial pitch was set to  $0^\circ$ , and the initial pitch rate was set to  $1 \text{ rad/s}$  to mimic the conditions as if the FWMAV was already flying.

Figure 3.11 shows the results of one such trial. The behavior of the FWMAV in the simulation seems reasonable and could be the potential results of a real-world flight. The flight path of the FWMAV, seen in Figure 3.11a, with an expanded view in Figure A.5a, follows an oscillatory downward and forward motion, where, on average, the FWMAV is descending and moving forward, but there are times when the FWMAV is climbing in height. Oscillations can be seen in the  $x$  and  $y$  velocities in Figure 3.11c, with an expanded

Table 3.2: Parameters for Comparison of Flapping and Gliding

$m_{body}$	30.0 g
$L_{body}$	0.254 m
$r_{wing}$	0.0127 m
$r_{tail}$	-0.1 m
$\theta_{tail}$	20°
$S_{tail}$	0.01354 m <sup>2</sup>
$L_{tail}$	0.1778 m
$L_{wing}$	0.152 m
$AR_{wing}$	3.25
$f$	9.8 Hz
$\beta$	90°
$\phi_0$	10°
$\phi_{amp}$	35°
$\theta_0$	-5°
$\theta_{amp}$	7.5°
<i>Wing Shape</i>	Rectangle seen in Figure 3.1

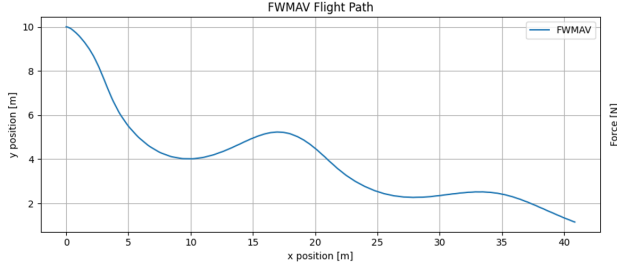
view in Figure A.6a, with small oscillations due to flapping, and large oscillations and changes due to aerodynamic effects, behaving similarly to how a glider with a large tail and large wings would behave. Examining the graph of the forces of the tail and wings in Figure 3.11b, with an expanded view in Figure A.5b, shows the relative impact that the tail and wings have on the motion of the FWMAV. The wing flapping force is magnitudes larger than the tail's forces, implying that the majority of the translation motion is due to the flapping rather than any gliding effects from the tail. The tail however plays a vital role in stabilizing the pitching of the FWMAV since its forces are further away from the center of mass, creating a larger moment.

The pitch of the FWMAV, seen in Figure 3.11d, with an expanded view in Figure A.6b, also has small oscillations that are related to the forces from

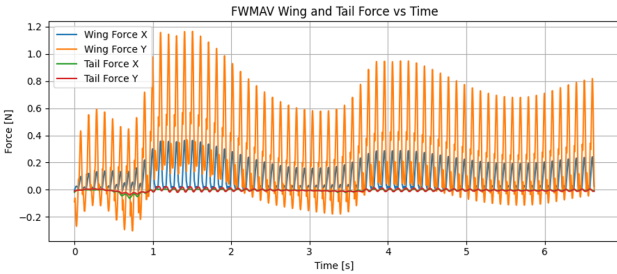
the flapping wings, and the larger oscillations are related to the aerodynamic effects of the FWMAV. The angle of attack of the body and tail are typically around  $20^\circ$  apart, which is what is expected because of the tail's inclined angle. The tail's angle of attack stays close to  $0^\circ$ , showing the role that the tail has in stabilizing the pitch of the FWMAV.

This is just one example where the simulation was able to achieve a steady-state flight condition. In many other simulations, the robot behaves unpredictably, sometimes performing large loops or spiraling downwards, alluding to the unstable behavior of an uncontrolled FWMAV. Small adjustments to the size and location of the tail as well as all the wings' kinematic and physical parameters cause large differences in the behavior of the uncontrolled FWMAV.

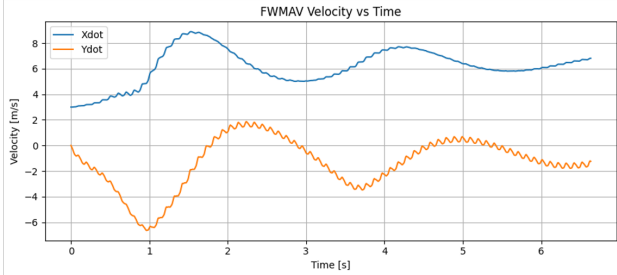
Another simulation was run to test the gliding behavior of the FWMAV. This will be a crucial component of the ultimate goal of the CUBIRD project since one of the guiding ideologies is to test the effects of intermittent flight. This simulation used the same parameters as the previous, found in table 3.2, and used the same initial conditions, except for the pitch rate, set to  $0 \text{ rad/s}$ , and was simulated for the same length of time, six seconds. The simulation, seen in Figure 3.12, behaves as expected, there is an initial increase in pitch due to the inclined tail, and afterward, the FWMAV displays an oscillating pitch before reaching a steady state value where the tail angle of attack is  $0^\circ$ . When comparing the gliding simulation and the initial



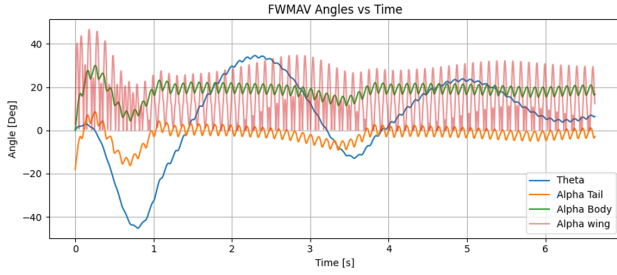
(a)



(b)



(c)



(d)

Figure 3.11: Simulation results for a 6-second simulation of flapping, with conventions from Figure 2.4. Figure 3.11a shows the flight path of the FWMAV, with an expanded view in Figure A.5a. Figure 3.11b shows the FWMAV's flapping forces in the body frame vs time, with an expanded view in Figure A.5b. Figure 3.11c shows the velocity in the global frame vs time, with an expanded view in Figure A.6a. Figure 3.11d shows the pitch angle and the tail's angle of attack vs time, with an expanded view in Figure A.6b. High-frequency oscillations can be observed due to the flapping wings, and low-frequency oscillations can be seen from the stabilizing effect from the tail of the FWMAV.

flapping test in Figure 3.11, the impact that flapping has on the motion of the FWMAV is evident. The first observation that stands out is that there are no lasting high-frequency oscillatory trends in the velocity or pitch seen in Figures 3.12c and 3.12d, which is explained by the lack of flapping wings since there are no longer high-frequency oscillatory forces being generated. The second observation, seen in Figure 3.12a is that the flapping wings not only led to a decreased height loss of 9 meters vs. 38 meters over the same time period, but also allowed the FWMAV to travel 2 meters further along the  $x$ -axis than the gliding FWMAV. For the use of intermittent flight, this information can prove valuable. If the loss of height is not a concern, then there could be a considerable advantage since there is only a small loss in the horizontal distance traveled. This, of course, would need to be explored further, as there are many factors that are integral to determining the efficiency of intermittent flight, such as the energy required to climb the height difference, the energy expenditure when flapping, and further optimizations to increase gliding capabilities.

One challenging aspect of verifying the simulation is that the parameters that were used were found through trial and error. While the mass and flapping frequency were chosen from the CUBIRD design, the other parameters have less basis from an existing system. While these parameters may work for the simulation, there is no way to know whether a robot with these specifications would perform the same in real life without building one from scratch.

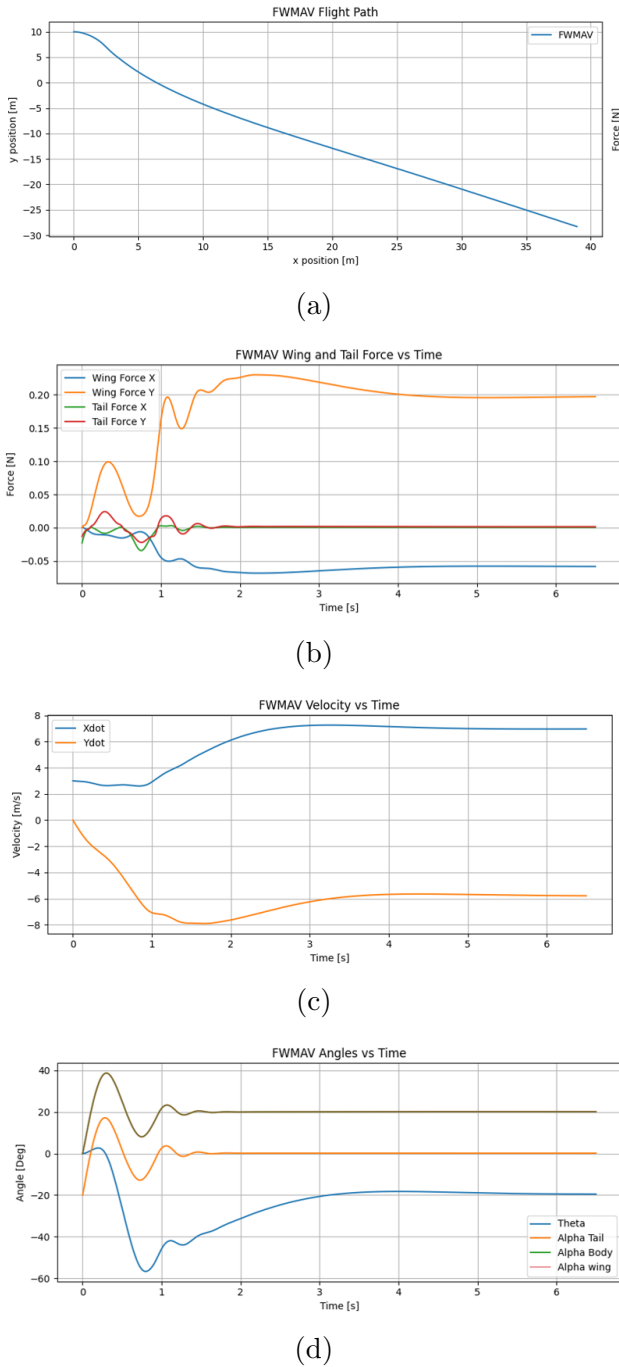


Figure 3.12: Flight data from a 6-second simulation when the FWMAV is gliding. Figure 3.12a shows the flight path of the FWMAV, with an expanded view in Figure A.7a. Figure 3.12b shows the flapping forces in the body frame vs time with an expanded view in Figure A.7b. Figure 3.12c shows the velocity in the global frame vs time with an expanded view in Figure A.8a. Figure 3.12d shows the pitch angle and the tail's angle of attack vs time with an expanded view in Figure A.8b. Compared to the flapping simulation in Figure 3.11, there are no high-frequency oscillations because there is no flapping motion. Without flapping, the tail quickly stabilizes the FWMAV and reaches an angle of attack of  $0^\circ$ .

It is therefore crucial that the simulation be tested and verified by comparing it with real-world data.

# Model Verification

## 4.1 Introduction

Developing a complex aerodynamic simulation is meaningless if the simulation does not accurately represent reality. Han [32] verified his model and simulation using an artificial wing submerged in a fluid tank, comparing the forces generated from flapping. There are, however, limitations to this as it does not factor in the changing body dynamics as it rotates and moves through the air. Ideally, the simulation would be verified by comparing the individual components of the simulation, the aerodynamic tail and body forces, and the flapping forces to real life. Since the transition and wing design of the CUBIRD FWMAV is currently being developed, there is no way to compare the flapping forces between the proposed design and simulation. Instead, to verify the full simulation, including the aerodynamics and the rigid body dynamics, the trajectory and rotation of an FWMAV in the simulation will be compared to an FWMAV flying in real life. While this will not allow for the individual forces to be compared, the general flight patterns can be evaluated providing a broad insight on whether the simulation seems to match reality.

#### 4.1.1 Comparison with the Purchased Flyer

It is integral to compare the trajectory of an FWMAV in simulation to that of real life. Since the CUBIRD FWMAV is still in development and there is no way to test its trajectory, a cheap toy FWMAV was purchased to conduct the test. The FWMAV that was chosen was the Zing Avatar Banshee<sup>1</sup> pictured in Figure 4.1. The product manual failed to enclose any specifications of the robot, so all measurements were taken by hand and the wing shape had to be approximated. The tabulated parameters of the Zing Avatar Banshee can be found in table 4.1. A ruler was used to measure distances with an accuracy of 1 millimeter and an electronic scale with an accuracy of 0.01 grams recorded the mass as 28.57 grams. The wing kinematic profiles were approximated by visually inspecting a slow-motion video, shot on an iPhone 13 at 240 Hz, stills of the slow-motion video are shown in Figure 4.2. The angles and the maximum and minimum rotation angles were extracted and plugged into Equations 2.52 and 2.53. One major difficulty when analyzing and comparing the FWMAV to the simulation is that the Zing Avatar Banshee has flexible wings that deform and rotate non-uniformly significantly during flapping. During the upstroke and downstroke, the fabric wing changes shape from the air resistance and creates a parachute-like shape. The non-rigid wings are a major concern since the blade element theory is only valid for rigid wings. Because of this two trials were conducted: one with the standard Zing Avatar

---

<sup>1</sup><https://www.amazon.com/Zing-Avatar-Banshee-Control-Drone-Tech/dp/B0B7575PVL>

Banshee and a second with chords made of carbon fiber added to the wings to reduce deformation and to create a more rigid wing.



Figure 4.1: Image of the Zing Avatar Banshee.



Figure 4.2: Film stills of slow-motion video capturing the flapping motion of the Zing Avatar Banshee. The first image shows the beginning of the downstroke, with the time underneath, and the last image shows the end of the upstroke.

The flight of the Zing Avatar Banshee was recorded with Vicon motion capture cameras with a sampling rate of 100 Hz. The FWMAV was equipped with six infrared reflective markers, each weighing 1.28 grams, increasing the

Table 4.1: Zing Avatar Banshee Specifications

$m_{body}$	28.57 g
$L_{body}$	0.254 m
$r_{wing}$	0.0254 m
$r_{tail}$	-0.1 m
$\theta_{tail}$	20°
$S_{tail}$	0.01354 m <sup>2</sup>
$L_{tail}$	0.1778 m
$L_{wing}$	0.152 m
$AR_{wing}$	3.25
$f$	17.5 Hz
$\beta$	90°
$\phi_0$	10°
$\phi_{amp}$	35°
$\theta_0$	-5°
$\theta_{amp}$	7.5°
Wing Shape	Trapazoidal, show in Figure 4.3

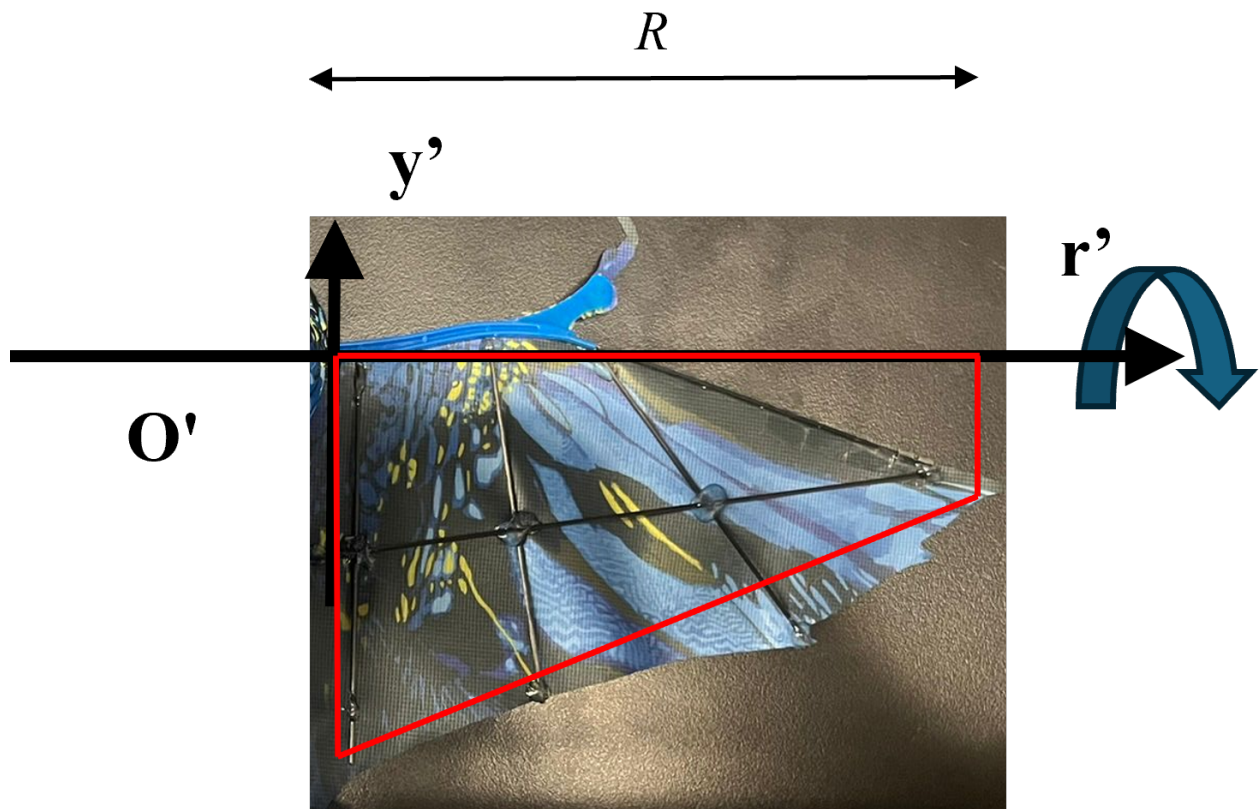


Figure 4.3: The trapezoidal wing approximation used in the model verification overlaid onto the wing of the Zing Avatar Banshee.

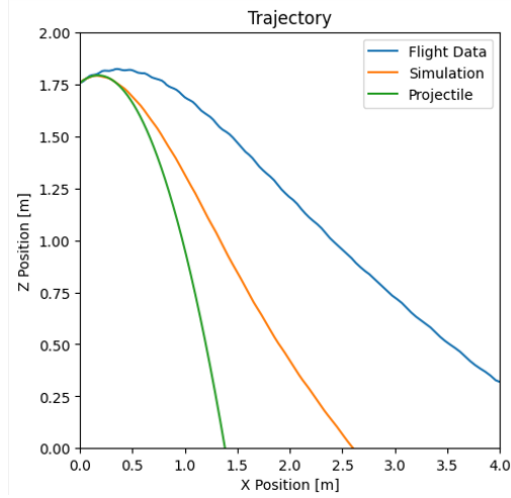
total mass of the robot by 26.88% to 36.25 grams. In the initial test, 3 markers were placed on the head of the body, 1 marker was placed on the top of the body at the end of the wings, and 2 markers were placed on the wings to verify the flapping frequency. After the first test, the markers on the wings were removed because the added weight on the wings was suspected of preventing the FWMAV from flying correctly. The FWMAV was turned on and was given time to reach the maximum flapping frequency before being thrown with an initial velocity and pitch angle, aiming for  $0^\circ$ . The position and rotation data, given as positions and rotations along the global  $x$ ,  $y$ , and  $z$  axes, were recorded in the Vicon desktop app and were exported as an Excel spreadsheet.

The Zing Avatar Banshee comes with a built-in controller that adjusts the flapping frequency, which in turn adjusts the pitch and flight speed, used for maintaining height and basic obstacle avoidance. This is a concern since we cannot track the changing flapping frequency which is a key component in the governing dynamics of the vehicle. Prior to the attachment of the tracking markers to the body, the Zing Avatar Banshee was flown and was able to fly at level height, and increases in the flapping frequency would result in the FWMAV climbing in altitude. After the tracking markers were attached, even when flapping at its now maximum frequency of 16.5 Hz, the FWMAV was unable to climb in height or even maintain level flight due to the added mass on the FWMAV. Although the Zing Avatar Banshee was

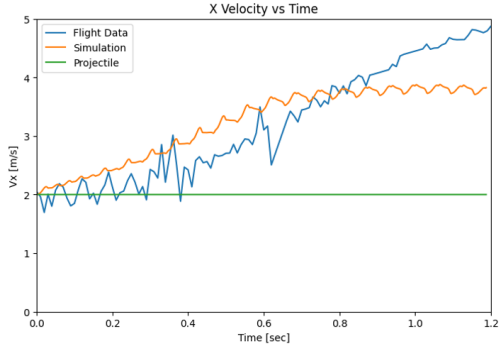
no longer able to fly, it was actually beneficial for comparing the simulation to real-world flight as there is now a constant flapping frequency that can be input into the simulation. One interesting takeaway from adding the markers was that it showed the fragility in the design of an FWMAV, as even a small increase in mass completely prevented the FWMAV from flying. This shows the importance of designing an adaptable simulation environment and control method, since small adjustments may require the reworking of an entire design.

Figure 4.4 shows the recorded flight results compared with the simulated results as well as standard projectile motion. Since the FWMAV was no longer able to fly and was instead experiencing "controlled falling", projectile motion was included in the results as a benchmark to visually assess the effects of flapping. The projectile motion equations integrate the position and velocity over time based on the initial conditions and the effects of gravity and neglect any effects from air resistance. The  $x$  position and velocity equations are given as  $x = x_0 + v_{x_0}t$  and  $v_x = v_{x_0}$ , and the  $z$  position and velocity are given as  $z = z_0 + v_{z_0}t - 0.5gt^2$  and  $v_z = v_{z_0} - gt$ . The initial conditions used in the simulation were the same value as the first entry in the recorded data to best mimic the flight of the FWMAV.

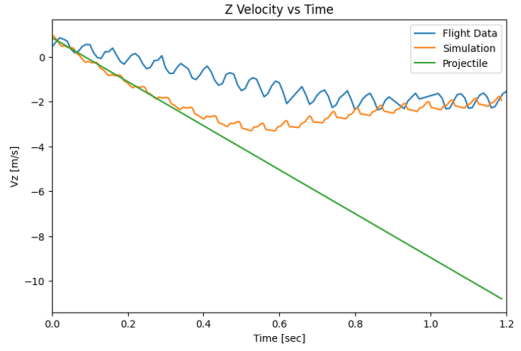
As expected, there are differences between the simulation and recorded flight data. Two immediate observations stand out, the difference in the  $z$  position and velocity, and the difference in the magnitude of the oscillations



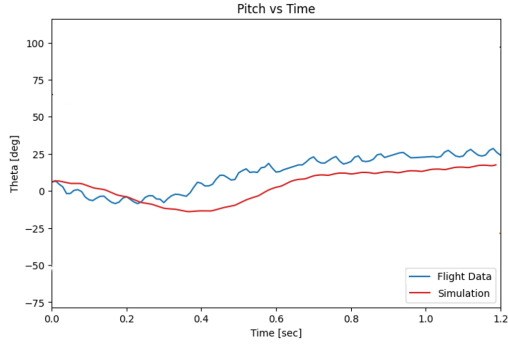
(a)



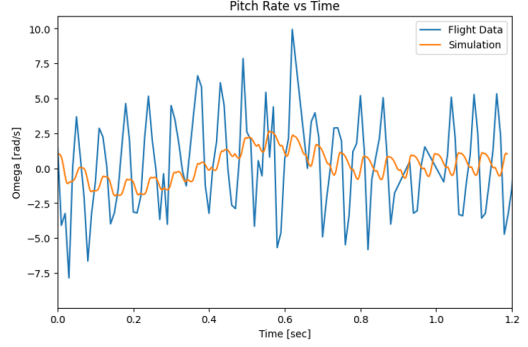
(b)



(c)



(d)



(e)

Figure 4.4: Initial flight test comparison of the purchased FWMAV to the simulation. Figure 4.4a shows the flight path. Figure 4.4b shows the  $x$  velocity in the global frame vs time. Figure 4.4c shows the  $z$  velocity in the global frame vs time, where the  $z$  axis used to record the flight data corresponds to the  $y$  axis in Figure 2.3. Figure 4.4d shows the pitch vs time. Figure 4.4e shows the pitch rate vs time. In this flight, the FWMAV was equipped solely with tracking markers and had flexible and compliant wings.

in the pitch angle  $\theta$  shown in Figure 4.4e. The recorded flight data shows the FWMAV increases in height slightly before descending at an almost constant rate. The simulation on the other hand predicts the  $z$  velocity to initially follow the velocity of simple projectile motion, decreasing at a constant rate, but as time passes, it diverges and becomes similar to the recorded flight data, leveling out at around the same velocity of  $-2 \text{ m/s}$  as seen in Figure 4.4c. As the magnitude of the velocity increases, the aerodynamic forces from the tail grow, adding more drag and lift forces, leading to a decrease in the  $x$  velocity and an increase in the  $z$  velocity. The simulated pitch angle follows a similar profile to the recorded flight data, initially decreasing in pitch before increasing and maintaining a steady level, shown in Figure 4.4d. The main difference between the two is that the recorded flight data has visible oscillations in the pitch angle and settles at a higher pitch compared to the simulation.

The differences between the simulation and the recorded data can be explained by the unmodeled physics in the simulation, particularly the non-rigid wings, with some additional effects from the body aerodynamics and the wing and tail shape approximations. As mentioned earlier, the deformable wings create a quarter-sphere shape during the upstroke and downstroke, having rotation angles that vary radially and chord-wise along the wing. The added weight on the wings also increases the flapping forces due to the inertial effects of the non-negligible mass, which are not captured in the flapping model. The

changes in the wing's shape result in increased forces, ultimately resulting in larger oscillations in the position and pitch of the FWMAV. The wings of the Zing Avatar Banshee are connected and have a larger total surface area than the approximation used in the simulation.

#### **4.1.2 Comparison with the Purchases Flyer Modified with Rigid Wings**

After testing the Zing Avatar Banshee as it initially came, the FWMAV was equipped with carbon fiber rods attached to each wing to increase its rigidity, and two of the tracking markers were removed to further reduce the weight, as seen in figure 4.5. Each carbon fiber rod had a diameter of 2 mm, and the total weight of the Zing Avatar Banshee with the tracking markers and the carbon fiber rods was 35.15 grams. The carbon fiber rods only added 1.46 grams to the total weight of the robot with the four markers attached, increasing the weight by only 4.33%, a negligible amount compared to the weight from the markers. Carbon fiber was chosen for its low weight, as any additional weight on the wings will add an inertial effect, increasing the expected force output from the wings [35]. Even the small adjustment of weight on the wings caused a significant decrease in the flapping frequency, going from 17.5 Hz to 10.56 Hz, a considerable decrease. This can largely be attributed to the cheap motor used to drive the wings, which likely applies just enough torque for the initial wings to flap at the desired frequency. The

lack of flexibility in the wings leads to larger forces resisting the movement of the wings, which the motor must overcome to maintain the same flapping frequency. Although the wings were still not completely rigid, as seen in image 2 in Figure 4.2, there was a drastic increase in the accuracy of the simulation compared to the first trial.

A total of 15 trials were conducted, and the data was recorded from each test. Each flight's data was manually inspected to ensure that the Zing Avatar Banshee flew in a relatively straight line along the global  $x$ -axis and the data that was selected only included data points from when the FWMAV was in the air. The robot was thrown with different initial velocities, as well as at different pitch angles. The range of the initial  $x$  velocity ranged from 1.43 to 2.74  $m/s$ , and the pitch ranged from  $-38.38^\circ$  to  $21.77^\circ$ . It was important to get a wide range of trials to compare the simulation to, as it will help illuminate where any pitfalls and strengths occur.

Overall, the simulation results roughly matched up with the flight data, with the closest match shown in Figure 4.8. In most cases, the simulation pitch would follow a similar trend to the pitch of the recorded data, but with a delay that increases with time. This delay can also be seen in the  $z$  velocity since the simulated FWMAV typically followed projectile motion for the first 2-3 periods of flapping before transitioning to match the recorded flight data. This is likely because the aerodynamic surfaces of Zing Avatar Banshee are made of fabric, as opposed to the rigid bodies used in the simula-

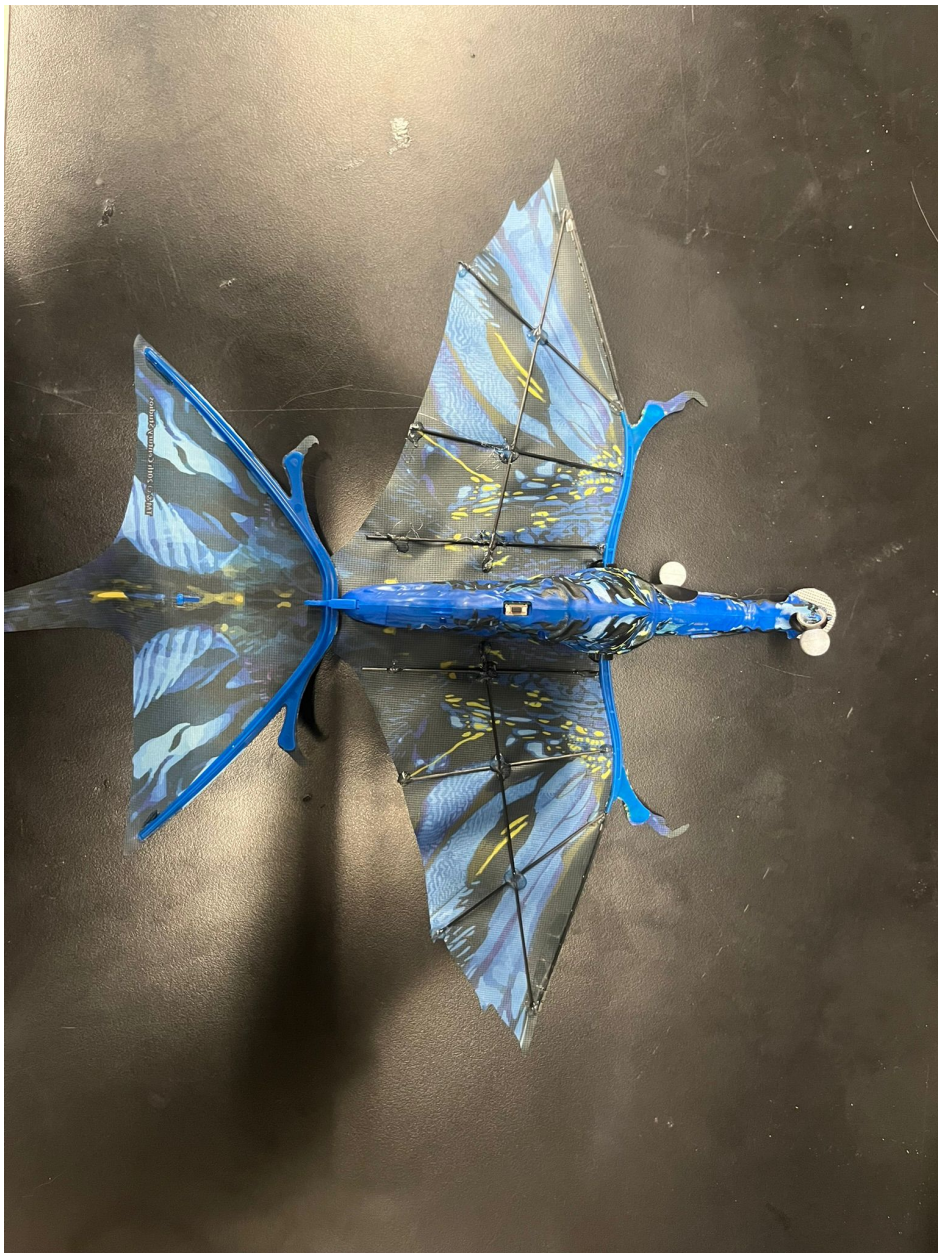


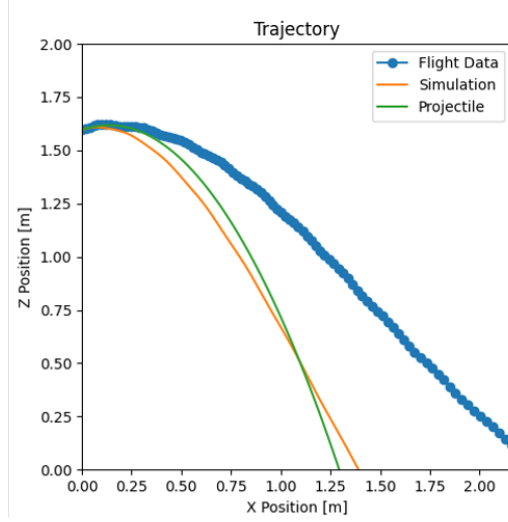
Figure 4.5: Zing Avatar Banshee equipped with carbon fiber chords. The carbon fiber chords increased the rigidity of the wing without adding significant weight.

tion aerodynamic model. The aerodynamic forces of the rigid bodies increase as the magnitude of the velocity grows, so as the velocity increases, steady-state aerodynamics can begin to be seen. The largest discrepancies between the flight data and the simulation came when the Zing Avatar Banshee was thrown forward with an initial large pitch angle in the positive or negative direction. This correlated to large angles of attack, with magnitudes above  $40^\circ$ , which is typically when the simulation diverges from reality. This is expected as the simulation uses a flat-plate approximation for the aerodynamics, and the body and tail of the robot are not actually flat plates.

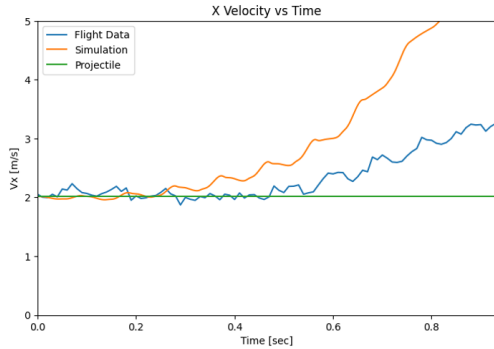
Figures 4.7, 4.8, and 4.9 highlight three of the simulations compared with the recorded flight data, the average simulation, the most accurate simulation, and the worst simulation, respectively. In all the comparisons, the initial conditions for the simulations were automatically calculated by averaging the first three values of the pitch angle and the translational and rotational velocities. The initial wing angles were manually adjusted, by adding a lag or lead to the wing kinematic equations from 2.52 and 2.53, to match the simulated results with the flight data. Even with the same initial conditions, the simulation would behave differently when starting with the wing in an upstroke or downstroke which can be seen in Figure 4.6 and Figure 4.7. The initial conditions used in the simulations were: an initial pitch of  $10.89^\circ$ , an  $x$  velocity of  $2.02 \text{ m/s}$ , a  $z$  velocity of  $0.62 \text{ m/s}$ , and a pitch rate of  $-1.08 \text{ rad/s}$ . Both these figures represent the same trial and simulation, with the

only difference being that the initial wing kinematics now matched up with the recorded data more accurately, having peaks in the  $z$  velocity at the same time as the flight data, as opposed to the initial test that started with an upstroke. The simulation with the correct initial flapping kinematics matches the flight data better in all the translational and rotational positions/angles and velocities.

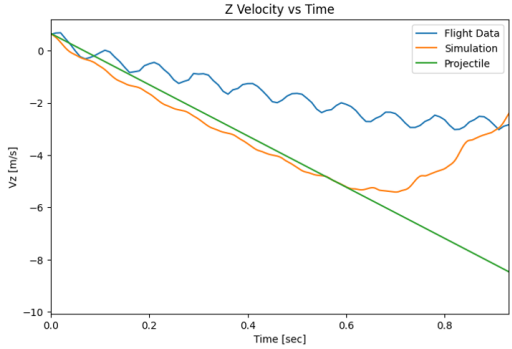
Figure 4.7 shows the flight recording that represents the average simulation and flight data comparison. This trial was chosen because it fell in between the more accurate comparisons and the least accurate, giving a better gauge of the simulation's accuracy. In this example, the robot had an initial pitch of  $10.89^\circ$ , an  $x$  velocity of  $2.02\text{ m/s}$ , a  $z$  velocity of  $0.62\text{ m/s}$ , and a pitch rate of  $-1.08\text{ rad/s}$ . Here, the trajectory of the simulation falls between the flight data and projectile motion, however as time increases, it starts to trend more towards the flight data. The  $x$  velocity initially stays steady around  $2\text{ m/s}$ , but quickly begins to increase before the recorded data begins to, as seen in Figure 4.7b. Conversely, the  $z$  velocity initially behaves like projectile motion, decreasing at a relatively steady rate, before increasing to a similar level, seen in Figure 4.7c. The  $x$  velocity appears to lead the true behavior, while the  $z$  velocity appears to experience lag. The lag can also be seen in the pitch angle, shown I Figure 4.7d, where the simulated FWMAV's pitch initially followed the flight data before ultimately falling behind. The pitch rate can provide insight into this behavior. While the simulated and recorded FWMAV data



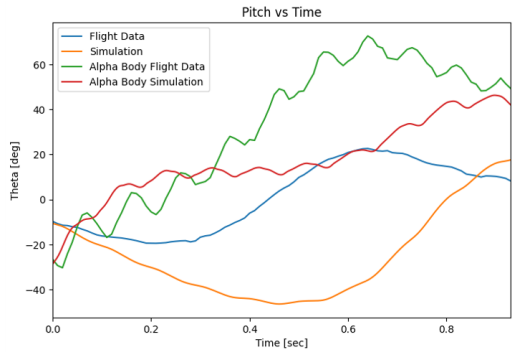
(a)



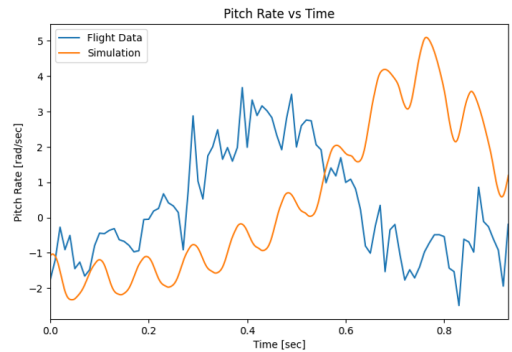
(b)



(c)



(d)

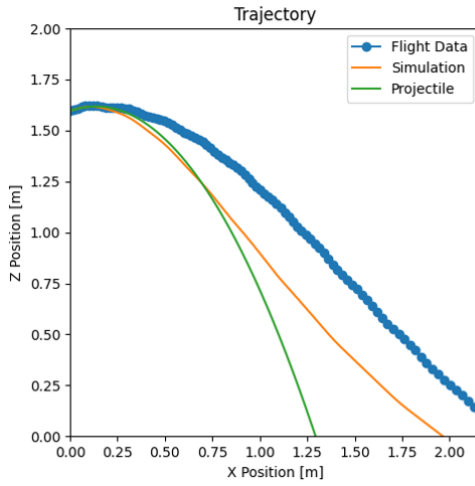


(e)

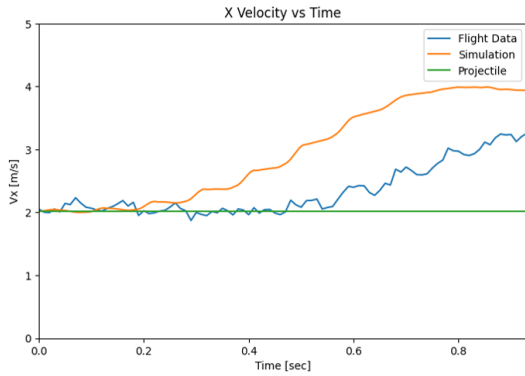
Figure 4.6: Initial comparison between the simulation and the recorded data with the Zing Avatar Banshee with carbon fiber chords along the wing. Figure 4.6a shows the flight path, Figure 4.6b shows the  $x$  velocity in the global frame vs time, Figure 4.6c shows the  $z$  velocity in the global frame vs time, Figure 4.6d shows the pitch and body's angle of attack vs time, and Figure 4.6e shows the pitch rate vs time. In this simulation, the wing kinematics started with an immediate upstroke and did not model the flight of the Zing Avatar Banshee correctly.

both show similar pitch rate profiles, shown in Figure 4.7e, increasing in pitch rate before slowly decreasing, the flight data is considerably faster even though the pitch rates have similar magnitudes in the higher frequency pitch rates (due to flapping) and the lower frequencies (due to the aerodynamic effects). These differences can be due to the changing wing kinematics that occurs during forward flight. The wing kinematics used in the simulation were taken from the Zing Avatar Banshee flapping while stationary, but these kinematics can change when there is the addition of aerodynamic forces that occur in forward flight.

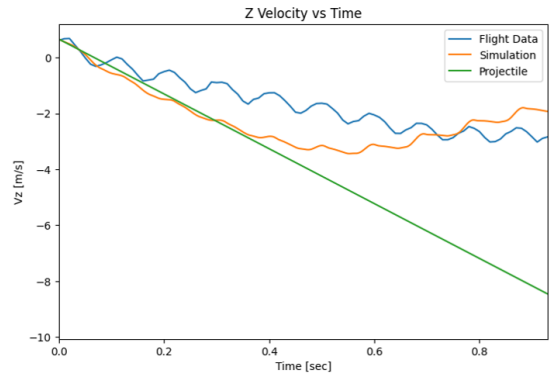
Figure 4.8 shows the flight recording that aligns the best with the simulation, where the high-frequency oscillations are in near-perfect sync with one another, and an angle of attack is low enough to not cause major deviations due to the aerodynamic approximations. In this flight, the robot was thrown forwards with an initial pitch of  $21.77^\circ$ ,  $x$  velocity of  $1.61\text{ m/s}$ ,  $z$  velocity of  $0.40\text{ m/s}$ , and an initial pitch rate of  $-0.58\text{ rad/s}$ . The simulated flight path, shown in Figure 4.8a, aligns almost perfectly with the recorded data, although the  $x$  and  $z$  positions diverge from one another slightly. Still, the trends stay the same. The pitch and pitch rate of the FWMAV follow similar trends and are of similar magnitudes as seen in Figure 4.8d. The  $z$  velocity follows a similar shape to the recorded data but maintains a slightly higher steady-state velocity, seen in Figure 4.8c. In comparison, the simulated  $x$  velocity, in Figure 4.8b, is lower than the recorded data but follows a similar



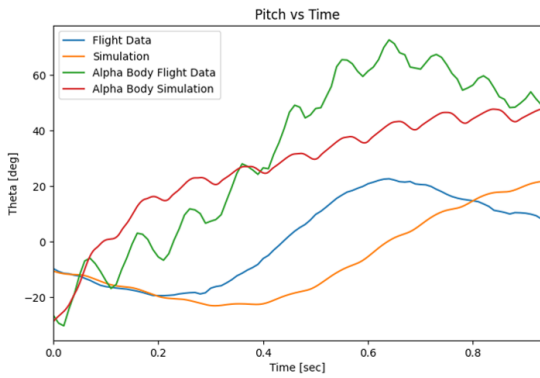
(a)



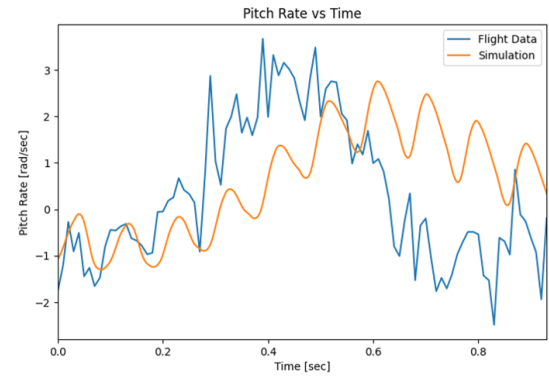
(b)



(c)



(d)

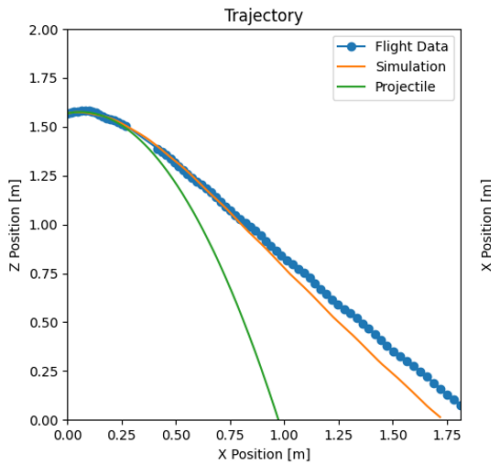


(e)

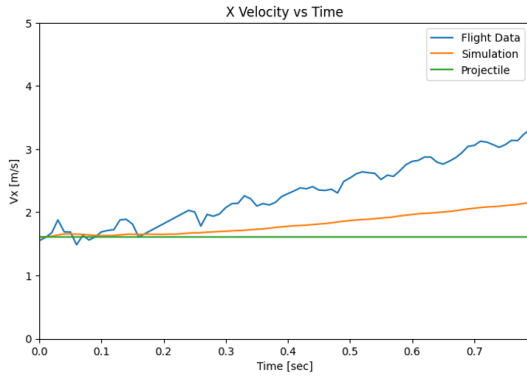
Figure 4.7: The average trial and comparison between simulation data and flight data. Figure 4.7a shows the flight path, Figure 4.7b shows the  $x$  velocity in the global frame vs time, Figure 4.7c shows the  $z$  velocity in the global frame vs time, Figure 4.7d shows the pitch and body's angle of attack vs time, and Figure 4.7e shows the pitch rate vs time. This simulation roughly emulates the motion of the FWM MAV.

trend of constant growth. Interestingly, the simulated velocities diverge in different directions, the  $x$  velocity is lower than the recorded data, and the  $z$  velocity is higher. This can likely be explained by the fabric material that comprises the aerodynamic surfaces which can morph and change the lift and drag forces. The angle of attack comparison and vehicle pitch further indicate that the simulation is working as expected. The angle of attack of the body in the simulation and collected data increase rapidly in the beginning, before settling between 50-60°. The pitch of the robot also follows similar behavior, although the simulation pitch does not oscillate with the same magnitude.

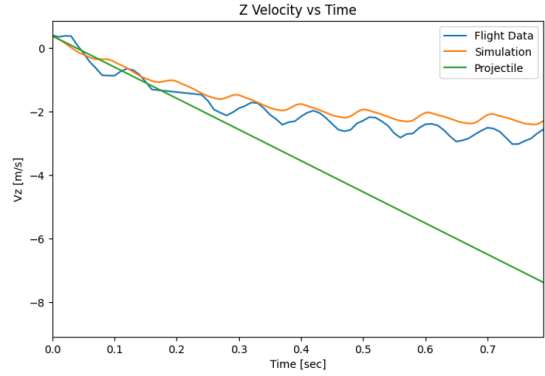
Figure 4.9 shows the flight recording that diverged the most from the simulation. In this test flight, the FWMAV had an initial pitch of -40.1°, an  $x$  velocity of 1.88  $m/s$ , a  $z$  velocity of 0.41  $m/s$ , and a pitch rate of -1.77  $rad/s$ . The initial angle of attack of the FWMAV was -54.35° considerably larger in magnitude than the other test cases. In this test case, the simulation performed worse than standard projectile motion. While the  $x$  velocity of the simulation roughly aligned with the flight data, the simulation's  $z$  velocity was significantly lower than the recorded flight data and exhibited minuscule oscillatory behavior seen in Figure 4.9c. Conversely, the oscillatory behavior from flapping can be seen in the pitch rate in Figure 4.9e, however, the pitch rate increases at a significantly slower rate than the recorded data. The pitch itself strays further from the recorded data and the angles of attack seemingly have no correlation to one another due to the stall conditions induced by the



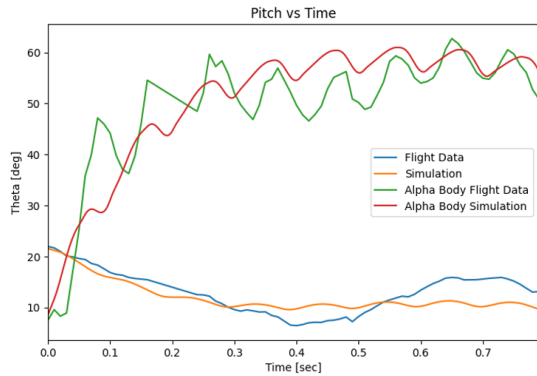
(a)



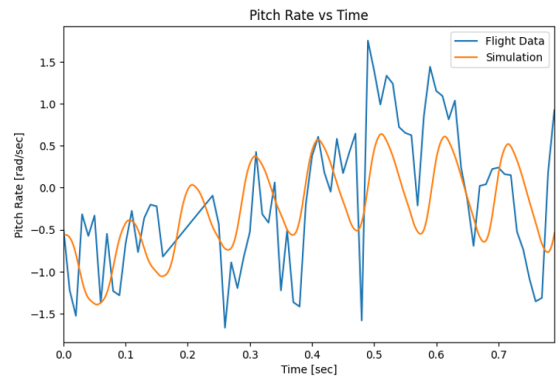
(b)



(c)



(d) The FWMAV's pitch and the body's angle of attack vs time.



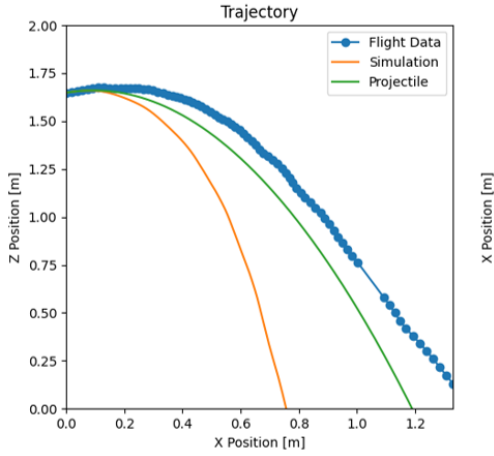
(e)

Figure 4.8: The best comparison between simulation data and flight data. Figure 4.8a shows the flight path, Figure 4.8b shows the  $x$  velocity in the global frame vs time, Figure 4.8c shows the  $z$  velocity in the global frame vs time, Figure 4.8d shows the pitch and body's angle of attack vs time, and Figure 4.8e shows the pitch rate vs time. Here, the simulation predicted the motion and orientation of the FWMAV most accurately.

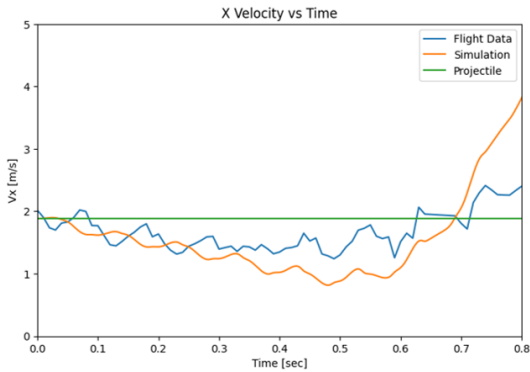
large initial angle of attack.

The recorded flight data presented an interesting observation. In all the trials, regardless of the initial conditions in velocity or pitch, the Zing Avatar Banshee appeared to adjust the pitch to  $20^\circ$ , regardless of the angle of attack. Typically with gliders, the equilibrium point is where the angle of attack is around  $0^\circ$ , but for this robot, the equilibrium appeared to be a pitch angle.

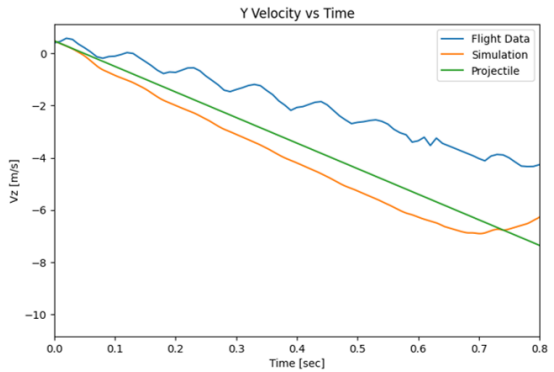
Although the simulated data does not line up precisely with the recorded data, it demonstrates that the simulation environment can be used to simulate an FWMAV. Even with the many approximations used to simulate the Zing Avatar Banshee, similar behaviors and trends, such as the pitch profile and oscillations seen in the velocities, were exhibited in the simulation and real life. The most accurate simulation closely mimicked the flight path and pitch of the Zing Avatar Banshee and even the average test cases captured the essence of the trajectory and pitch profiles of the recorded data. The differences in the  $x$  and  $z$  velocities can be traced back to the pitch angle of the FWMAV. The more inclined the FWMAV is, the larger the  $x$  velocity is and the smaller the  $z$  velocity is, which is supported by the fact that the vertical component of the flapping force is larger than the horizontal component. The most stark contrasts arose when the initial angle of attack of the robot was large, typically above  $30^\circ$  or below  $-30^\circ$ , demonstrating some of the pitfalls in the current simulation. The differences between the simulation and reality largely stemmed from the unmodeled aerodynamic stall



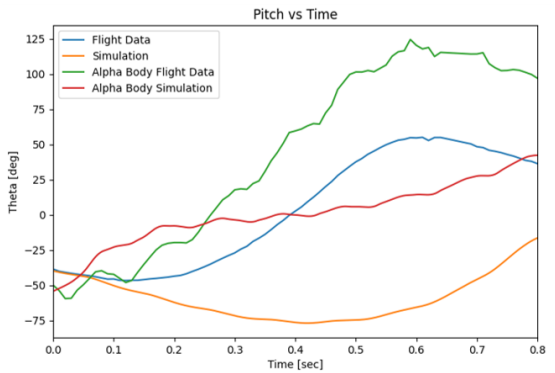
(a)



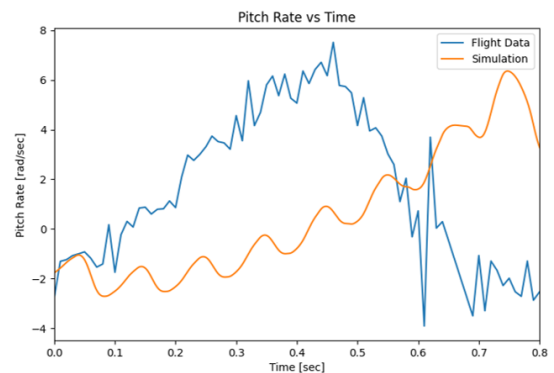
(b)



(c)



(d)



(e)

Figure 4.9: The worst comparison between simulation data and flight data. Figure 4.9a shows the flight path, Figure 4.9b shows the  $x$  velocity in the global frame vs time, Figure 4.9c shows the  $z$  velocity in the global frame vs time, Figure 4.9d shows the pitch and body's angle of attack vs time, and Figure 4.9e shows the pitch rate vs time. In this simulation, the model performed significantly worse than the projectile motion simulation in predicting the trajectory of the FWMAV. The simulation also did not capture the pitch pattern of the flight data, having a significant decrease before pitching upwards.

effects and approximations used for the simulation rather than from the flapping aerodynamics producing completely incorrect results and are discussed further in the subsequent section.

## 4.2 Limitations

One of the main limitations of this study was that the purchased FWMAV used for comparing the simulation to real-world data is difficult to model accurately. The shape of the robot is irregular and the wings and tail are made from a cloth-like material causing deformations in the wings and tail which result in different aerodynamic forces than one would expect from rigid components. Additionally, the robot did not possess two distinct wings, rather they were connected and part of the same piece of fabric, further complicating the aerodynamics. Finally, there is unmodelled behavior resulting from the interaction of the flapping wings and the tail. The tail is not only affected by the airflow as the robot moves, but it also has the addition of the airflow caused by the wakes and vortices generated by flapping. This can cause unexpected lift and drag forces that are not captured in the simulation.

The largest causes of error can be attributed to the aerodynamic effects from the tail and body, as well as the approximation used for the wing's shape and wing kinematics. This is apparent when the robot experiences large angles of attack as shown in Figure 4.9. When flying at low angles of attack, there are smaller drag and lift forces that occur from the body and

tail compared to larger angles of attack, but as the angle of attack increases, the approximations used in the aerodynamic models represent reality less and less do to the morphing of the aerodynamic surfaces. These properties can be difficult to mathematically model, and it would be more suitable to attain these aerodynamic properties through physical testing. These aerodynamic properties can also explain the differences in the  $x$  and  $z$  velocities, where the lift and drag forces experienced by the Zing Avatar Banshee are of different magnitudes than the simulation predicts. The differences in the magnitude of the oscillations in the  $x$  and  $z$  velocities can also be attributed to the approximation of the wing's shape and because even with the attachment of carbon fiber rods, the wings were still not completely rigid. The differences in the wing's area and the centers of pressure could increase the magnitudes of forces caused by the flapping motion, thereby increasing the magnitude of the oscillations. Additionally, the flapping wing kinematics were taken from when the Zing Avatar Banshee was flapping in still air but the flapping kinematics may change slightly when there is forward flight.

Lastly, a source of error that affects the recorded flight data is the motion capture hardware itself. The cameras used would occasionally lose track of the markers, leading to missing data entries. Additionally, the Vicon records data at 100 Hz, considering that the flight duration only lasts around 0.8 seconds on average, there are around 80 data points for each trial. While this captures the trajectory of the robot, the velocities become less accurate

due to being undersampled and due to errors that accumulate as the position gets integrated.

# Future Work and Conclusion

## 5.1 Future Work

While significant progress has been made in developing a robust simulation for FWMAV with customizable designs and configurations, there remains further work to be done, particularly in the realm of control scheme development. The primary objective of the physics simulation extends beyond merely testing initial conditions; it is crafted with the specific aim of informing the development of tailored control strategies by incorporating the dynamics of the FWMAV into controller design. Given the inherent instability of FWMAVs, a robust controller customized to the individual characteristics of each FWMAV is essential.

To advance towards this goal, three key steps are outlined. The first would be to design a test stand, along with a rigid wing and transmission system, and record the force output from the wing flapping in a wind tunnel. There would be a force and torque sensor located on the bottom of the test stand that would record the forces exerted onto it by the FWMAV. This would allow for the flapping aerodynamics to be tested and verified without having to build an entire robot. The wind speed could be set to different values and the pitch of the test stand could be adjusted to provide force and moment

data for a wide range of flight speeds as well as a wide range of potential pitch angles of the FWMAV. One limitation of this is that it would not allow for the testing of the aerodynamic forces when the robot is rotating and moving through the air. An additional upside, however, is that developing a test rig would not only allow for the wing force to be compared to the finished design, but also the aerodynamic properties of the Zing Avatar Banshee, and in the future the CUBIRD FWMAV, can be measured and modeled with higher accuracy in the physics simulation. Ideally, this test stand should possess the capability to manipulate incoming wind speed, adjust the pitch angle, and accurately measure forces and moments generated during flapping motion. Integration of a high-speed camera within this setup would further enhance the modeling of the wing kinematics, by giving a researcher the ability to see variations in the kinematics induced by changes in pitch or see non-uniform rotation angles along the radial axis of the wing.

Secondly, establishing a comprehensive understanding of the FWMAV's aerodynamics is paramount. There are two ways to further improve the aerodynamic model. The first is to buy an FWMAV with more details from the manufacturer about the key physical parameters, the body aerodynamics, and the wing's shape and kinematics would allow for a more specific simulation to be conducted. This would allow for testing to be done on the simulation code simultaneously with the continuation of the design of the CUBIRD FWMAV. The second method would involve placing the body of

different-sized FWMAVs in a wind tunnel and developing models that capture the aerodynamics based on the critical dimensions. The goal would be to develop more accurate aerodynamic models for the bodies of FWMAVs that factor in the critical dimensions. The model used for the flapping aerodynamics in the current simulation is adaptable to various wing shapes and sizes, creating an aerodynamic model with similar adaptability but for the body and tail would greatly improve the adaptability of the simulation at large.

Finally, the determination of the trim conditions, a task complicated by the inherently periodic nature of flapping forces and moments. Unlike traditional trim search algorithms, which are unsuitable for such periodic patterns, the FWMAV requires a tailored approach. This entails analyzing average forces and states over successive periods to establish equilibrium conditions over the duration of one period. While in a trimmed state, the forces acting on the FWMAV from flapping and from the aerodynamics should sum to zero. Once trim conditions are identified, various control strategies can be explored, leveraging these conditions as reference points. Advanced control schemes may exploit differential flapping frequencies or controlled wing positioning to execute maneuvers such as turns, mirroring avian flight patterns.

In implementing controllers, the linearization of aerodynamic models for flapping forces, tail, and body dynamics plays a pivotal role. These linearized models, integrated with the established trim conditions, form the foundation

for developing and implementing control algorithms tailored to the specific dynamics of each FWMAV. By addressing these steps, future research can advance the field of FWMAVs, allowing for robots of various sizes and designs to be simulated correctly and have control systems developed in an easier manner.

## 5.2 Conclusion

This thesis has addressed a crucial need within the field: the development of an open-source, adaptable physics simulation capable of accommodating FWMAVs of diverse sizes, unique wing kinematics, and arbitrary wing shapes. By organizing key components into separate files, the simulation framework offers user-friendly modifications, empowering future researchers and students to tailor the simulation to their unique FWMAV designs. Notably, the integration of automated calculations for key variables associated with different wing shapes, wing area,  $\hat{r}_2$ , and  $\hat{r}_M$ , streamlines the customization process, allowing for the easy implementation of custom wing shapes.

Central to the simulation's efficacy is a modified quasi-steady aerodynamic model, grounded in blade element theory. This model, accounts for unsteady leading edge vortex effects, rotational flow effects, and added mass effects, and forms the cornerstone of flapping aerodynamics within the simulation. While aerodynamic models for the tail and body primarily relied on airfoil and flat plate approximations, their performance in validating the simulation

against collected data proved satisfactory. Nonetheless, the pursuit of more accurate aerodynamic models remains imperative for enhancing simulation fidelity in future endeavors.

Verification of the flapping aerodynamic model was achieved through comparison with flight data from a commercially available FWMAV. Encouragingly, simulated flight data exhibited trends consistent with actual flight observations, albeit differences that can be attributed to variances in the aerodynamic properties and discrepancies between physical wings and model approximations.

In conclusion, this physics simulation represents a promising step towards the development of an open-source FWMAV simulator, doubling as a potent design tool. Its accessibility and flexibility allow for seamless adjustments to wing shape, kinematics, and physical attributes, enabling users to gain insights into their FWMAV's performance without physically building their FWMAV. Moving forward, refinements in aerodynamic modeling for the tail and body, coupled with the establishment of periodic trim conditions for controller design, stand as compelling avenues for future research and innovation in the realm of the development of accessible FWMAVs.

# Appendices

# Appendix A

## Additional Figures for Simulation Results

### A.1 Parameter Study

#### A.1.1 Forces from Different Wing Shapes

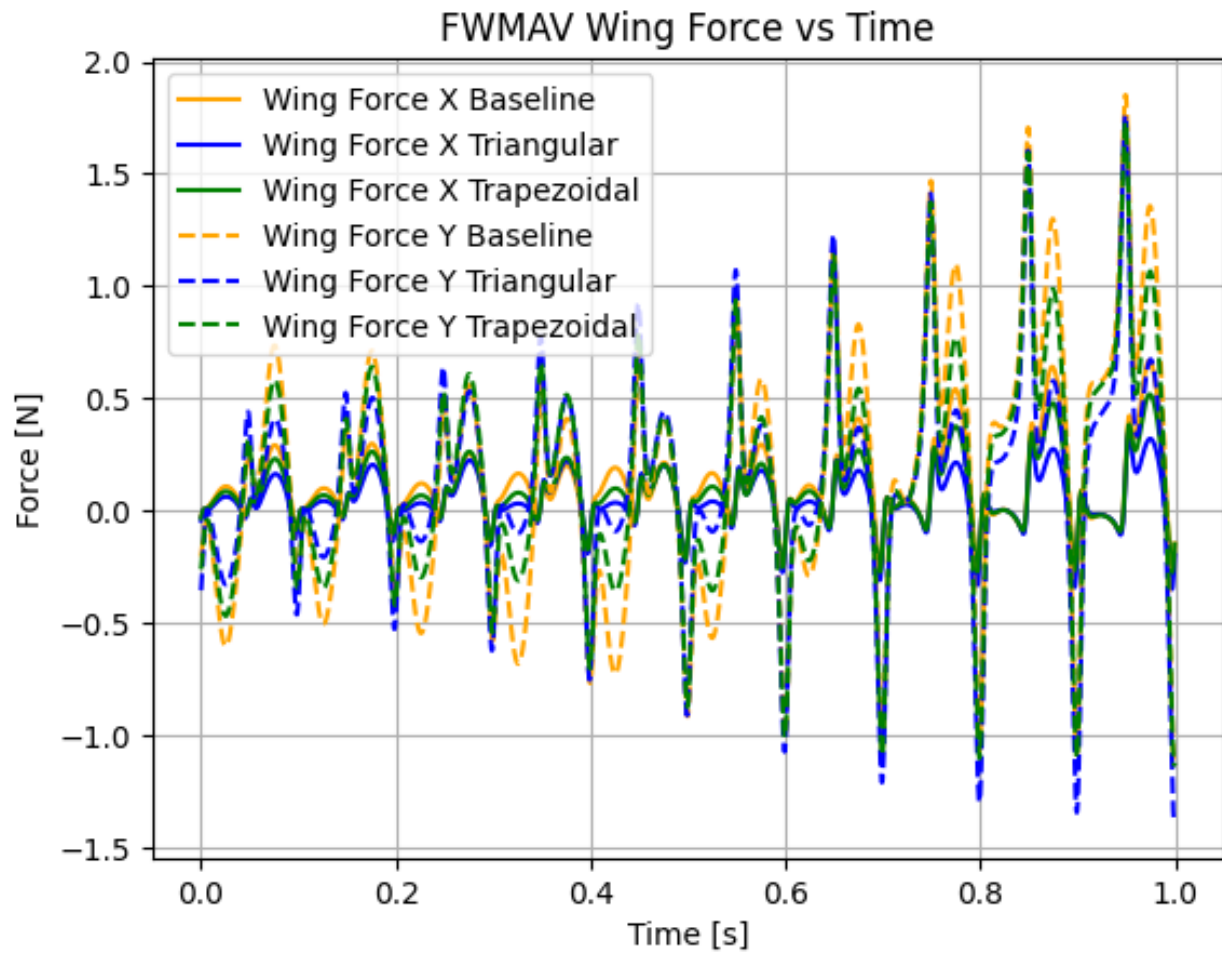


Figure A.1: Expanded image of the flapping forces seen in Figure 3.5b.

#### A.1.2 Forces from Different Stroke Amplitudes

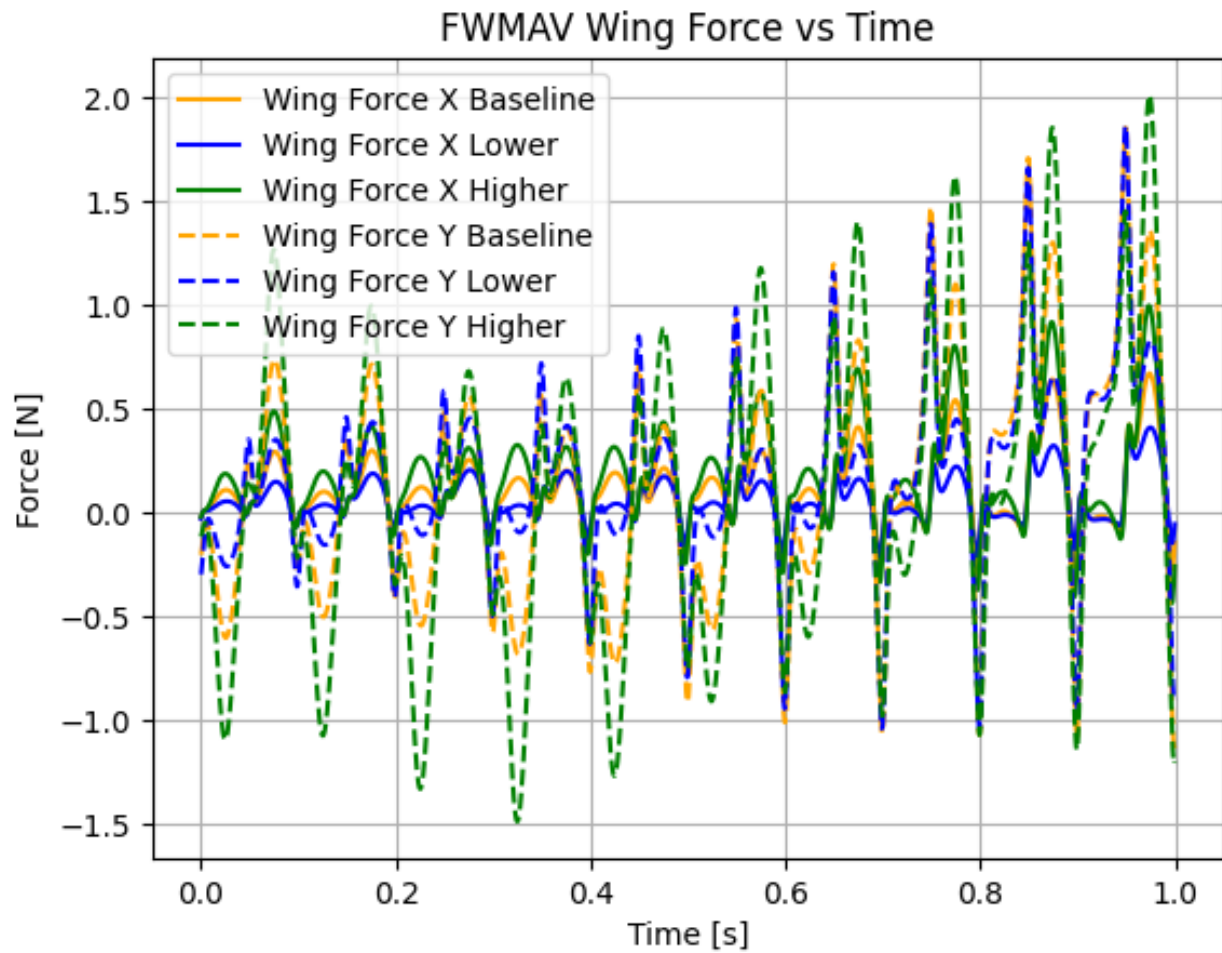


Figure A.2: Expanded image of the flapping forces seen in Figure 3.6b.

#### A.1.3 Forces from Different Rotation Amplitudes

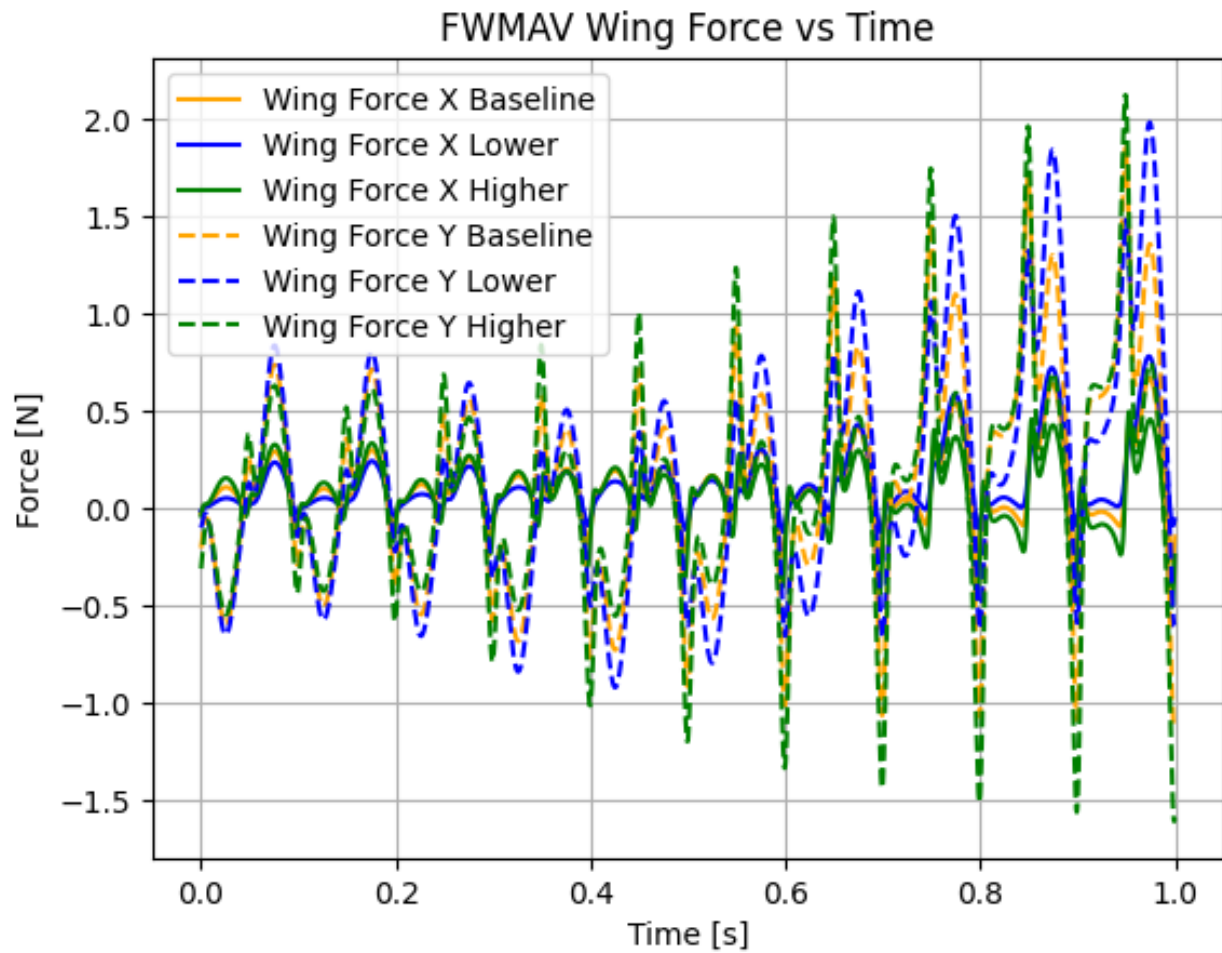


Figure A.3: Expanded image of the flapping forces seen in Figure 3.7b.

#### A.1.4 Forces from Different Flapping Frequencies

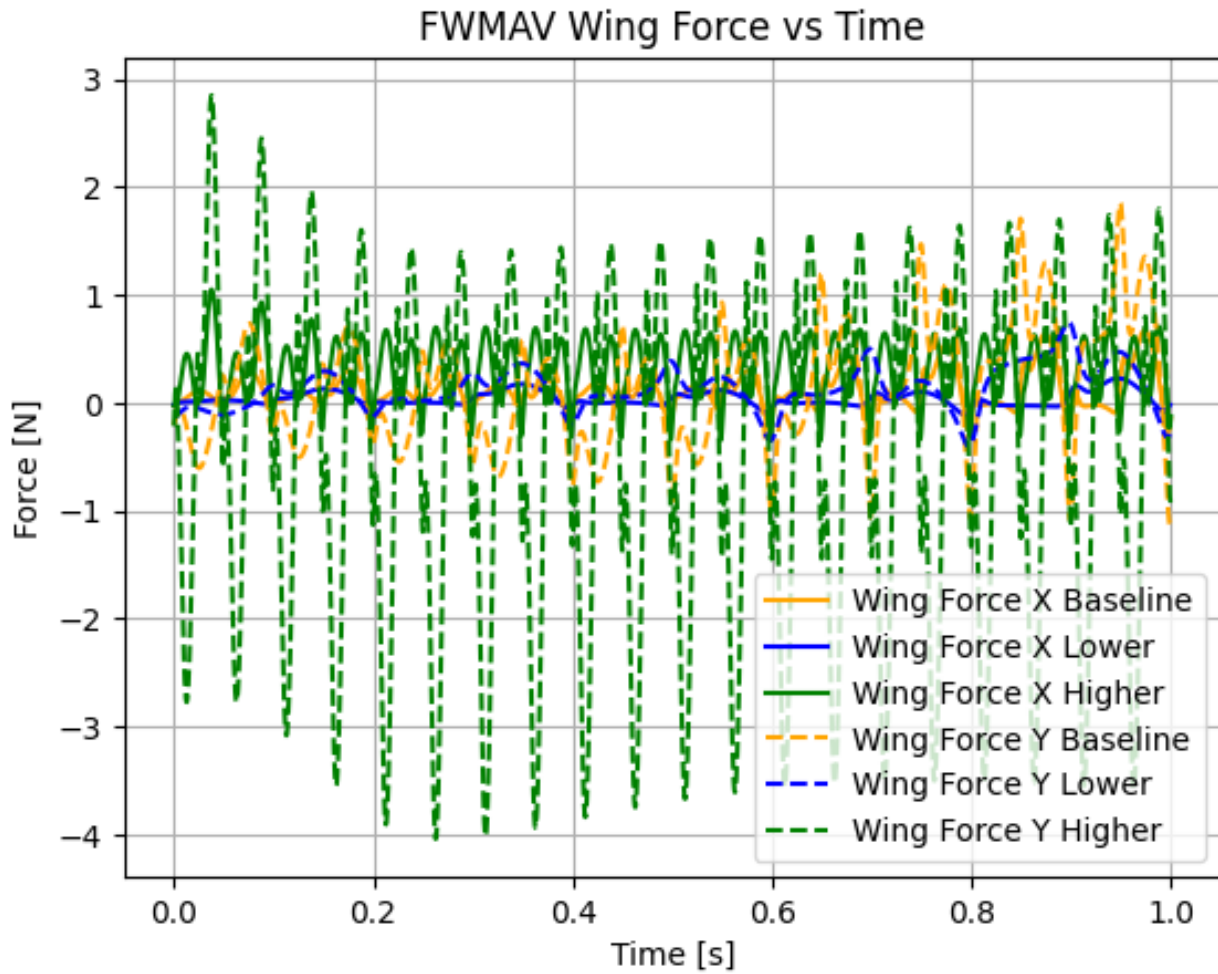
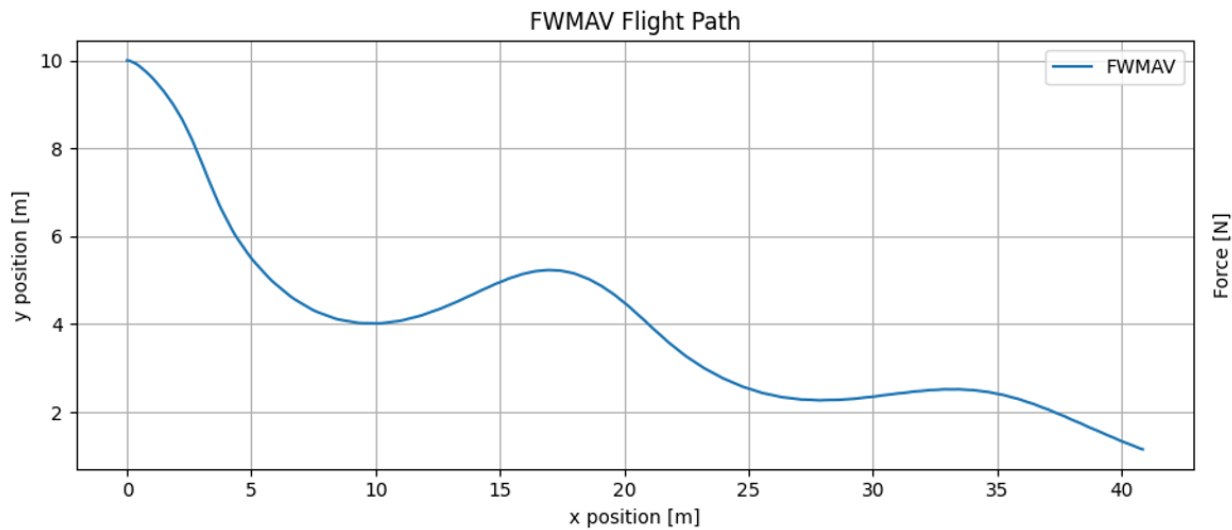


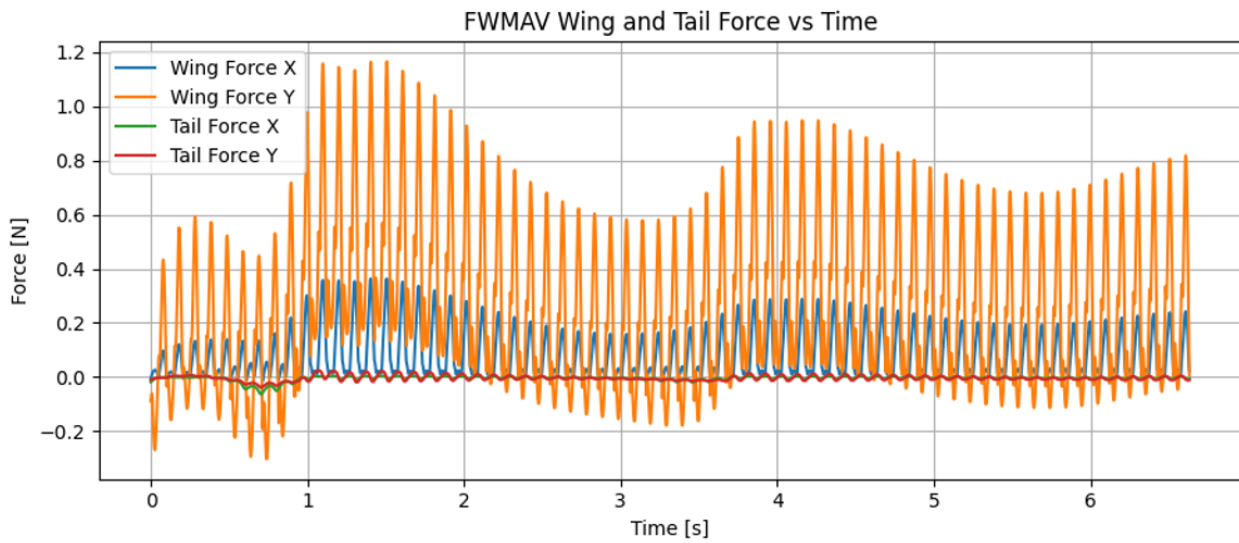
Figure A.4: Expanded image of the flapping forces seen in Figure 3.9b.

## A.2 Extended Flight and Comparison to Gliding

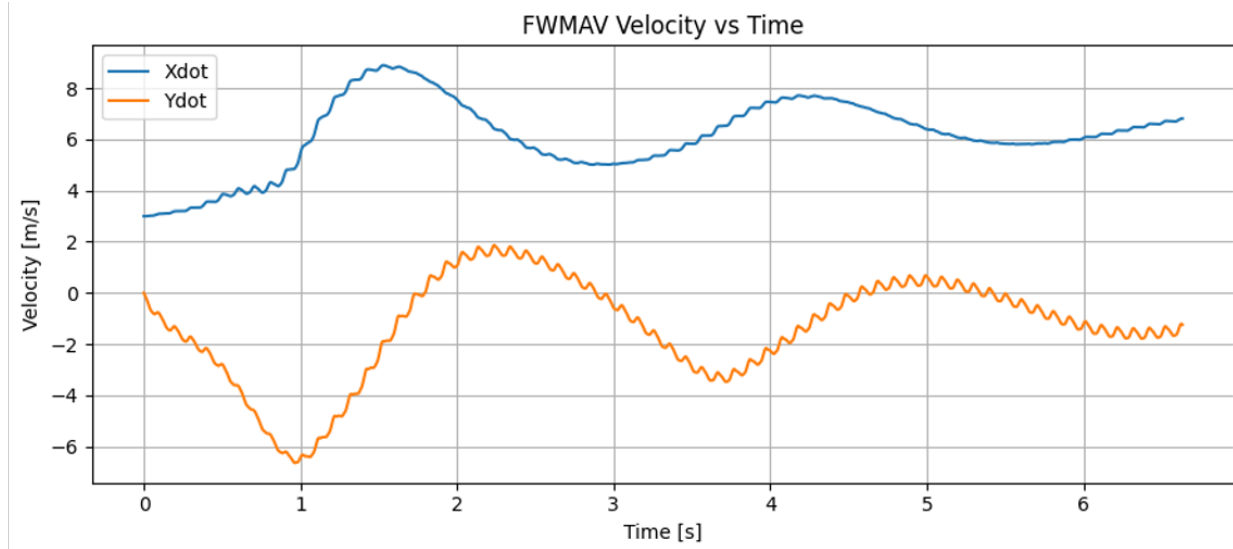
### A.2.1 Figures from Flapping Simulation



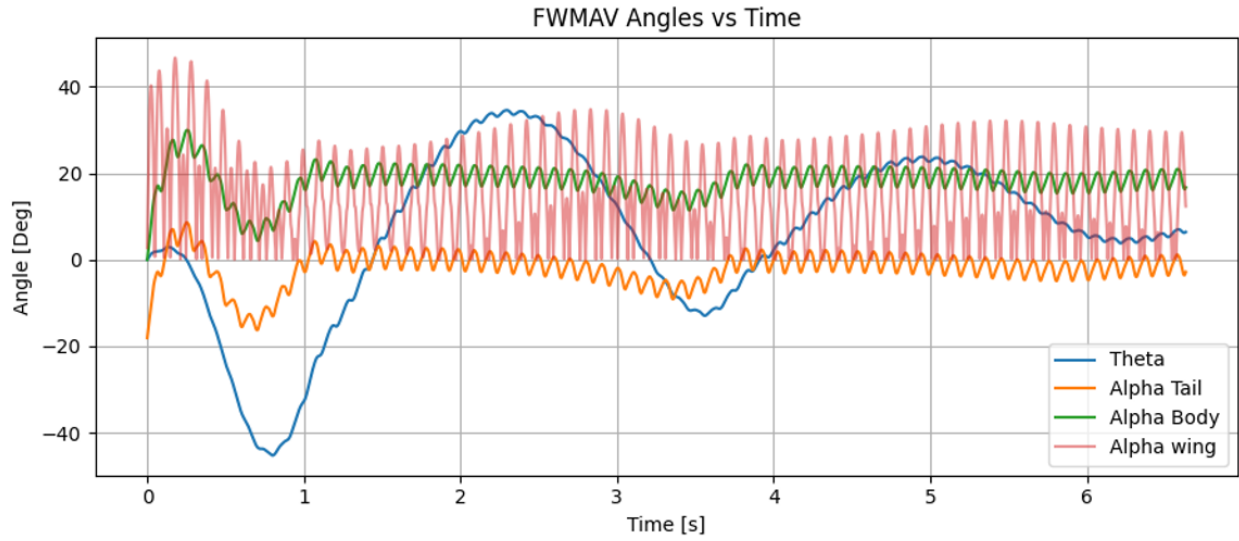
(a) Expanded view of the flight path of the FWMAV for a 6-second simulation of flapping seen in Figure 3.11a.



(b) Expanded view of the flapping and tail forces of the FWMAV for a 6-second simulation of flapping seen in Figure 3.11b.

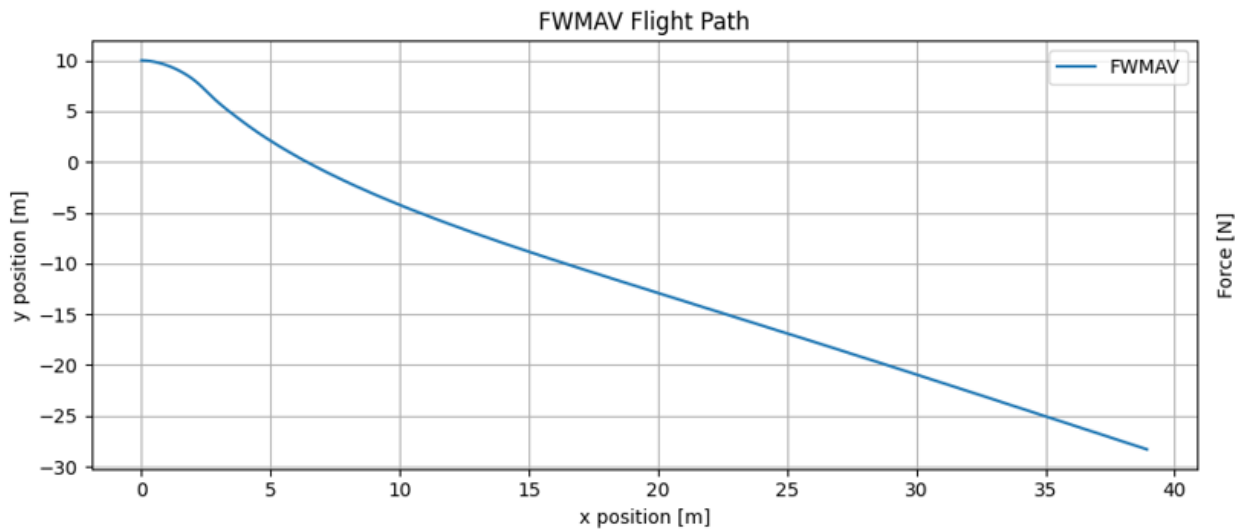


(a) Expanded view of the velocity of the FWMAV for a 6-second simulation of flapping seen in Figure 3.11c.

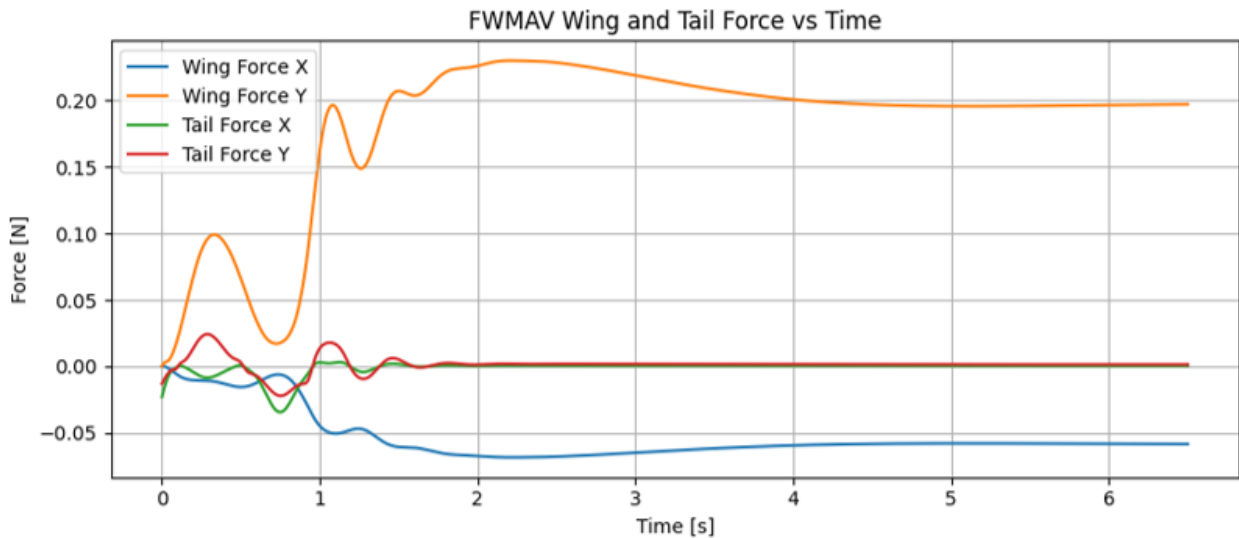


(b) Expanded view of the pitch and angle of attack of the FWMAV for a 6-second simulation of flapping seen in Figure 3.11d.

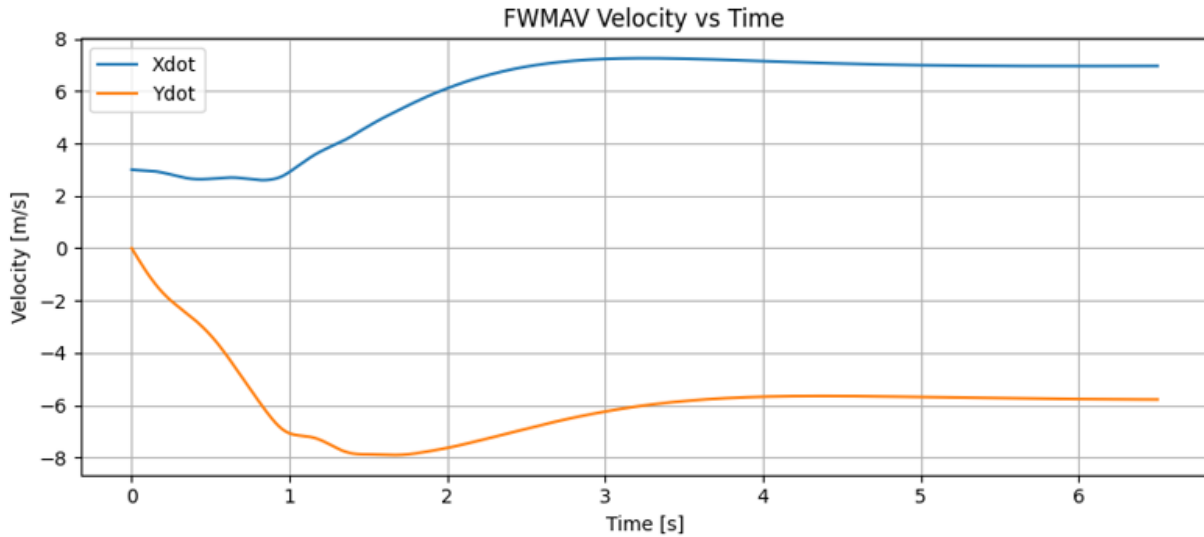
### A.2.2 Figures from Gliding Simulation



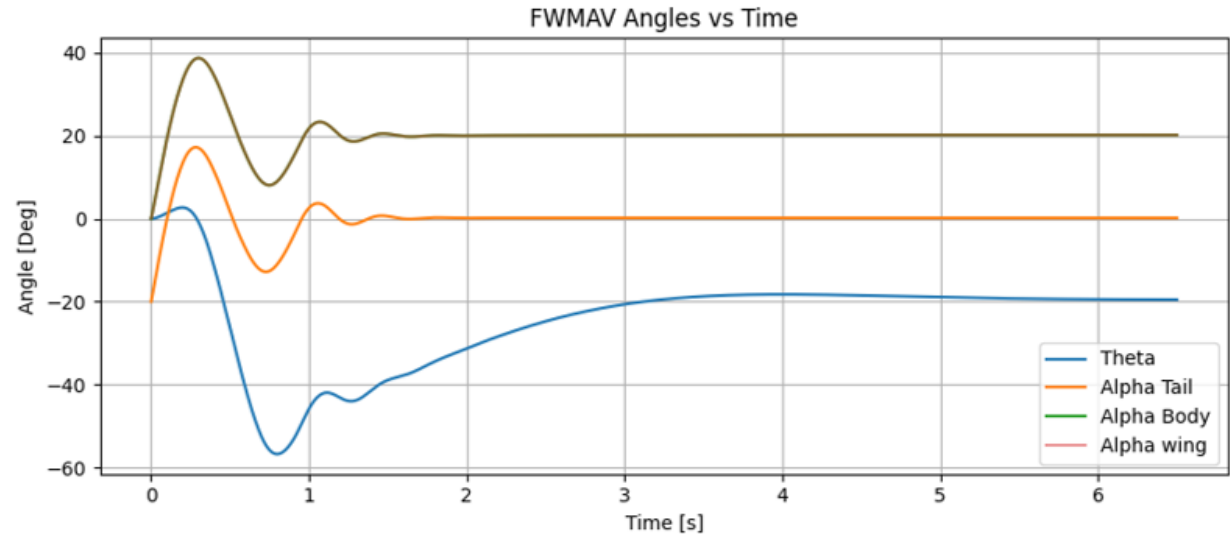
(a) Expanded view of the flight path of the FWMAV for a 6-second simulation of flapping seen in Figure 3.12a.



(b) Expanded view of the flapping and tail forces of the FWMAV for a 6-second simulation of flapping seen in Figure 3.12b.



(a) Expanded view of the velocity of the FWMAV for a 6-second simulation of flapping seen in Figure 3.12c.



(b) Expanded view of the pitch and angle of attack of the FWMAV for a 6-second simulation of flapping seen in Figure 3.12d.

# Bibliography

- [1] Saori Tanaka et al. “Review of Biomimetic Approaches for Drones”. In: *Drones* 6.11 (Oct. 26, 2022), p. 320. ISSN: 2504-446X. DOI: 10.3390/drones6110320. URL: <https://www.mdpi.com/2504-446X/6/11/320> (visited on 04/04/2024).
- [2] E. Farrell Helbling and Robert J. Wood. “A Review of Propulsion, Power, and Control Architectures for Insect-Scale Flapping-Wing Vehicles”. In: *Applied Mechanics Reviews* 70.1 (Jan. 1, 2018), p. 010801. ISSN: 0003-6900, 2379-0407. DOI: 10.1115/1.4038795. URL: <https://asmedigitalcollection.asme.org/appliedmechanicsreviews/article/doi/10.1115/1.4038795/443695/A-Review-of-Propulsion-Power-and-Control> (visited on 08/02/2023).
- [3] Bret W. Tobalske. “Biomechanics of bird flight”. In: *Journal of Experimental Biology* 210.18 (Sept. 15, 2007), pp. 3135–3146. ISSN: 1477-9145, 0022-0949. DOI: 10.1242/jeb.000273. URL: <https://journals.biologists.com/jeb/article/210/18/3135/17027/Biomechanics-of-bird-flight> (visited on 07/20/2023).
- [4] J.V. Caetano et al. “Linear Aerodynamic Model Identification of a Flapping Wing MAV Based on Flight Test Data”. In: *International Journal of Micro Air Vehicles* 5.4 (Dec. 2013), pp. 273–286. ISSN: 1756-8293, 1756-8307. DOI: 10.1260/1756-8293.5.4.273. URL: <http://journals.sagepub.com/doi/10.1260/1756-8293.5.4.273> (visited on 08/02/2023).
- [5] Zihao Chen et al. “Development of an Insect-like Flapping-Wing Micro Air Vehicle with Parallel Control Mechanism”. In: *Applied Sciences* 12.7 (Mar. 30, 2022), p. 3509. ISSN: 2076-3417. DOI: 10.3390/app12073509. URL: <https://www.mdpi.com/2076-3417/12/7/3509> (visited on 08/02/2023).

- [6] P. Paoletti and L. Mahadevan. “Intermittent locomotion as an optimal control strategy”. In: *Proceedings of the Royal Society A: Mathematical, Physical and Engineering Sciences* 470.2164 (Apr. 8, 2014), p. 20130535. ISSN: 1364-5021, 1471-2946. DOI: 10.1098/rspa.2013.0535. URL: <https://royalsocietypublishing.org/doi/10.1098/rspa.2013.0535> (visited on 07/20/2023).
- [7] Christopher T. Orlowski and Anouck R. Girard. “Dynamics, stability, and control analyses of flapping wing micro-air vehicles”. In: *Progress in Aerospace Sciences* 51 (May 2012), pp. 18–30. ISSN: 03760421. DOI: 10.1016/j.paerosci.2012.01.001. URL: <https://linkinghub.elsevier.com/retrieve/pii/S0376042112000103> (visited on 08/07/2023).
- [8] Ru Xu et al. “Intermittent control strategy can enhance stabilization robustness in bumblebee hovering”. In: *Bioinspiration & Biomimetics* 16.1 (Jan. 1, 2021), p. 016013. ISSN: 1748-3182, 1748-3190. DOI: 10.1088/1748-3190/abbc65. URL: <https://iopscience.iop.org/article/10.1088/1748-3190/abbc65> (visited on 08/07/2023).
- [9] Charles P. Ellington. “The Aerodynamics of Flapping Animal Flight”. In: *American Zoologist* 24.1 (Feb. 1984), pp. 95–105. ISSN: 0003-1569. DOI: 10.1093/icb/24.1.95. URL: <https://academic.oup.com/icb/article-lookup/doi/10.1093/icb/24.1.95> (visited on 04/04/2024).
- [10] Jr. Hubbard, Frecker James E., and Mary I. *Design, Fabrication and Testing of a Passively Morphing Ornithopter Wing for Increased Lift and Agility*: Fort Belvoir, VA: Defense Technical Information Center, Dec. 13, 2012. DOI: 10.21236/ADA581539. URL: <http://www.dtic.mil/docs/citations/ADA581539> (visited on 04/03/2024).
- [11] Addis Ababa Science and Technology University/College of Electrical and mechanical Engineering/Department of Electromechanical Engineering, Addis Ababa, Ethiopia and Lidiya Abebe Dejene. “Dynamic Modelling and Control of Flapping Wing Micro Air Vehicle for Flap-Glide Flight Mode”. In: *International Journal of Engineering*

*and Manufacturing* 12.5 (Oct. 8, 2022), pp. 22–47. ISSN: 23053631, 23065982. DOI: 10.5815/ijem.2022.05.03. URL: <http://www.mecs-press.org/ijem/ijem-v12-n5/v12n5-3.html> (visited on 07/20/2023).

- [12] Ortal Mizrahy-Rewald et al. “Empirical Evidence for Energy Efficiency Using Intermittent Gliding Flight in Northern Bald Ibises”. In: *Frontiers in Ecology and Evolution* 10 (June 13, 2022), p. 891079. ISSN: 2296-701X. DOI: 10.3389/fevo.2022.891079. URL: <https://www.frontiersin.org/articles/10.3389/fevo.2022.891079/full> (visited on 04/04/2024).
- [13] Fritz-Olaf Lehmann et al. “Elastic deformation and energy loss of flapping fly wings”. In: *Journal of Experimental Biology* 214.17 (Sept. 1, 2011), pp. 2949–2961. ISSN: 1477-9145, 0022-0949. DOI: 10.1242/jeb.045351. URL: <https://journals.biologists.com/jeb/article/214/17/2949/10511/Elastic-deformation-and-energy-loss-of-flapping> (visited on 08/02/2023).
- [14] Xinyan Deng et al. “Flapping flight for biomimetic robotic insects: part I-system modeling”. In: *IEEE Transactions on Robotics* 22.4 (Aug. 2006), pp. 776–788. ISSN: 1552-3098. DOI: 10.1109/TRO.2006.875480. URL: <http://ieeexplore.ieee.org/document/1668260/> (visited on 08/07/2023).
- [15] Joong-Kwan Kim and Jae-Hung Han. “A multibody approach for 6-DOF flight dynamics and stability analysis of the hawkmoth *Manduca sexta*”. In: *Bioinspiration & Biomimetics* 9.1 (Jan. 22, 2014), p. 016011. ISSN: 1748-3182, 1748-3190. DOI: 10.1088/1748-3182/9/1/016011. URL: <https://iopscience.iop.org/article/10.1088/1748-3182/9/1/016011> (visited on 04/04/2024).
- [16] David Lentink, Stefan R. Jongerius, and Nancy L. Bradshaw. “The Scalable Design of Flapping Micro-Air Vehicles Inspired by Insect Flight”. In: *Flying Insects and Robots*. Ed. by Dario Floreano et al. Berlin, Heidelberg: Springer Berlin Heidelberg, 2009, pp. 185–205. ISBN: 978-3-540-89392-9 978-3-540-89393-6. DOI: 10.1007/978-3-540-

89393-6\_14. URL: [http://link.springer.com/10.1007/978-3-540-89393-6\\_14](http://link.springer.com/10.1007/978-3-540-89393-6_14) (visited on 04/04/2024).

- [17] Wenqing Yang, Liguang Wang, and Bifeng Song. “Dove: A biomimetic flapping-wing micro air vehicle”. In: *International Journal of Micro Air Vehicles* 10.1 (Mar. 2018), pp. 70–84. ISSN: 1756-8293, 1756-8307. DOI: 10.1177/1756829317734837. URL: <http://journals.sagepub.com/doi/10.1177/1756829317734837> (visited on 04/03/2024).
- [18] Yilong Min et al. “Aspect Ratio Effects on the Aerodynamic Performance of a Biomimetic Hummingbird Wing in Flapping”. In: *Biomimetics* 8.2 (May 23, 2023), p. 216. ISSN: 2313-7673. DOI: 10.3390/biomimetics8020216. URL: <https://www.mdpi.com/2313-7673/8/2/216> (visited on 04/04/2024).
- [19] Haithem E. Taha, Muhammad R. Hajj, and Ali H. Nayfeh. “Flight dynamics and control of flapping-wing MAVs: a review”. In: *Nonlinear Dynamics* 70.2 (Oct. 2012), pp. 907–939. ISSN: 0924-090X, 1573-269X. DOI: 10.1007/s11071-012-0529-5. URL: <http://link.springer.com/10.1007/s11071-012-0529-5> (visited on 08/07/2023).
- [20] Shaoran Liang et al. “Active disturbance rejection attitude control for the dove flapping wing micro air vehicle in intermittent flapping and gliding flight”. In: *International Journal of Micro Air Vehicles* 12 (Jan. 2020), p. 175682932094308. ISSN: 1756-8293, 1756-8307. DOI: 10.1177/1756829320943085. URL: <http://journals.sagepub.com/doi/10.1177/1756829320943085> (visited on 07/20/2023).
- [21] Shu Tong, Zhang Weiping, and Mou Jiawang. “Research Progress on Control of Bioinspired Flapping-wing Micro Air Vehicles”. In: () .
- [22] Ru Xu, Xiangdong Zhang, and Hao Liu. “Effects of wing-to-body mass ratio on insect flapping flights”. In: *Physics of Fluids* 33.2 (Feb. 1, 2021), p. 021902. ISSN: 1070-6631, 1089-7666. DOI: 10.1063/5.0034806. URL: <https://pubs.aip.org/pof/article/33/2/021902/1032173/Effects-of-wing-to-body-mass-ratio-on-insect> (visited on 04/04/2024).

- [23] Jong-Seob Han, Jo Won Chang, and Jae-Hung Han. “An aerodynamic model for insect flapping wings in forward flight”. In: *Bioinspiration & Biomimetics* 12.3 (Mar. 31, 2017), p. 036004. ISSN: 1748-3190. DOI: 10.1088/1748-3190/aa640d. URL: <https://iopscience.iop.org/article/10.1088/1748-3190/aa640d> (visited on 09/25/2023).
- [24] Jorn A. Cheney et al. “Raptor wing morphing with flight speed”. In: *Journal of The Royal Society Interface* 18.180 (July 2021), p. 20210349. ISSN: 1742-5662. DOI: 10.1098/rsif.2021.0349. URL: <https://royalsocietypublishing.org/doi/10.1098/rsif.2021.0349> (visited on 04/04/2024).
- [25] Robert F. Stengel. *Flight dynamics*. Second edition. Princeton Oxford: Princeton University Press, 2022. 894 pp. ISBN: 978-0-691-22025-3.
- [26] Randal W. Beard and Timothy W. McLain. *Small unmanned aircraft: theory and practice*. OCLC: ocn724663112. Princeton, N.J: Princeton University Press, 2012. 300 pp. ISBN: 978-0-691-14921-9.
- [27] Thomas R. Yechout, Steven L. Morris, and American Institute of Aeronautics and Astronautics, eds. *Introduction to aircraft flight mechanics: performance, static stability, dynamic stability, and classical feedback control*. AIAA education series. Reston, Va: AIAA, American Institute of Aeronautics and Astronautics, 2003. 634 pp. ISBN: 978-1-56347-577-1.
- [28] Alexander P. Willmott and Charles P. Ellington. “The mechanics of flight in the hawkmoth *Manduca sexta* I. Kinematics of hovering and forward flight”. In: *Journal of Experimental Biology* 200.21 (Nov. 1, 1997), pp. 2705–2722. ISSN: 0022-0949, 1477-9145. DOI: 10.1242/jeb.200.21.2705. URL: <https://journals.biologists.com/jeb/article/200/21/2705/7599/The-mechanics-of-flight-in-the-hawkmoth-Manduca> (visited on 03/27/2024).
- [29] John Peter Whitney. “Design and Performance of Insect-Scale Flapping-Wing Vehicles”. In: () .

- [30] Sanjay P. Sane and Michael H. Dickinson. “The aerodynamic effects of wing rotation and a revised quasi-steady model of flapping flight”. In: *Journal of Experimental Biology* 205.8 (Apr. 15, 2002), pp. 1087–1096. ISSN: 0022-0949. DOI: 10.1242/jeb.205.8.1087. URL: <https://doi.org/10.1242/jeb.205.8.1087> (visited on 04/02/2024).
- [31] L. I. Sedov et al. “Two-Dimensional Problems in Hydrodynamics and Aerodynamics”. In: *Physics Today* 18.12 (Dec. 1, 1965), pp. 62–63. ISSN: 0031-9228, 1945-0699. DOI: 10.1063/1.3047038. URL: <https://pubs.aip.org/physicstoday/article/18/12/62/424294/Two-Dimensional-Problems-in-Hydrodynamics-and> (visited on 04/02/2024).
- [32] Jong-Seob Han et al. “An improved quasi-steady aerodynamic model for insect wings that considers movement of the center of pressure”. In: *Bioinspiration & Biomimetics* 10.4 (July 30, 2015), p. 046014. ISSN: 1748-3190. DOI: 10.1088/1748-3190/10/4/046014. URL: <https://iopscience.iop.org/article/10.1088/1748-3190/10/4/046014> (visited on 09/27/2023).
- [33] J. D. DeLaurier. “An aerodynamic model for flapping-wing flight”. In: *The Aeronautical Journal* 97.964 (Apr. 1993), pp. 125–130. ISSN: 0001-9240, 2059-6464. DOI: 10.1017/S0001924000026002. URL: [https://www.cambridge.org/core/product/identifier/S0001924000026002/type/journal\\_article](https://www.cambridge.org/core/product/identifier/S0001924000026002/type/journal_article) (visited on 08/07/2023).
- [34] Muhammad Yousaf Bhatti, Sang-Gil Lee, and Jae-Hung Han. “Dynamic Stability and Flight Control of Biomimetic Flapping-Wing Micro Air Vehicle”. In: *Aerospace* 8.12 (Nov. 24, 2021), p. 362. ISSN: 2226-4310. DOI: 10.3390/aerospace8120362. URL: <https://www.mdpi.com/2226-4310/8/12/362> (visited on 12/22/2023).
- [35] Yufeng Chen, Kevin Ma, and Robert J. Wood. “Influence of wing morphological and inertial parameters on flapping flight performance”. In: *2016 IEEE/RSJ International Conference on Intelligent Robots and Systems (IROS)*. 2016 IEEE/RSJ International Conference on Intelligent Robots and Systems (IROS). Daejeon, South Korea:

IEEE, Oct. 2016, pp. 2329–2336. ISBN: 978-1-5090-3762-9. DOI: 10.1109/IROS.2016.7759363. URL: <http://ieeexplore.ieee.org/document/7759363/> (visited on 04/05/2024).